



536759  
146P

TR/IN/24  
2001 112 692

# The Oxidation Kinetics of Continuous Carbon Fibers in a Cracked Ceramic Matrix Composite

Michael C. Halbig  
U.S. Army Research Laboratory, Glenn Research Center, Cleveland, Ohio

## The NASA STI Program Office . . . in Profile

Since its founding, NASA has been dedicated to the advancement of aeronautics and space science. The NASA Scientific and Technical Information (STI) Program Office plays a key part in helping NASA maintain this important role.

The NASA STI Program Office is operated by Langley Research Center, the Lead Center for NASA's scientific and technical information. The NASA STI Program Office provides access to the NASA STI Database, the largest collection of aeronautical and space science STI in the world. The Program Office is also NASA's institutional mechanism for disseminating the results of its research and development activities. These results are published by NASA in the NASA STI Report Series, which includes the following report types:

- **TECHNICAL PUBLICATION.** Reports of completed research or a major significant phase of research that present the results of NASA programs and include extensive data or theoretical analysis. Includes compilations of significant scientific and technical data and information deemed to be of continuing reference value. NASA's counterpart of peer-reviewed formal professional papers but has less stringent limitations on manuscript length and extent of graphic presentations.
- **TECHNICAL MEMORANDUM.** Scientific and technical findings that are preliminary or of specialized interest, e.g., quick release reports, working papers, and bibliographies that contain minimal annotation. Does not contain extensive analysis.
- **CONTRACTOR REPORT.** Scientific and technical findings by NASA-sponsored contractors and grantees.

- **CONFERENCE PUBLICATION.** Collected papers from scientific and technical conferences, symposia, seminars, or other meetings sponsored or cosponsored by NASA.
- **SPECIAL PUBLICATION.** Scientific, technical, or historical information from NASA programs, projects, and missions, often concerned with subjects having substantial public interest.
- **TECHNICAL TRANSLATION.** English-language translations of foreign scientific and technical material pertinent to NASA's mission.

Specialized services that complement the STI Program Office's diverse offerings include creating custom thesauri, building customized data bases, organizing and publishing research results . . . even providing videos.

For more information about the NASA STI Program Office, see the following:

- Access the NASA STI Program Home Page at <http://www.sti.nasa.gov>
- E-mail your question via the Internet to [help@sti.nasa.gov](mailto:help@sti.nasa.gov)
- Fax your question to the NASA Access Help Desk at 30-621-0134
- Telephone the NASA Access Help Desk at 301-621-0390
- Write to:  
NASA Access Help Desk  
NASA Center for AeroSpace Information  
7121 Standard Drive  
Hanover, MD 21076



# The Oxidation Kinetics of Continuous Carbon Fibers in a Cracked Ceramic Matrix Composite

Michael C. Halbig

U.S. Army Research Laboratory, Glenn Research Center, Cleveland, Ohio

National Aeronautics and  
Space Administration

Glenn Research Center

## Acknowledgment

The author would like to acknowledge James D. Cawley and Andrew J. Eckel for their guidance.

Available from

NASA Center for Aerospace Information  
7121 Standard Drive  
Hanover, MD 21076

National Technical Information Service  
5285 Port Royal Road  
Springfield, VA 22100

Available electronically at <http://gltrs.grc.nasa.gov/GLTRS>

<b>TABLE OF CONTENTS</b>	<u>Page</u>
1. Introduction	1
1.1 Objectives	3
1.2 Materials Description	4
1.3 Theory	5
2. Experimental Studies of C/SiC	18
2.1 Materials and Experimental	18
2.1.1 TGA of T-300 Carbon Fiber	19
2.1.2 TGA of C/SiC Coupons	19
2.1.3 Stressed Oxidation of C/SiC Coupons	20
2.1.4 Creep of C/SiC Coupons	21
2.1.5 Stressed Oxidation of Four Different C/SiC Materials	21
2.2 Results	24
2.2.1 TGA of T-300 Carbon Fiber	24
2.2.2 TGA of C/SiC Coupons	25
2.2.3 Stressed Oxidation of C/SiC Coupons	27
2.2.4 Creep of C/SiC Coupons	34
2.2.5 Stressed Oxidation of Four Different C/SiC Materials	35
2.3 Discussion	38
2.3.1 TGA of T-300 Carbon Fiber	38
2.3.2 TGA of C/SiC Coupons	43
2.3.3 Stressed Oxidation of C/SiC Coupons	44
2.3.4 Creep of C/SiC Coupons	45
2.3.5 Oxidation Patterns and Trends	47
2.3.6 Stressed Oxidation of Four Different C/SiC Materials	55
2.4 Experimental Summary	71
3. Modeling	73
3.1 Model Development	73
3.1.1 Oxygen Concentration at Steady-State	73
3.1.2 Carbon Consumption	81
3.1.3 Model Geometry Study and Comparison to Analytical Solutions	86
3.2 Results	95
3.2.1 Oxygen Concentration at Steady-State	95
3.2.2 Carbon Consumption	98
3.2.3 Model Geometry Study and Comparison to Analytical Solutions	105
3.3 Discussion	111
3.3.1 Oxygen Concentration at Steady-State	111
3.3.2 Carbon Consumption	112
3.3.3 Model Geometry Study and Comparison to Analytical Solutions	117
3.4 Modeling Summary	120
4. Conclusions	122
5. Appendix - Studying the Effect of Flaws	125
6. Bibliography	133

## LIST OF TABLES

	<u>Page</u>
Table I. Calculated values for the diffusion coefficient and the reaction rate constant and the resulting Sherwood number.	14
Table II. Objectives of experimental tests conducted on carbon fiber and C/SiC composite material.	18
Table III. Constituents and processing properties of four different C/SiC materials.	23
Table IV. Times to failure and strains to failure for the stressed oxidation of C/SiC coupons in air at a stress of 69 MPa (10 ksi).	29
Table V. Times to failure and strains to failure for the stressed oxidation of C/SiC coupons in air at a stress of 172 MPa (25 ksi).	30

<b>LIST OF FIGURES</b>	<u>Page</u>
Figure 1. Oxidation of crack bridging fibers at an elevated temperature in air.	6
Figure 2. Polished cross-section of C/SiC material showing cracks traversing through the material.	7
Figure 3. Generalized representation of continuous carbon fiber tows bridging a matrix crack.	8
Figure 4. Temperature effect on the diffusion coefficient.	15
Figure 5. Temperature effect on the reaction rate constant.	16
Figure 6. Illustrations of the oxidation of an array of fiber tows for reaction controlled and diffusion controlled kinetics.	17
Figure 7. Percent weight loss versus time for the thermogravimetric analysis of T300 carbon fiber in an oxygen environment.	25
Figure 8. Percent weight loss versus time for the thermogravimetric analysis of C/SiC coupons in an oxygen environment.	26
Figure 9. Strain versus time for the stressed oxidation of C/SiC test coupons at temperatures of 350°C and 550°C and stresses of 69 MPa and 172 MPa.	31
Figure 10. Strain versus time for the stressed oxidation of C/SiC test coupons at temperatures of 750°C to 1500°C and a stress of 69 MPa.	32
Figure 11. Strain versus time for the stressed oxidation of C/SiC test coupons at temperatures of 750°C to 1500°C and a stress of 172 MPa.	33
Figure 12. Creep tests of C/SiC coupons at 750°C in air and inert environments.	34
Figure 13. Times to failure for 4 different C/SiC materials at a temperature of 1454°C and a stress of 69 MPa.	36
Figure 14. Times to failure for 4 different C/SiC materials at a temperature of 1454°C and a stress of 172 MPa.	37
Figure 15. Determination of the activation energy of T300 carbon fiber.	42
Figure 16. Polished cross-section showing oxidation of carbon fibers occurring preferentially along microcracks.	49

Figure 17. Fracture surface showing oxidation of the pyro-carbon interphase and narrowing of the fiber cross-section.	50
Figure 18. Fracture surface showing fibers receding to the left and right away from a matrix crack.	51
Figures 19a-c. Cross-sections of a sample tested at 750°C/69 MPa.	53
Figures 20a-c. Cross-sections of a sample tested at 1400°C/69 MPa.	54
Figure 21a-c. Material A: DuPont-Lanxide standard C/SiC.	56
Figure 22a-c. Material B: BFG C/SiC.	57
Figure 23. Fracture surface of a sample that was stressed oxidation tested at 1454°C/69 MPa.	58
Figure 24. Fracture surface of a sample that was stressed oxidation tested at 1454°C/69 MPa.	59
Figures 25a-b. Polished cross-section of the interior of material C which shows boron containing particulates.	61
Figures 26a-b. Polished cross-section of the interior of material D which shows boron containing particulates.	62
Figure 27a-d. Material C: DuPont-Lanxide enhanced C/SiC.	63
Figure 28. SEM micrograph of the fracture surface of a DLC enhanced C/SiC sample that was stressed oxidation tested at 1454°C/172 MPa.	64
Figure 29. SEM micrograph of the fracture surface of a DLC enhanced C/SiC sample that was stressed oxidation tested at 1454°C/172 MPa.	65
Figure 30a-b. Test coupon failure locations.	66
Figure 31a-c. Material D: DuPont-Lanxide enhanced C/SiC with CBS.	68
Figure 32a-b. Incomplete chemical vapor infiltration of silicon carbide into fiber tows.	69
Figure 33a-b. Oxidation in a cross-section taken from the thermal gradient region.	70

Figure 34. Illustration of a 12x12 array of crack bridging fiber tows.	75
Figure 35a-b. One-quarter plot of the matrix pattern orientated as shown in the sectioned square.	76
Figure 36. Detail of cell pattern near fiber tow.	80
Figure 37. Circular core of carbon represented by square cells.	86
Figure 38a-e. Cases considered in the models.	89
Figure 39. Geometry of cracked carbon material where oxygen diffuses down an open column bounded by carbon.	91
Figure 40. Oxygen concentration at steady-state for $Sh=0.1$ and $Sh= 0.0001$ .	96
Figure 41. Oxygen concentrations across the center of the surface for several Sherwood values.	97
Figure 42. Shrinking core without geometry correction.	99
Figure 43. Shrinking core with geometry correction.	100
Figure 44. Radius reduction for reacting core with and without geometry correction.	101
Figure 45. Model results for cross-section at a temperature of 1400°C.	103
Figure 46. Model results for cross-section at a temperature of 700°C.	104
Figure 47. Oxygen concentration along the midline for the analysis of the case of diffusion down a column bounded by continuous walls of carbon.	106
Figure 48. Oxygen concentrations one-eighth of the distance down the column length for the CW model and the 2-D analytical solution for the five line positions of width parallel to the midline.	107
Figure 49. Oxygen concentrations across the midline for different geometries.	109
Figure 50. Oxygen concentration across the long dimension of the 12 x 36 FTA model.	110

Figure 51a-b. Close-up of carbon core originally of 59 cells in radius at 95% carbon reacted without a geometry correction and with a geometry correction.	115
Figure 52. Modeling a realistic C/SiC geometry.	116
Figure 53. Correcting the continuous wall models to fit the bumped wall model.	119

## 1. INTRODUCTION

Carbon fiber reinforced silicon carbide matrix composites (C/SiC) are a ceramic matrix composite material that is proposed for several high temperature structural applications. Applications include nozzle ramps, nozzles, thrusters, turbopumps, and turbines (Effinger *et al.*, 1997; Herbell and Eckel, 1993A; Herbell and Eckel, 1993B). This material offers benefits over superalloys such as higher temperature capability, thermal shock resistance, higher strength to density ratio and thus lighter weight. The use of continuous fiber reinforcement in ceramics offers to reduce the brittle failures that are inherent in monolithic ceramics. The proposed applications for C/SiC are primarily in space applications where high strength, light weight, and high temperature capability are major requirements. Lighter weight can lead to benefits of increased thrust (performance) and/or increased payload. Higher temperature capability is important since the flame temperature of the fuels used is very high (greater than 3000°C) and since the use of conventional superalloys requires the use of complex cooling schemes. The use of high temperature materials that requires little or no cooling can allow for simpler and more flexible designs which would lead to smaller overall vehicle designs and weight savings. Despite the benefits of using C/SiC in these types of applications, one of the barriers to its use in high-temperature applications is the degradation of the carbon fiber reinforcement particularly in oxidizing environments, which can lead to strength reduction and component failure.

The oxidation of carbon in its bulk (Pickup *et al.*, 1986; Wood *et al.*, 1980) and fabric forms (Ismail, 1991) has been well investigated. However, the oxidation kinetics of carbon fibers in complex composite systems are less known. Many studies involve

thermogravimetric analysis (TGA) in which weight loss of the composite is monitored over time (Goujard *et al.*, 1994; Lamouroux *et al.*, 1994; Lamouroux *et al.*, 1993; Filipuzzi *et al.*, 1994). These types of studies provide valuable information, however the oxidation of the composites in unstressed and stressed states can be very different. In an unstressed state, the formation of silica near 1200°C and the closing of pre-existing cracks near the processing temperature seals the cracks and protects the interior of the composite from the outside environment (Lamouroux *et al.*, 1994; Filipuzzi *et al.*, 1994; Vix-Guterl *et al.*, 1993). However in many real application conditions, stresses present can prevent cracks from sealing due to wide crack openings and the relatively slow rate of silica growth.

While TGA tests were conducted, the oxidation kinetics of carbon fibers in a silicon carbide matrix were also studied in stressed conditions. Although, weight could not be monitored as in TGA experiments, the times and strains to failure of the composites provide a gage of the amount of oxidation. Optical and scanning electron microscopy of polished cross-sections and fracture surfaces also give indications of the amount of oxidation. The experimental results were used to provide a basis for developing a model to gain a better understanding of diffusion and reaction-controlled kinetics.

A finite difference model was developed which simulates the diffusion of oxygen into a matrix crack bridged by an array of carbon fiber tows where a tow is a bundle of individual continuous carbon fibers, often in bundles of 1000. The model provides a visual, qualitative, and quantitative basis for understanding the oxidation kinetics. The

influence of important variables, T (temperature), D (diffusion coefficient), K (reaction rate constant), geometry, and environment, were all studied using the model.

### 1.1 Objectives

There were several objectives to the work in this thesis. The first two were to investigate through experimentation the susceptibility of carbon fiber to oxidation and to study the oxidation kinetics. The activation energy of carbon fiber was determined. The two primary regimes of oxidation kinetics, diffusion-controlled and reaction-controlled, were identified. Oxidation patterns and trends relating to each regime were also investigated. Other factors that influence oxidation of the carbon fibers in a matrix were analyzed and included matrix oxidation, crack closure, stress, environment, and oxidation inhibitors. Objectives relating to the development and use of the model included identifying the kinetic regimes, simulating experimental results, studying the effect of sample geometry, and comparing the model to analytical solutions. Analysis of the model by using different Sherwood numbers gave oxygen concentrations that related to the two regimes and showed the effect of specific variables in relation to one another such as temperature, diffusion coefficient, characteristic length, oxygen partial pressure and, reaction rate constant which for the system under consideration is the effective mass transfer coefficient. The Sherwood number, which will be described in greater detail later in this thesis, is a dimensionless parameter that describes the gradient in oxygen concentration at the surface. Oxidation patterns for reacted cross-sections that correlated with experimental results were obtained using the model. Comparing the model results to analytical solutions helped validate the model and determine cases when it is preferred to conduct analysis with the simpler to use analytical solutions.

## 1.2 Material Description

Processing and properties of the constituents in C/SiC composites will now be discussed with the focus being on one common form of the composite. The C/SiC composite materials to be discussed in this work were made by DuPont-Lanxide Composites Inc. (now known as Honeywell Advanced Composites, Inc.) and B.F. Goodrich. The composites consisted of PAN-based T300 carbon fibers that are in tows of 1000 fibers (bundles). The fibers are made from polymer precursors in the form of textile fibers that leave a residue of carbon and do not melt during pyrolysis in an inert atmosphere. The fibers have a diameter of 8 microns and are grouped into bundles of 1000 continuous fibers called 1k fiber tows. The carbon preform consists of 0° and 90° fiber tows woven into what is called a plain weave configuration. Fibers in the 0° direction are woven with fibers in the 90° direction to form a two layer weave called a ply. The plies are stacked until the desired thickness is achieved. A pyrolytic-carbon interphase, typically 0.5-1.0 microns in thickness, is then deposited onto the carbon preform using chemical vapor deposition. The SiC matrix is deposited through chemical vapor infiltration. The composite panels are commonly 20.3 cm x 25.4 and 0.32 cm thick (8" x 10" and 1/8" thick). Test coupons are cut from the panel and a SiC external seal-coating is applied using chemical vapor deposition.

C/SiC materials have a pre-cracked as-received condition due to the SiC matrix cracking when cooled down from the processing temperature. The microcracks arise due the coefficient of thermal expansion mismatch between the carbon fiber and the silicon carbide matrix and the large change in temperature when cooling down from the processing temperature. Lamouroux summarized the coefficients of thermal expansions

(CTE) from other researchers and discussed their relation with one another (Lamouroux *et al.*, 1993). The T300 carbon fiber is an anisotropic material; the coefficient of thermal expansion in the longitudinal direction is negative and has low values in the range of  $-0.1 \times 10^{-6}$  to  $-1.1 \times 10^{-6} / ^\circ\text{C}$  (Mensessier *et al.*, 1989; Yasada *et al.*, 1993). The coefficient of thermal expansion for T300 in the radial direction, determined using a TEM technique, was reported to be  $7 \times 10^{-6} / ^\circ\text{C}$  (Villeneuve *et al.*, 1993). The coefficient of thermal expansion for CVI SiC which is assumed to be isotropic is reported to be  $4.8 \times 10^{-6} / ^\circ\text{C}$  (Lowden, 1989). Due to the matrix having a larger CTE than the fiber in its longitudinal direction, the matrix is put under a tensile stress by the woven fibers during cooling and develops microcracks in directions perpendicular to the fiber axis. Also, since the coefficient of thermal expansion of the carbon fiber in the radial direction is larger than the coefficient of thermal expansion for the matrix, decohesion between the fiber and matrix occurs during cooling.

### 1.3 Theory

The related theory in the oxidation of a carbon fiber in a non-reactive matrix was used in the development of a finite difference, cracked matrix model used to study oxidation kinetics. In a ceramic matrix composite that has as-fabricated microcracks, continuous fibers will bridge the crack. These cracks allow for the ingress of oxygen. Portions of the fibers that bridge a crack will be susceptible to oxidation as shown in Figure 1. Cracks can be readily traced from one edge of the matrix across to the other edge as the cracks traverse through the fibers tows and matrix of the interior of the material. An example of a polished cross-section of traversing cracks is shown in Figure 2. Based on these types of microstructural analyses, an idealization of the relevant

geometry is assumed as illustrated in Figure 3. Oxygen is able to diffuse into the microcracks and react with carbon to form an oxide (either carbon monoxide or carbon dioxide). The oxide then diffuses out of the microcrack to the atmosphere.

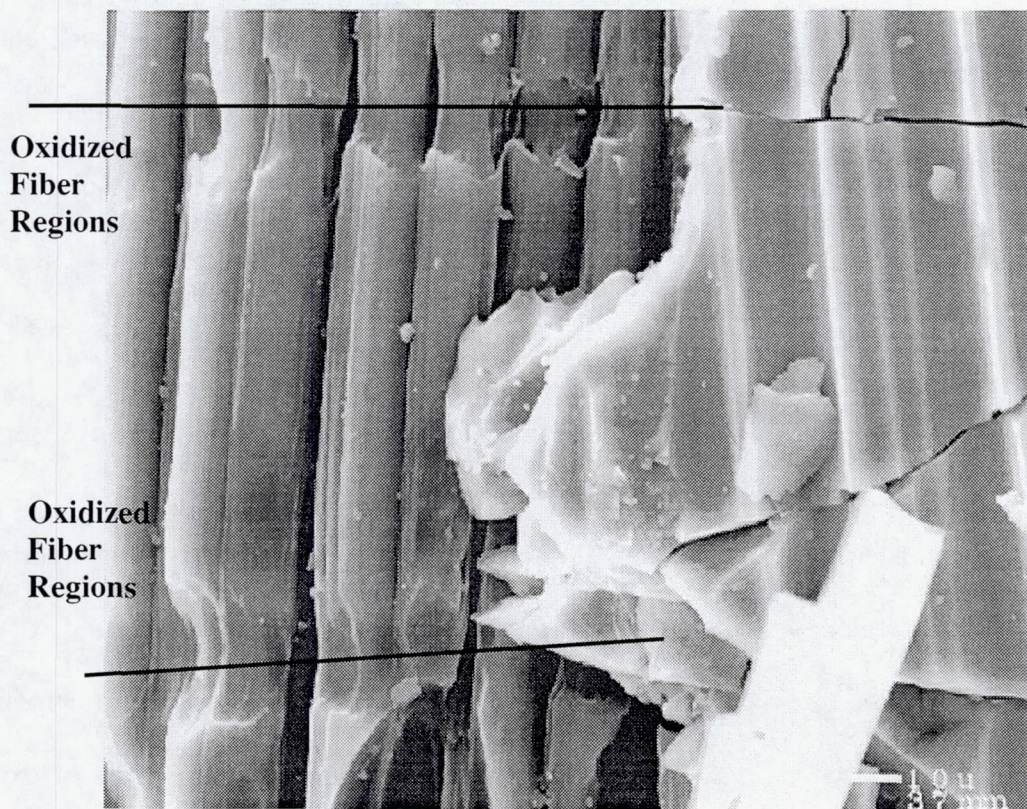


Figure 1. Oxidation of crack bridging fibers at an elevated temperature in air.

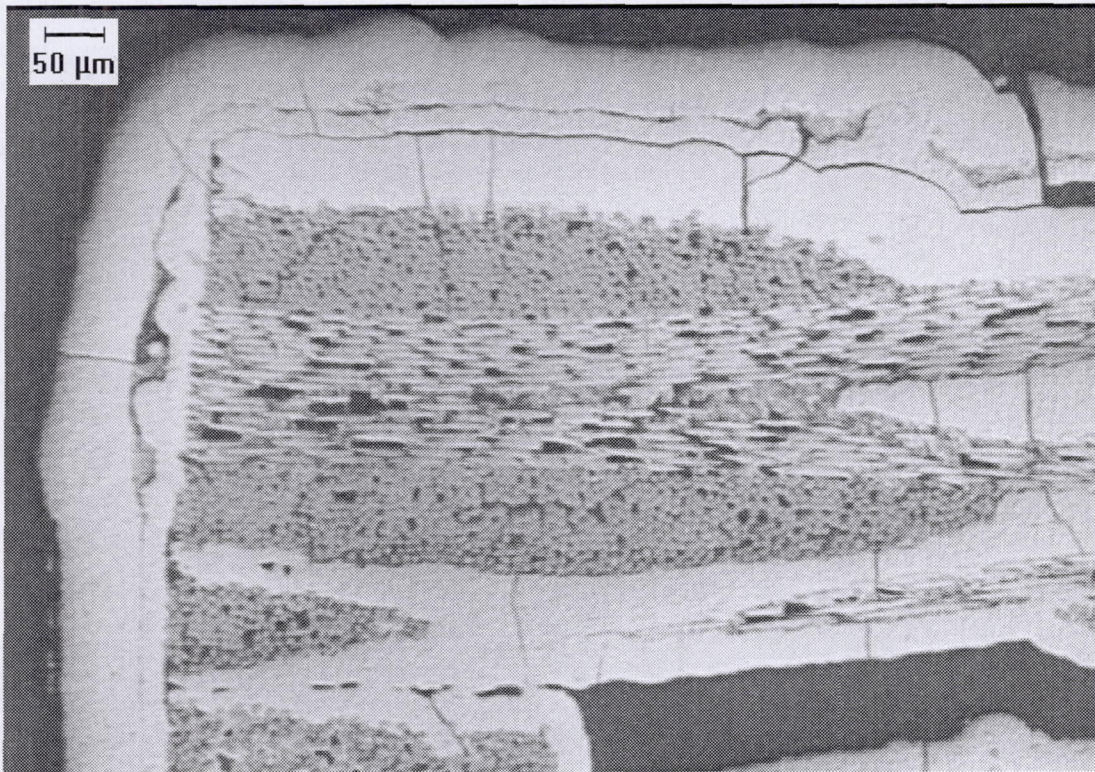


Figure 2. Polished cross-section of C/SiC material showing cracks traversing through the material.

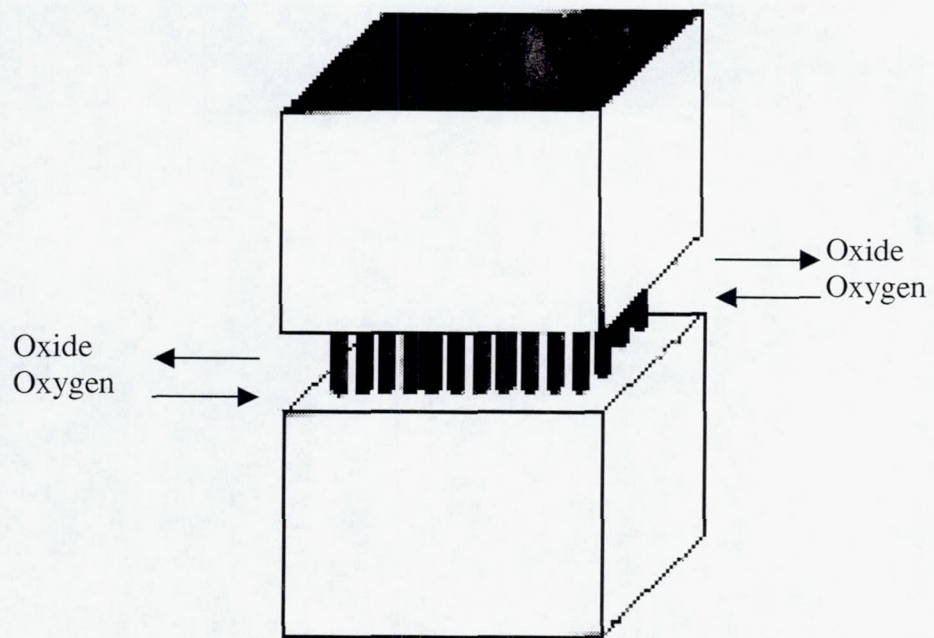


Figure 3. Generalized representation of continuous carbon fiber tows bridging a matrix crack.

The oxidation kinetics for the recession of carbon can be described by the linear-parabolic rate law [Eckel *et al.*, 1995]:

$$\frac{x^2}{k_p} + \frac{x}{k_l} = t, \quad (1)$$

where  $x$  (m) is the recession distance of the carbon,  $k_p$  is the parabolic rate constant ( $\text{m}^2/\text{sec}$ ),  $k_l$  is the linear rate constant ( $\text{m}/\text{sec}$ ) and  $t$  is time (sec). Equation (1) is used for the case of planar recession such as for the case of a single fiber that is end-on in a crack free matrix.

The parabolic and linear rate constants can be related to more familiar constants, specifically the diffusion coefficient and the reaction rate constant. Only the relevant equations will be discussed. More thorough discussions and derivations can be found in papers by Eckel *et al.* (Eckel *et al.*, 1995) and Glime and Cawley (Glime and Cawley, 1995).

When the linear term in equation (1) drops out (or for small  $x$ ) and carbon dioxide is the evolving oxide, the equation for the recession distance is expressed as (Eckel *et al.*, 1995)

$$x = t^{1/2} k_p^{1/2} = t^{1/2} \left( \frac{2D_{AB} C_{ox}}{\rho_c} \right) \quad (2)$$

such that

$$k_p = \left( \frac{2D_{AB} C_{ox}}{\rho_c} \right) \quad (3)$$

where  $D_{AB}$  ( $\text{m}^2 / \text{sec}$ ) is the diffusion coefficient of gas A (oxygen) diffusing in the stationary or stagnant atmosphere of gas B (oxide),  $C_{ox}$  is the oxygen concentration of the atmosphere ( $\text{mol} / \text{m}^3$ ) and  $\rho_c$  is the molar density of carbon ( $\text{mol} / \text{m}^3$ ). In some

experimental situations, carbon monoxide is the reaction product, but the form of Equation (2) will be the same and there will be a modest 30% difference in its magnitude (Eckel *et al.*, 1995).

The discussion does not consider Knudsen effects in which molecular-wall collisions are more frequent than inter-molecular collisions. Knudsen effects are not a factor until the pore becomes as small as 0.1  $\mu\text{m}$  (Eckel *et al.*, 1995). In the C/SiC material studied, typical cracks in the matrix and seal coating are on the order of 1  $\mu\text{m}$ . Also, the model considers a stressed state where the cracks are open even further.

The second limiting case occurs when  $k_p$  is much larger than  $k_1$ , i.e. when the parabolic term drops out and the linear term limits. In this case, the recession distance can be expressed as

$$x = t k_1 = t \frac{K C_{\text{ox}}}{\rho_c} \quad (4)$$

such that

$$k_1 = \frac{K C_{\text{ox}}}{\rho_c} \quad (5)$$

where  $K$  is the reaction rate constant (m/s).

The above equation takes an alternate form when the oxygen concentration is substituted by the oxygen partial pressure,  $\chi$ , times the total concentration of gas molecules in the atmosphere,  $C_T$  ( $\text{mol/m}^3$ ). The total concentration can be substituted using the ideal gas law so that Equation (5) becomes

$$k_1 = \left( \frac{1}{\rho_c} \right) (\chi C_T) K = \left( \frac{1}{\rho_c} \right) \left( \frac{\chi P}{R T} \right) K \quad (6)$$

where P is pressure (Pa), R is the gas constant (J/mol K), and T is the absolute temperature (K).

Substituting values for  $k_p$  and  $k_1$ , Equation (1) becomes

$$t = \frac{x^2}{k_p} + \frac{x}{k_1} = \frac{x^2}{\left(2D_{AB} \frac{C_{ox}}{\rho_c}\right)} + \frac{x}{\left(\frac{1}{\rho_c}\right)\left(\chi \frac{P}{RT}\right)K} \quad (7)$$

The diffusion coefficient,  $D_{AB}$ , can be obtained from Chapman-Enskog kinetic theory (Geankoplis, 1978)

$$D_{AB} = \left(5.9543 \times 10^{-24}\right) \frac{T^{3/2} \left(\frac{1}{M_A} + \frac{1}{M_B}\right)^{1/2}}{P \sigma_{AB}^2 \Omega_{AB}} \quad (8)$$

and the reaction rate constant, K (m/s), can be expressed in an Arrhenius form:

$$K = k_0 \exp\left(\frac{-Q}{RT}\right) \quad (9)$$

where  $D_{AB}$  ( $m^2 / sec$ ) again is the diffusion coefficient of gas A (oxygen) diffusing in the stationary or stagnant atmosphere of gas B (oxide), T is temperature (K),  $M_A$  and  $M_B$  are the molecular weights of gases A and B (kg/mol), and P is pressure (Pa). The symbols  $\sigma_{AB}$  (m) and  $\Omega_{AB}$  (dimensionless) are Leonard Jones potentials for the collision diameter and collision integral respectively. Values for the collision diameter and the characteristic energy of interaction between the molecules which is needed for calculating the collision integral can be found in tables (Bird *et al.*, 1963, Geankoplis, 1978). Q is the activation energy (J/mol). The term  $k_0$  is a pre-exponential constant (m/s).

From the above equations for the diffusion coefficient (8) and the reaction rate constant (9), it is seen that one of the two arguments in Equation (7) will dominate

depending on temperature and if  $x$  is small or large. The diffusion coefficient depends on  $T^{3/2}$ , with the effect being even less when the decreasing molar density of the gas is considered with increasing temperature. The reaction rate constant varies exponentially with inverse temperature when large activation energies are considered.

It can be seen that Equation (7) describes a two step process occurring in series. Each step has the potential to limit the overall process. Although Equation (7) is used to describe planar recession, qualitative trends can be predicted for an alternate geometry such as for crack bridging fiber tows. For the case of bridging fiber tows, which will be further discussed in the experimental portion of this thesis, recession is first in the radial direction of the fiber tow and then along fiber tow axis. Equation (7) is used to illustrate the two step process from which the dominating kinetics develop. For the case of crack bridging fiber tows, prediction and analysis of oxygen concentrations was used to study kinetics and the Sherwood number was used to further convey the concept of the two step process. From using Chapman-Enskog Kinetic theory (assuming  $O_2$  and  $CO$  as the reactant and product gasses respectively) and from using data from Eckel *et al.* (Eckel *et al.*, 1995) for the linear recession rate at  $800^\circ C$  (to determine the reaction rate constant at this temperature assuming an activation energy of  $100 \text{ kJ/mol}$ ), the diffusion coefficients and reaction rate constants across the temperature range of  $600\text{-}1500^\circ C$  ( $873\text{-}1773\text{K}$ ) were determined. The calculated values versus temperature are shown in Table I and plotted in Figure 4 and 5 and show that across this temperature range the diffusion coefficient will change by a factor of 3. In marked contrast, the reaction rate constant, which has a much greater temperature dependence, will change by 3 orders of magnitude. Examples of the two limiting cases are illustrated in Figure 6 and correspond to the cross-

sections of an open region where fibers bridge a crack such as the case illustrated in Figure 3. When the reaction rate constant is small and the diffusion coefficient is large, the process will be limited by the reaction rate, i.e. reaction-controlled (for low temperature and/or small  $x$ ). Oxygen will diffuse into the cracks and therefore into the material faster than it can react so that the pore becomes saturated in oxygen. As illustrated in the two stages of oxidation over time, there will be a general oxidation throughout the array of bridging fibers. However, if the diffusion coefficient is small compared to the reaction rate constant, carbon/oxygen reactions occur as soon as oxygen is supplied. In this case the process is controlled by the slower diffusion step, i.e. diffusion-controlled (for high temperature and /or large  $x$ ). As illustrated in the two stages of oxidation over time for the case of diffusion-controlled kinetics, there will be a moving reaction front of oxygen traveling inward as the carbon continues to be consumed. A shrinking core effect will be obtained. These two types of kinetics will be included in the modeling part of this thesis.

T (K)	D (cm <sup>2</sup> /sec)	K (cm/s)	Sh
773	1.08	0.179	8.29E-04
873	1.25	1.17	4.68E-03
973	1.54	4.84	1.57E-02
1073	1.79	15.3	4.25E-02
1173	2.06	39.8	9.66E-02
1273	2.32	89.1	0.192
1373	2.68	177	0.330
1473	3.01	321	0.533
1573	3.36	540	0.804
1673	3.73	853	1.14
1773	4.12	1270	1.55

Table I. Calculated values for the diffusion coefficient and the reaction rate constant and the resulting Sherwood number. The geometry based  $\Delta x$  value used to determine the Sherwood number was  $5.0 \times 10^{-5}$  cm.

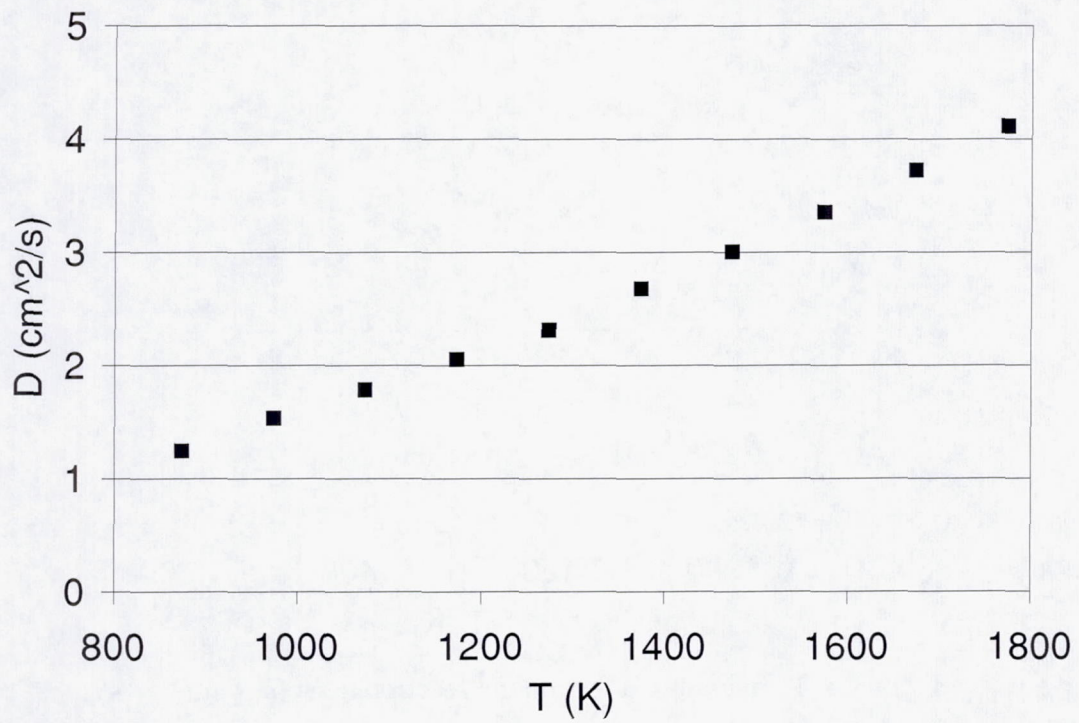


Figure 4. Temperature effect on the diffusion coefficient.

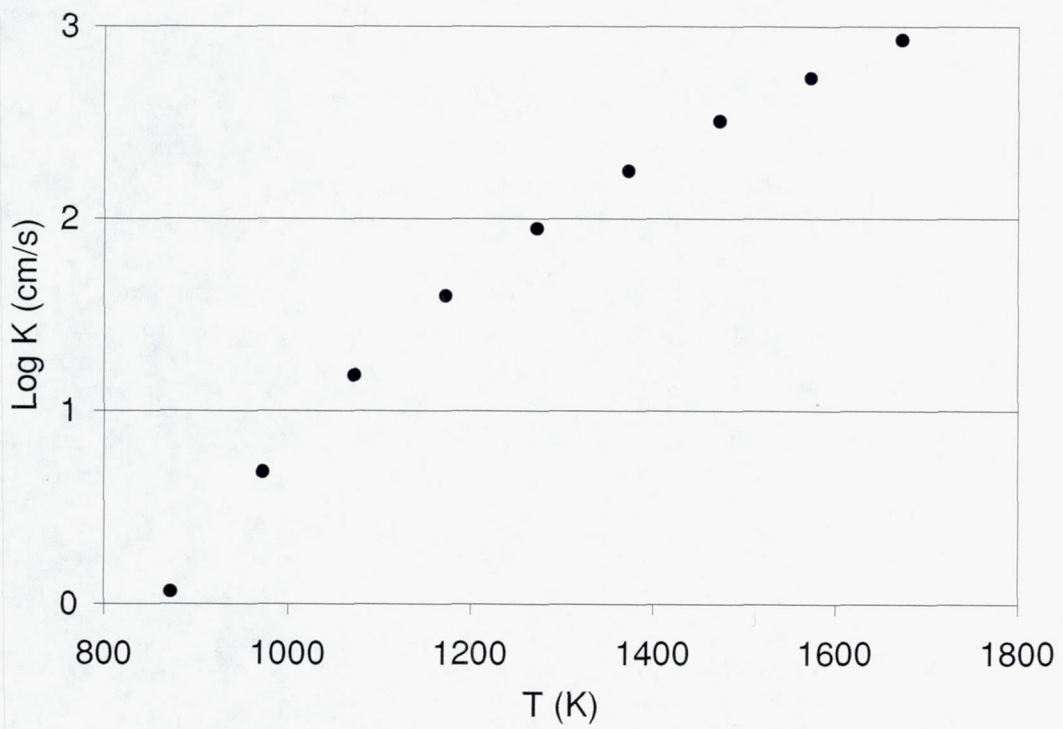


Figure 5. Temperature effect on the reaction rate constant.

# Anticipated Temperature Dependence

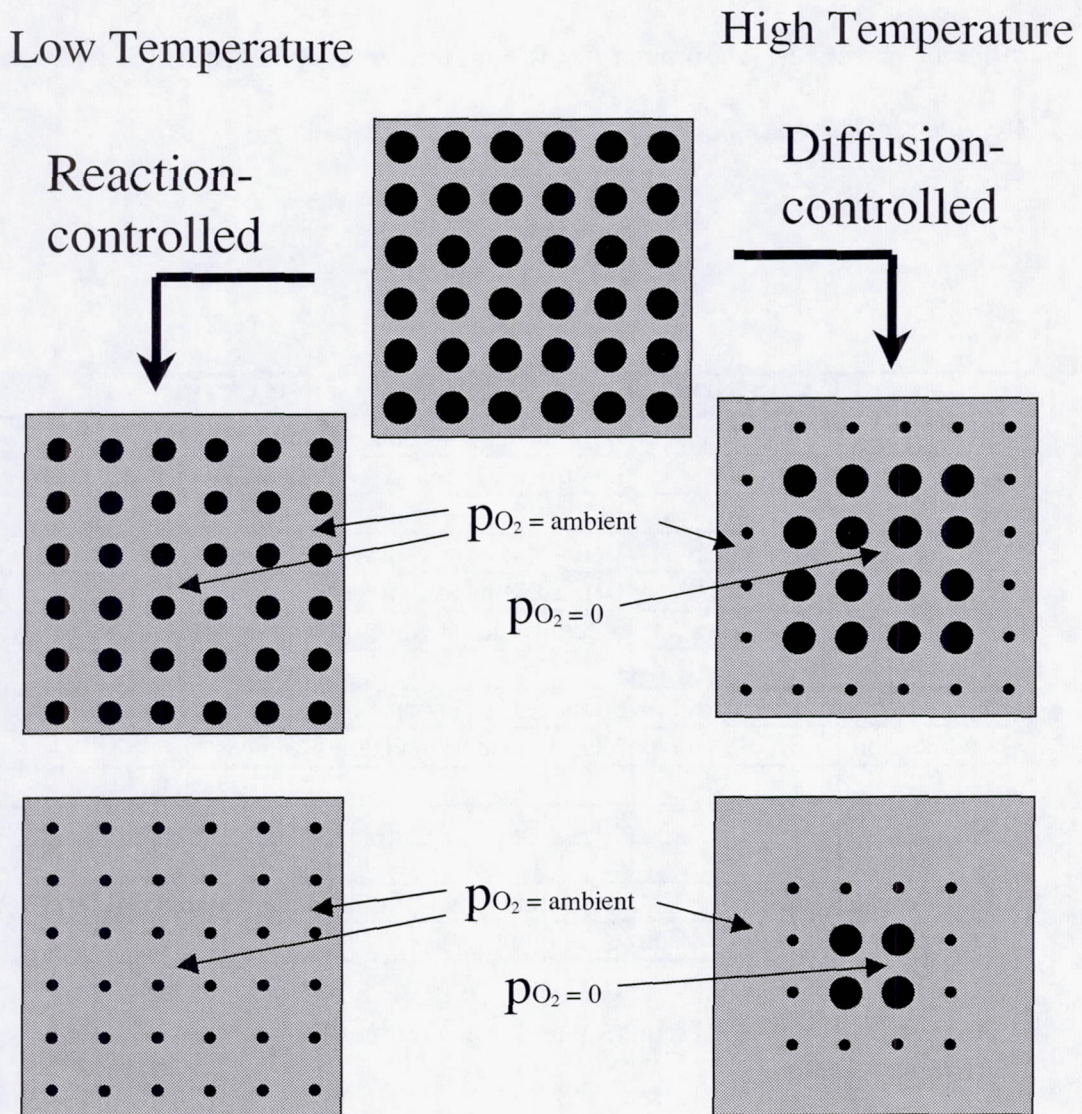


Figure 6. Illustrations of the oxidation of an array of fiber tows for reaction-controlled and diffusion-controlled kinetics.

## 2. EXPERIMENTAL STUDIES OF C/SiC

### 2.1 Materials and Experimental

Several types of tests were conducted. Each type of test may have had several different objectives. A summary of the experimental tests conducted and the objectives are given in Table II.

	TEST	MATERIAL	OBJECTIVE
1	TGA	T-300 carbon	Determine fiber's susceptibility to oxidation
		fiber	Identify oxidation kinetics regimes
2	TGA	C/SiC	Determine fiber's susceptibility to oxidation when in a matrix
			Determine matrix effects
			Study oxidation when the composite is not under stress
3	Stressed	C/SiC	Study oxidation when the composite is under stress
	Oxidation		Identify oxidation kinetics regimes
4	Creep	C/SiC	Study inelastic strain in material in inert and air environments
5	Stressed	4 different	Determine effect of oxidation inhibitors
	Oxidation	C/SiC Materials	

Table II. Objectives of experimental tests conducted on carbon fiber and C/SiC composite material.

### 2.1.1 TGA of T-300 Carbon Fiber

Thermogravimetric analyses (TGA) of carbon fibers were conducted. A sample of approximately 0.4 grams of continuous carbon fiber was taken from a spool of T300 carbon fiber in a 1K tow. The carbon fiber sample was placed in an alumina basket and suspended in a TGA furnace by a platinum wire. With the material already in the furnace, the furnace was brought to the desired temperature and maintained for the duration of the test. The tests were conducted in an oxygen environment where oxygen was flowing at 100 cc/min. through a 2.54 cm (1.0") diameter tube. The temperatures of interest were 500°C, 550°C, 600°C, 650°C, 700°C, 750°C, 800°C, 900°C, 1000°C, 1100°C, 1200°C, 1300°C, and 1400°C. Weight change in relation to time was recorded. The tests were allowed to continue until the carbon was completely consumed.

### 2.1.2 TGA of C/SiC Coupons

Thermogravimetric analysis was also conducted on C/SiC coupons in order to determine the effect of the presence of a cracked matrix. These tests also enabled oxidation studies to be conducted for when the composite material is not under stress. The composite material consisted of T300 carbon fibers in a silicon carbide matrix. The C/SiC materials were fabricated by DuPont-Lanxide Composites (now known as Honeywell Advanced Composites, Inc.). The T300 fiber preforms had a 0/90 degree weave. A pyrolytic carbon interphase was applied onto the fibers by chemical vapor deposition (CVD). The silicon carbide matrix was applied by chemical vapor infiltration (CVI). After fabrication of the C/SiC panel, test coupons were machined from the panel. Once the coupons were cut from the panel, an external seal-coating of silicon carbide was applied by chemical vapor deposition to seal the machined edges and holes in the case of

TGA coupons. TGA coupons were approximately 2.54 cm (1.00") in length, 1.27 cm (0.50") in width and were 0.33 cm (0.13") in thickness and had a machined hole toward one end which allowed the sample to be suspended by a platinum wire into the TGA furnace. Tests on the C/SiC coupons were conducted in the same oxygen environment as for the T-300 carbon fiber (oxygen flowing at 100 cc/min. through a 2.54 cm, 1.0", diameter tube). The temperatures of interests were 550°C, 600°C, 650°C, 700°C, 750°C, 800°C, 900°C, 950°C, 1000°C, 1100°C, 1250°C, and 1400°C. Weight change over time was recorded until the carbon fiber was completely consumed from the silicon carbide matrix or until 25 hours had elapsed.

### 2.1.3 Stressed Oxidation of C/SiC Coupons

Another type of test, stressed oxidation, was conducted on the DuPont-Lanxide C/SiC material and provided the other data needed to compare the susceptibility of the carbon fiber to oxidation when the composite material is unstressed (TGA of C/SiC) and stressed (stressed oxidation of C/SiC). The stressed oxidation tests (also known as creep rupture tests) put the material under a tensile stress so that matrix cracks are open and allow for easier ingress of oxygen into the material. Tensile bar coupons of C/SiC were loaded into an Instron 8500 Servo-Hydraulic load frame with hydraulic, water-cooled wedge grips. The dog-bone shaped tensile bars had dimensions of approximately 15.24 cm (6.00") long, 1.02 cm (0.40") wide in the gage section, and 0.33 cm (0.13") thick. A SiC susceptor coil placed circumferentially around the gage section of the sample was used to heat the gage section. Instrumentation was placed within the gage section of the sample. Thermocouples were placed at the front and rear face of the sample to monitor temperature. Extensometers with 1.27 cm (0.5") spaced probes were

placed on both edges of the sample and were used to monitor strain. Tests were conducted in an air environment. Gage sections of the tensile bars were brought to the desired temperature of either 350°C, 550°C, 750°C, 1000°C, 1250°C, 1400°C, and 1500°C. Once at temperature, a tensile stress of either 69 MPa (10 ksi) or 172 MPa (25 ksi) was applied. Samples were allowed to remain under stress at an elevated temperature until they failed or until 25 hours had elapsed. Strain, constant load, and temperature were recorded over time. Samples that survived 25 hours were fractured at room temperature to determine their residual strength.

#### 2.1.4 Creep of C/SiC Coupons

Tests comparable to stressed oxidation tests were conducted except the environment was non-oxidizing. Creep tests were conducted on the DuPont-Lanxide C/SiC material in an inert (argon) environment. Tensile bar coupons were tested at a temperature of 750°C and stresses of either 69 MPa (10 ksi) or 172 MPa (25 ksi). These tests were conducted in order to determine if the changes in strain that were observed in an air environment could be attributed exclusively or principally to oxidation damage effects or whether creep damage effects also play a role. The tests were conducted in the same rig and with the same instrumentation as for the stressed oxidation tests. The inert tests conducted at 750°C were compared to the stressed oxidation tests conducted at the same temperature.

#### 2.1.5 Stressed Oxidation of Four Different C/SiC Materials

Stressed oxidation tests were also conducted on four different C/SiC materials. The constituents and processing properties can be seen in Table III. Materials A, C, and D were fabricated by DuPont-Lanxide Composites (DLC). Material B was fabricated by

B. F. Goodrich (BFG). All materials had a 0/90 degree plain weave preform of T300 carbon fibers in 1k tows. They all also had a carbon interphase, a CVI SiC matrix, and a SiC external seal-coating. Material A was DLC's standard C/SiC material which did not have any type of oxidation inhibitor. This was the same type of C/SiC material used in the previously discussed TGA and stressed oxidation testing conducted across the wide temperature ranges. Material B was a BFG C/SiC material said to have some type of proprietary oxidation inhibitor believed to be at the interphase level. Material C was DLC's enhanced C/SiC material which had an oxidation inhibitor in the form of boron containing particulates in the matrix. Material D was DLC's enhanced C/SiC material with the addition of a CBS external coating. This material had two forms of oxidation inhibitors. The first was boron-containing particulates in the matrix. The second was an external seal coating that consisted of carbon, boron, and silicon. For the purposes of this work, materials A and B were classified as materials without boron containing oxidation inhibitors and materials C and D were classified as materials with boron containing oxidation inhibitors. Stressed oxidation tests were conducted in the same manner as previously discussed however only one temperature was studied. Tests were conducted at a temperature of 1454°C and a stress of either 69 MPa (10 ksi) or 172 MPa (25 ksi). Coupons that survived 25 hours of exposure were fractured at room temperature to determine the residual strength.

A                      B                      C                      D

MATERIAL	STD C-SiC	C-SiC	ENH C-SiC	ENH C-SiC w/CBS
MANUFACTURER	DUPONT LANXIDE	BF GOODRICH	DUPONT LANXIDE	DUPONT LANXIDE
YARN	1K T-300	1K T-300	1K T-300	1K T-300
YARN HEAT TREATMENT	NONE	1800°C	1700°C	
FIBER ARCH.	2D PLAIN	2D PLAIN	2D PLAIN	2D PLAIN
YARN ENDS PER INCH	19/IN	19/IN	19/IN	19/IN
INTERFACE COATING	PyC ALPHA - 3	PyC	PyC ALPHA - 3	PyC ALPHA - 3
MATRIX	SiC	SiC	SiC	SiC
DENSIFICATION	ISOTHERMAL CVI	ISOTHERMAL CVI	ISOTHERMAL CVI	ISOTHERMAL CVI
OXIDATION INHIBITOR	NO	YES	YES	YES
COATING	CVIP	CVD SiC	CVIP	CVIP

Table III. Constituents and processing properties of four different C/SiC materials. A and B do not have boron containing oxidation inhibitors. C and D do have boron containing oxidation inhibitors.

## 2.2 Results

### 2.2.1 TGA of T-300 Carbon Fibers

The results of the TGA tests of the T300 fiber are shown in Figure 7. The carbon was completely consumed in less than two hours for all temperatures. Two distinct regimes were seen. In regime 1, which occurs in the temperature range of 500°C-600°C, there was a strong temperature dependence. The oxidation rate increased incrementally with each temperature step. However in regime two, which occurred from 600°C-1400°C, there was less of a temperature dependence. The rate of weight loss was similar for all temperatures in this range. Some of the lower temperature exposures in this range had slightly steeper curves than those for higher temperature exposures. This could be due to the furnace heat up rate or the timing of the data for each curve on the overall plot. Apart from this, the results show a very weak temperature dependence for regime 2. It is noted that the transition between regime 1 and regime 2 is sometimes considered a separate regime called the transition regime.

### 2.2.2 TGA of C/SiC Coupons

The results of the TGA testing on the standard C/SiC materials are shown in Figure 8. At 550°C-700°C the carbon reactivity increased as the temperature was increased. At 700°C-800°C, there was little temperature dependence and complete carbon burnout occurred in about five hours. As the temperature of 1100°C was approached, the oxidation rate of carbon decreased. The oxidation rate was the lowest at 1100°C and only a 1% reduction in weight was observed after 25 hours of exposure at this temperature. As the temperature was increased beyond 1100°C, the oxidation rate began to slightly increase however, the weight loss was still less than 5 % compared to

the 40-50 % weight change needed for complete carbon consumption. It should be noted that the sample tested at 750°C was from a different batch of fiber and had a fiber loading of approximately 42 wt% compared to a fiber loading of approximately 50 wt% for the other samples.

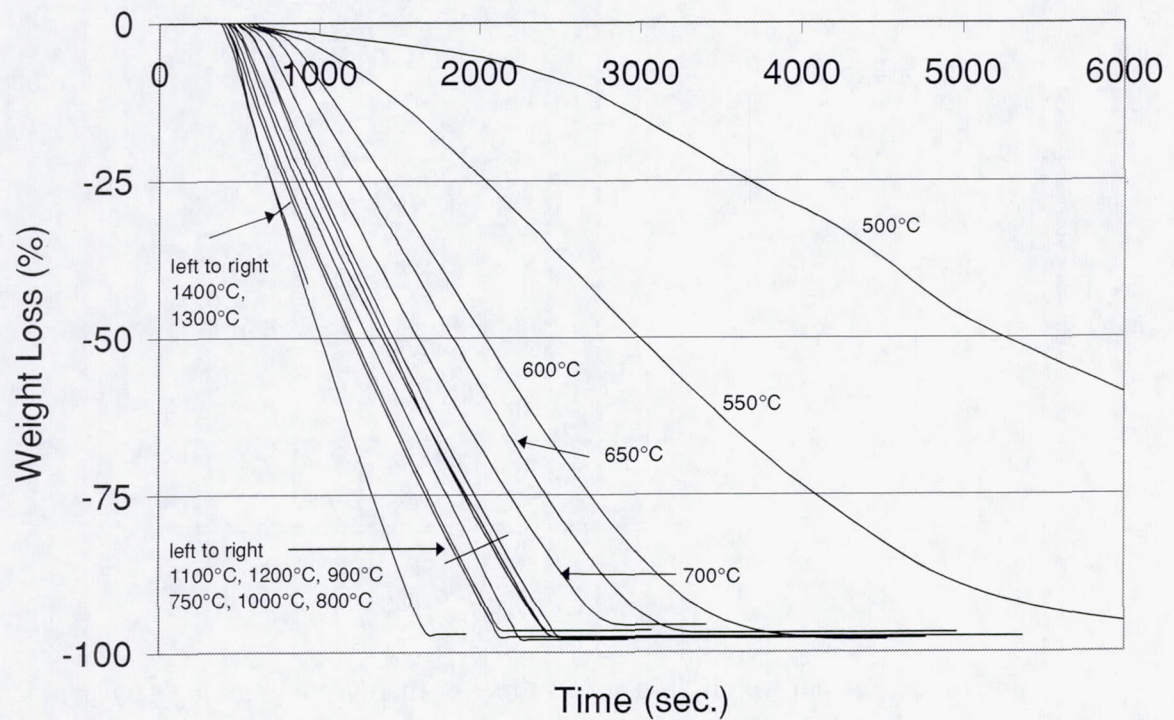


Figure 7. Percent weight loss versus time for the thermogravimetric analysis of T300 carbon fiber in a flowing oxygen environment.

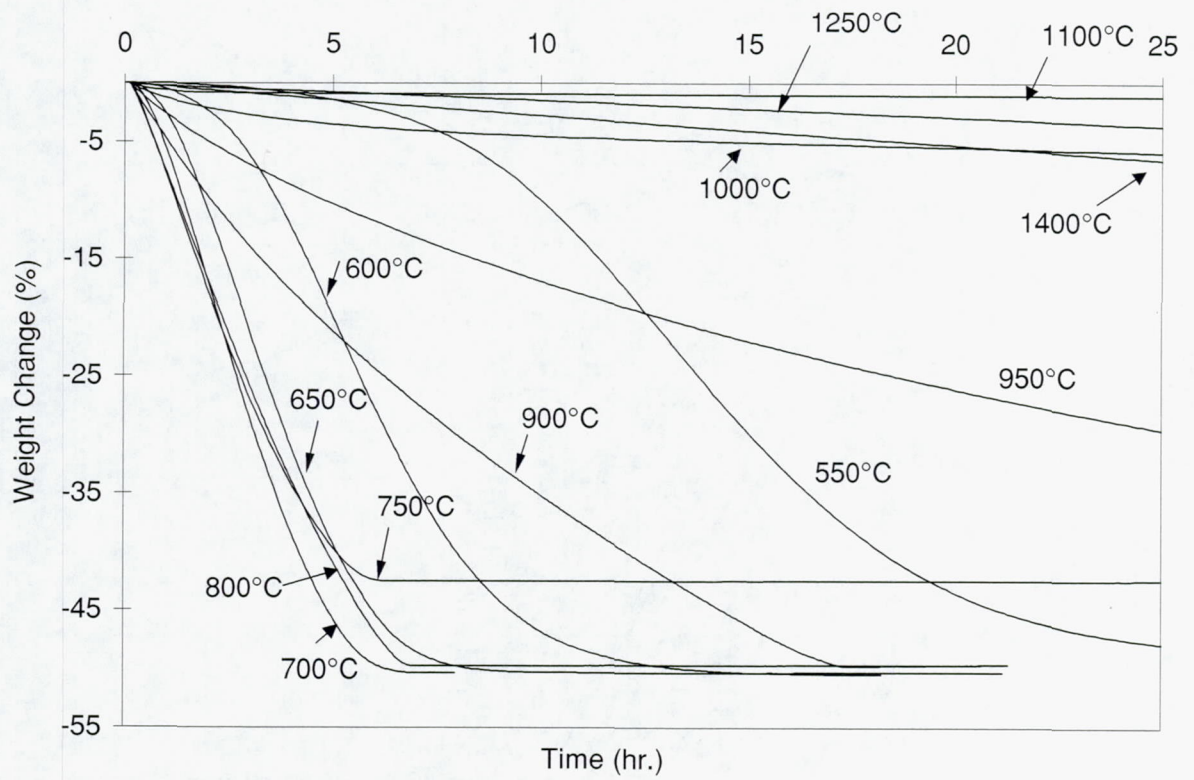


Figure 8. Percent weight loss versus time for thermogravimetric analysis of C/SiC coupons in a flowing oxygen environment.

### 2.2.3 Stressed Oxidation of C/SiC Coupons

The results of the stressed oxidation tests of the C/SiC material are shown in Table IV and Table V for the stresses of 69 MPa and 172 MPa respectively. The strains and times to failure are given for all tests conducted. The samples that survived 25 hours of exposure were fractured under tension at room temperature to determine the residual strength. The data suggest two regimes. In regime 1, temperatures from 350°C to 750°C, there was a strong temperature dependence. Samples tested at 350°C did not show any signs of oxidation and had residual strengths comparable to the as-received tensile strength of two samples which were 351 and 406 MPa. At 550°C, the sample tested at the lower stress of 69 MPa survived 25 hours however it lost half of its strength compared to the strength of the two as-received tensile bars. The sample tested at the higher stress at this same temperature failed at the 25 hour mark. At the higher temperature of 750°C, there was a sharp drop in sample life with the sample tested at 69 MPa failing after 91 minutes and the sample tested at 172 MPa failing after 22 minutes. In regime 2, temperatures from 750°C-1500°C, there was less of a temperature dependence in the times to failure. The times to failure in this range remained relatively short although there was a modest variation in the times to failure with the times to failure increasing up to the temperature of 1250°C and then decreasing at higher temperatures. It should be noted that the strains to failure appeared to have a strong temperature dependence throughout the overall temperature range. While the stress did have a significant effect on the times to failure, it did not have a significant effect on the strains to failure. The strains to failure are similar at each temperature for both stress conditions. This was despite the higher stress being two and a half times the value of the

lower stress. Also a trend of strain to failure increasing with temperature is observed at both stresses. It should be noted that all strain versus time plots in this thesis include the mechanical strain due to load-up.

The strain versus time curves for the stressed oxidation tests are shown in Figure 9-11. The curves for the lower temperature tests (350°C and 550°C) in which lives were longer are shown in Figure 9. The curves for the higher temperature tests are shown in Figure 10 for the 69 MPa tests and Figure 11 for the 172 MPa tests. The increase in strain to failures with temperature can be seen in the plots. In Figure 10, the curves for samples tested at temperatures above 750°C at a stress of 69 MPa show a shape reminiscent of that expected when the three classic changes in strain rate often observed during the classical creep of metals are present: primary, secondary, and tertiary. For the higher stress tests in Figure 11, the individual "creep" regimes are more difficult to distinguish.

Test Temp. °C	Time to Failure	Strain to Failure (%)	Residual Strength MPa
1500	65 min.	0.930	
1400	86 min.	0.757	
1250	142 min.	0.750	
1000	124 min.	0.324	
750	91 min.	0.209	
550	25+ hr.		192
350	25+ hr.		382

Table IV. Times to failure and strains to failure for the stressed oxidation of C/SiC coupons in air at a stress of 69 MPa (10 ksi).

Test Temp. °C	Time to Failure	Strain to Failure (%)	Residual Strength MPa
1500	17 min.	1.000	
1400	28 min.	0.910	
1250	36 min.	0.944	
1000	22 min.	0.359	
750	22 min.	0.363	
550	25 hr.	0.450	
350	25+ hr.		403

Table V. Times to failure and strains to failure for the stressed oxidation of C/SiC coupons in air at a stress of 172 MPa (25 ksi).

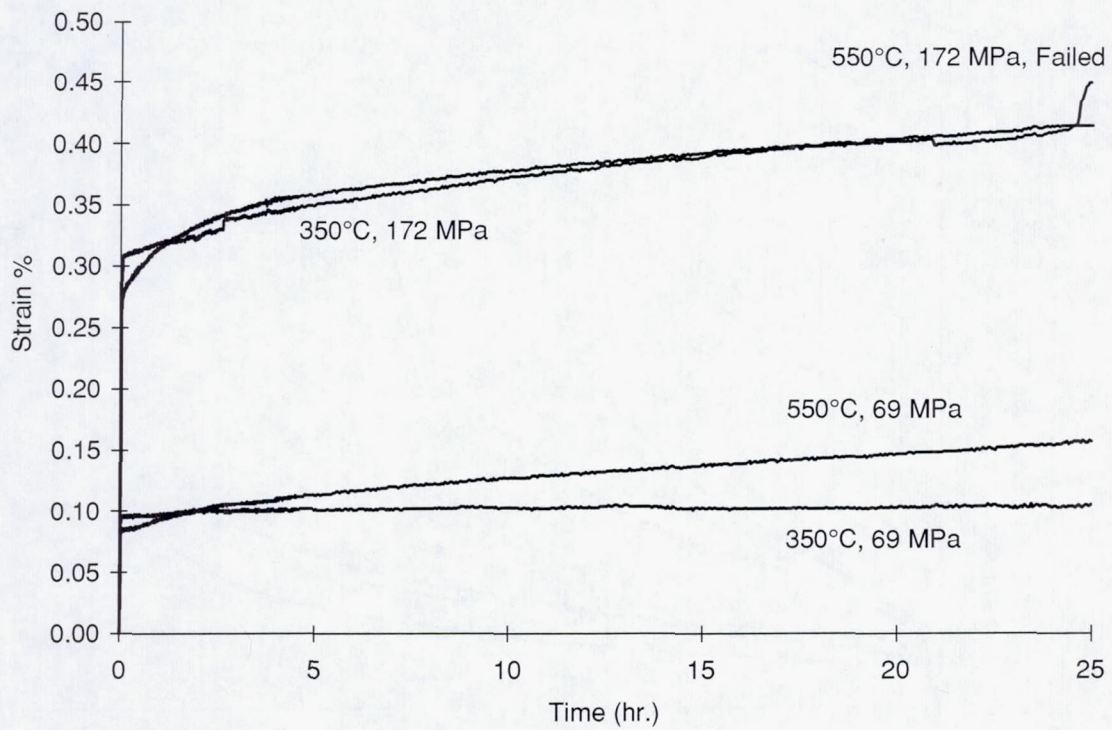


Figure 9. Strain versus time curves for the stressed oxidation of C/SiC test coupons at temperatures of 350°C and 550°C and stresses of 69 MPa and 172 MPa.

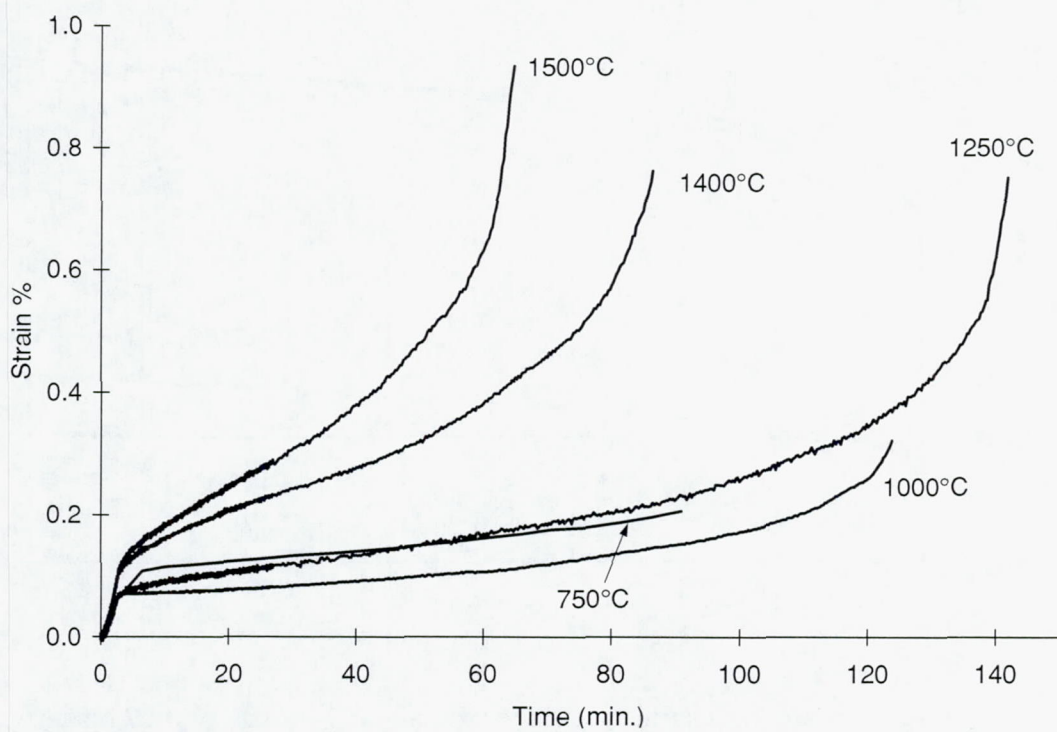


Figure 10. Strain versus time curves for the stressed oxidation of C/SiC test coupons at temperatures of 750°C to 1500°C and a stress of 69 MPa.

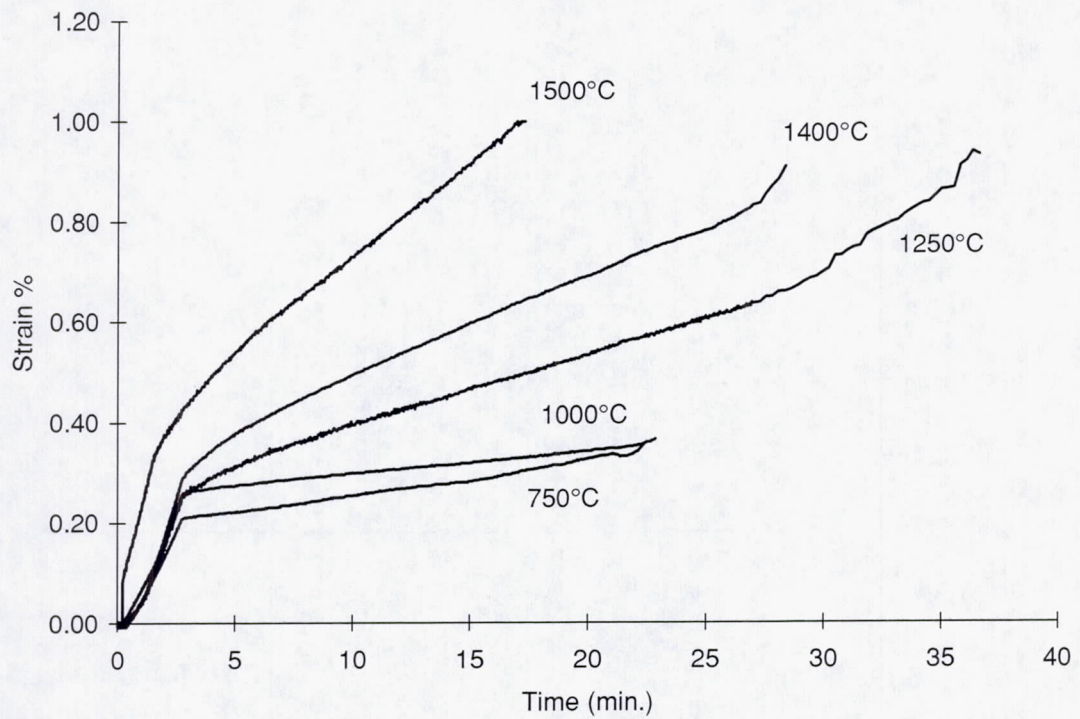


Figure 11. Strain versus time curves for the stressed oxidation of C/SiC test coupons at temperatures of 750°C to 1500°C and a stress of 172 MPa.

#### 2.2.4 Creep of C/SiC Coupons

The creep tests were conducted in argon at the temperature of 750°C and stresses of 69 MPa and 172 MPa. The results are shown in Figure 12. The tests conducted in the inert environment showed no significant increase in strain for the 25 hours of exposure after they were brought to load. The two samples that were held at 69 MPa and 172 MPa for 25 hours had residual strengths at room temperature that were comparable to the as-received tensile strengths.

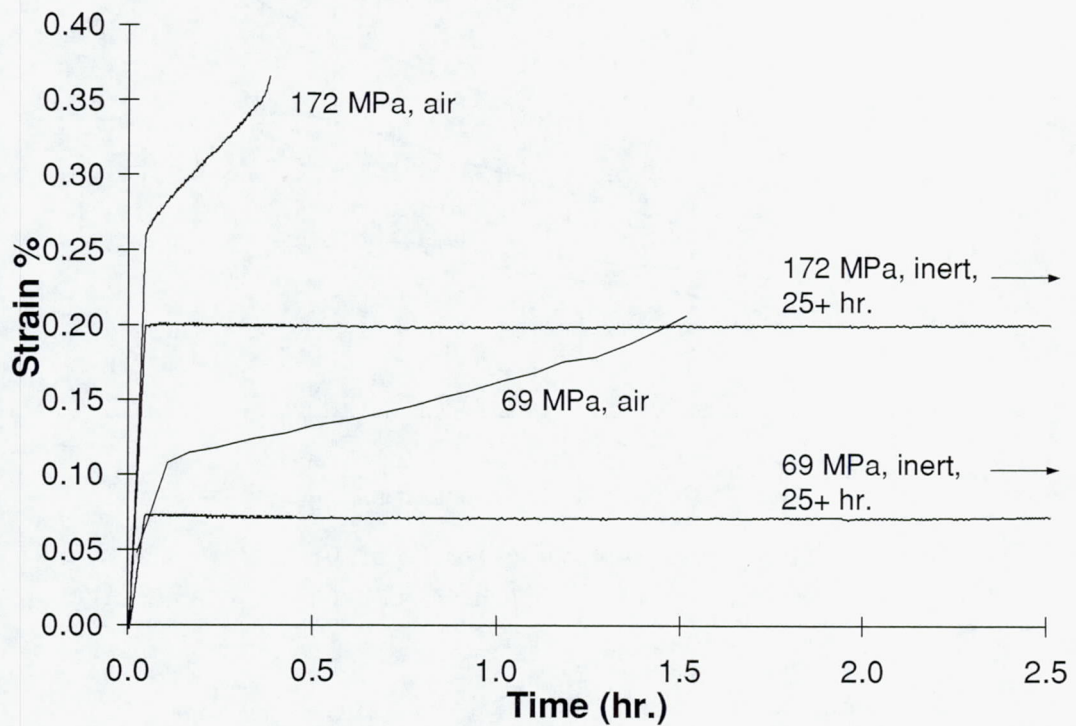


Figure 12. Creep tests of C/SiC coupons at 750°C in air and inert environments.

### 2.2.5 Stressed Oxidation of Four Different C/SiC Materials

The times to failure for the four different C/SiC materials are shown in Figure 13 for the stress of 69 MPa and in Figure 14 for the stress of 172 MPa. The two materials without boron containing oxidation inhibitors, materials A and B, had relatively short lives at both stresses. These short lives were comparable to the short lives obtained for the stressed oxidation of C/SiC at similarly high temperatures, 1400°C and 1500°C, in air as was shown in Figures 10 and 11 and Tables IV and V. However the two materials which did have boron containing oxidation inhibitors, materials C and D, had much longer lives at the stress of 69 MPa. These materials survived 25 hours and had high residual strengths. At the higher stress of 172 MPa, only material D performed significantly better than the other materials. It had lives in the teens of hours, while the other materials either failed load up or failed in less than two hours.

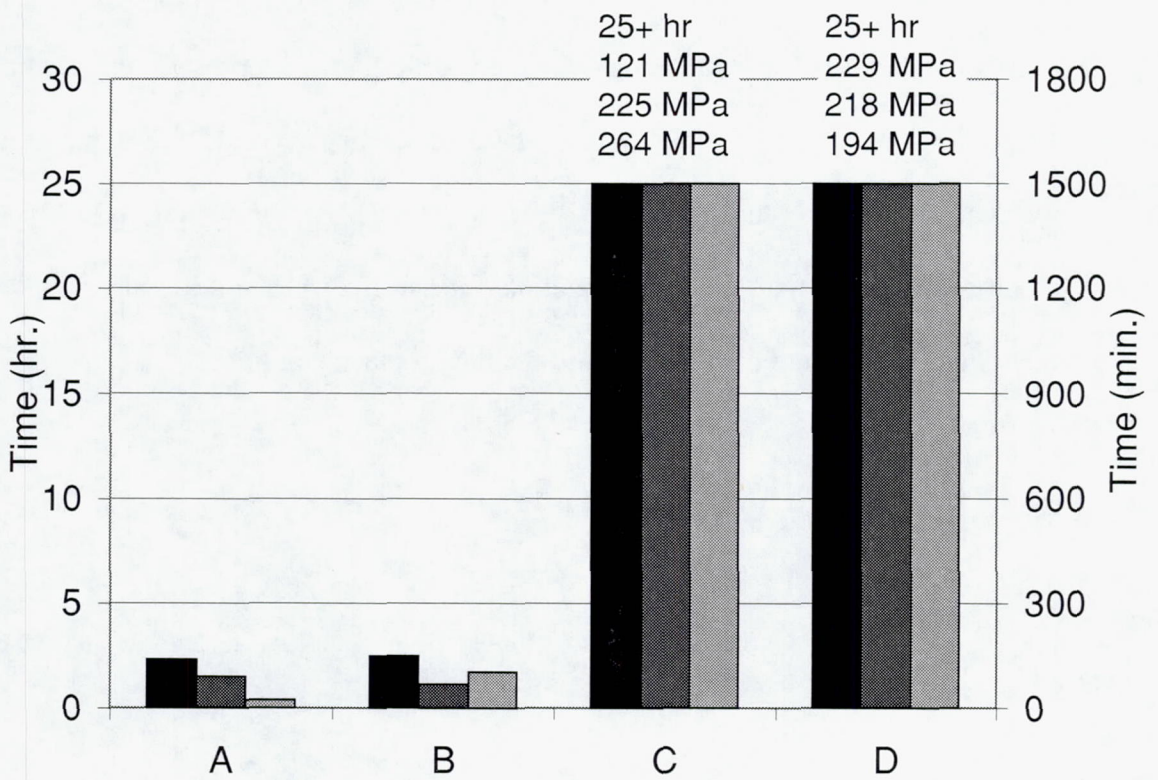


Figure 13. Times to failure for the four different C/SiC materials at a temperature of 1454°C and a stress of 69 MPa. Materials A and B did not have boron containing oxidation inhibitors while materials C and D did. Residual strengths of C and D are given.

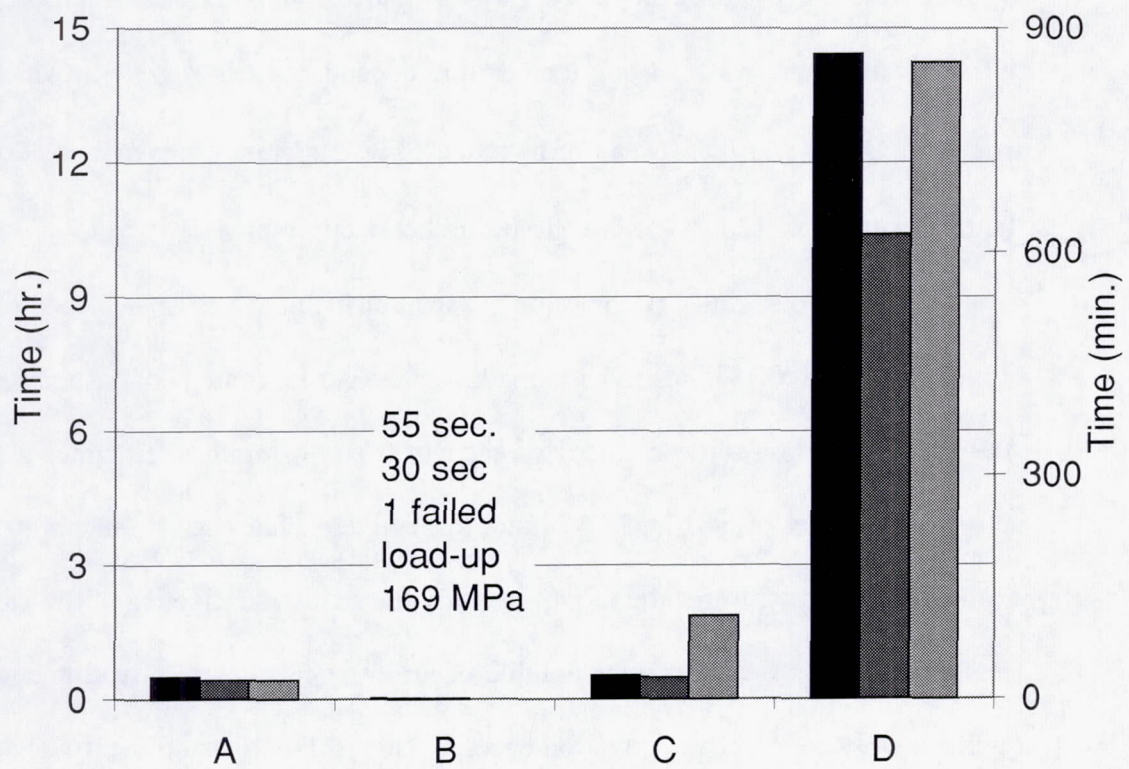


Figure 14. Times to failure for the four different C/SiC materials at a temperature of 1454°C and a stress of 172 MPa. Materials A and B did not have boron containing oxidation inhibitors while materials C and D did.

## 2.3 Discussion

### 2.3.1 TGA of T-300 Carbon Fiber

The results of the TGA tests in an oxygen environment for the bare T-300 carbon fiber show the susceptibility of carbon to oxidation at temperatures as low as 500°C. Other studies have shown that carbon will oxidize at temperatures as low as 500°C-550°C (Lamouroux *et al.*, 1993; Shemet *et al.*, 1993; McKee, 1998). Two distinct regimes were suggested by the data shown in Figure 7. In regime 1, which occurred from 500°C-600°C, there was a strong temperature dependence. In regime 2, which occurred from 600°C-1400°C, there was not as much of a temperature dependence especially in the range of 800°C-1200°C where curves did not occur in order.

These two regimes become more apparent in Figure 15 in which the  $\ln K_l$  was plotted against  $10,000/T$  where  $K_l$  is the linear weight loss rate and  $T$  is the temperature. Activation energies were obtained for each of the two regimes. Regimes 1 and 2 had activation energies of 64.1 and 7.6 kJ/mol respectively. The activation energy for regime 1 was used as an input for the model to study the oxidation kinetics of the carbon fiber. Regime 2 only shows that a transition did occur. The calculated activation energy in this regime is only an effective activation energy. This is due to using linear weight loss data to analyze a parabolic regime (regime 2). Also, the regime 2 data does not fall perfectly on the line due to the relation to temperature not being an exponential relation as plotted. As pointed out in the introduction and by Eckel, the diffusion coefficient has a  $T^{2/3}$  dependency on temperature. Eckel suggest force fitting the diffusion coefficient to an Arrhenius form such that a theoretical effective activation energy based on the diffusion coefficient can be determined for the diffusion-controlled regime (Eckel, 1998).

Other researchers have obtained variations on the activation energies and the regimes. Ismail reports an activation energy of 94.1 kJ/mol for T-300 in the temperature range of 600°C-950°C in an air environment flowing at 100 cc/min (Ismail, 1991). Although the reported value is higher than for the current results, Ismail's range of temperatures and the presence of one activation energy in this range agrees with the currently determined regime 2 which occurred in the same temperature range. Lamouroux *et al.* had activation energies of 80 kJ/mol across the temperature range of 500°C-700°C and 15 kJ/mol across the temperature range of 700°C-900°C for the oxidation of T-300 fiber in an oxygen environment (Lamouroux, *et al.*, 1993). Lamouroux's values for the activation energies are more compatible to those obtained in this work. The difference between Lamouroux's transition from regime 1 to 2 and currently presented transition from regime 1 to 2 can be due to the flow rate of the oxygen. Lamouroux's flow rate of 16.7 cc/min was much lower than the rate of 100 cc/min used in the experimental part of this thesis. Both sets of experiments were conducted at 1 atmosphere ( $1.0 \times 10^5$  Pa).

When the flow rate is lowered, the flux of oxygen will be lowered. Therefore as the flow rate is lowered, the transition from regime 1 to regime 2 will occur at a higher temperature. This effect can also be realized by considering the Sherwood number (sometimes referred to as the mass transfer Nusselt number) which is a dimensionless concentration gradient at the surface:

$$Sh = \frac{h \Delta x}{D_{AB}} \quad (10)$$

where  $h$  is the mass transfer coefficient (m/s) which in this case is equivalent to the reaction rate constant of carbon,  $K$  (m/s),  $\Delta x$  is a characteristic length which is dependent on the geometry of the system being analyzed (m), and  $D_{AB}$  is the diffusion constant for the binary gas mixture of the reactant gas of oxygen and the product gas of the oxide (either CO or CO<sub>2</sub>) (m<sup>2</sup>/s). The effect on the velocity on the Sherwood number can be considered when one realizes that the Sherwood number for a prescribed geometry is a function of the Reynolds (Re) and the Schmidt (Sc) numbers (Incropera and Dewitt, 1985; Gaskell, 1982):

$$Sh = f(\Delta x, Re, Sc) \quad (11)$$

so that the local Sherwood number ( $Sh_x$ ) for the case of laminar flow in fluids ( $0.6 \leq Sc \leq 50$ ) is

$$Sh_x = 0.332 D_{AB} Sc^{0.343} Re^{1/2} \quad (12)$$

The Schmidt number is the ratio of viscous momentum transport,  $\nu$  (m<sup>2</sup>/s), and mass diffusivities such that

$$Sc = \frac{\nu}{D_{AB}} \quad (13)$$

The Reynolds number is the ratio of the inertia and viscous forces such that

$$Re = \frac{V_x \Delta x}{\nu} \quad (14)$$

where  $V_x$  is the velocity of the gas (m/s) and again  $\Delta x$  is a characteristic length (m) and  $\nu$  is the viscous momentum transport (m<sup>2</sup>/s). Therefore, by substituting Equations (13) and (14) into Equation (12), it is seen that an increase in velocity will increase the Sherwood number and therefore cause the transition from regime 1 to regime 2 or from reaction-controlled kinetics to diffusion-controlled kinetics to occur sooner (at a lower

temperature) than for low velocity gases. For low velocity gases, the transfer in kinetics will occur at a relatively higher temperature compared to the transfer temperature obtained for high velocity gasses. This can be seen by comparing the TGA data conducted here to that of Lamouroux. Assuming flow through a tube with a diameter of 2.56 cm for both studies, Equation (12) gave a Sherwood number almost 2.45 times higher when the flow was 100 cc/min compared to when it was 16.7 cc/min. From the calculated values in Table 1, it is seen that if the Sherwood number at 600°C,  $4.68 \times 10^{-3}$ , is multiplied by 2.45, a value of  $1.15 \times 10^{-2}$ , is obtained which approaches the value for the Sherwood number at 700°C,  $1.57 \times 10^{-2}$ . Therefore the oxygen flow rate can account for the differences in the transition temperature for Lamouroux's work and this current work.

Other differences in activation energies and the transition temperatures among published data may be due to the carbon reactivity being dependent on several variables. The variables include impurity level, crystal structure, carbon surface, environment, temperature, and pressure (Ismail, 1991; Eckel *et al.*, 1995; Shemet *et al.*, 1993). In a summary of published data (Shemet *et al.*, 1993) on the activation energy of carbon materials, it is seen that reported activation energies range from 8-184 kJ/mol for temperatures from 400°C-1000°C. Some researchers who conducted studies across most of this temperature range reported obtaining only one activation energy while others had two activation energies (an activation energy and an apparent activation energy).

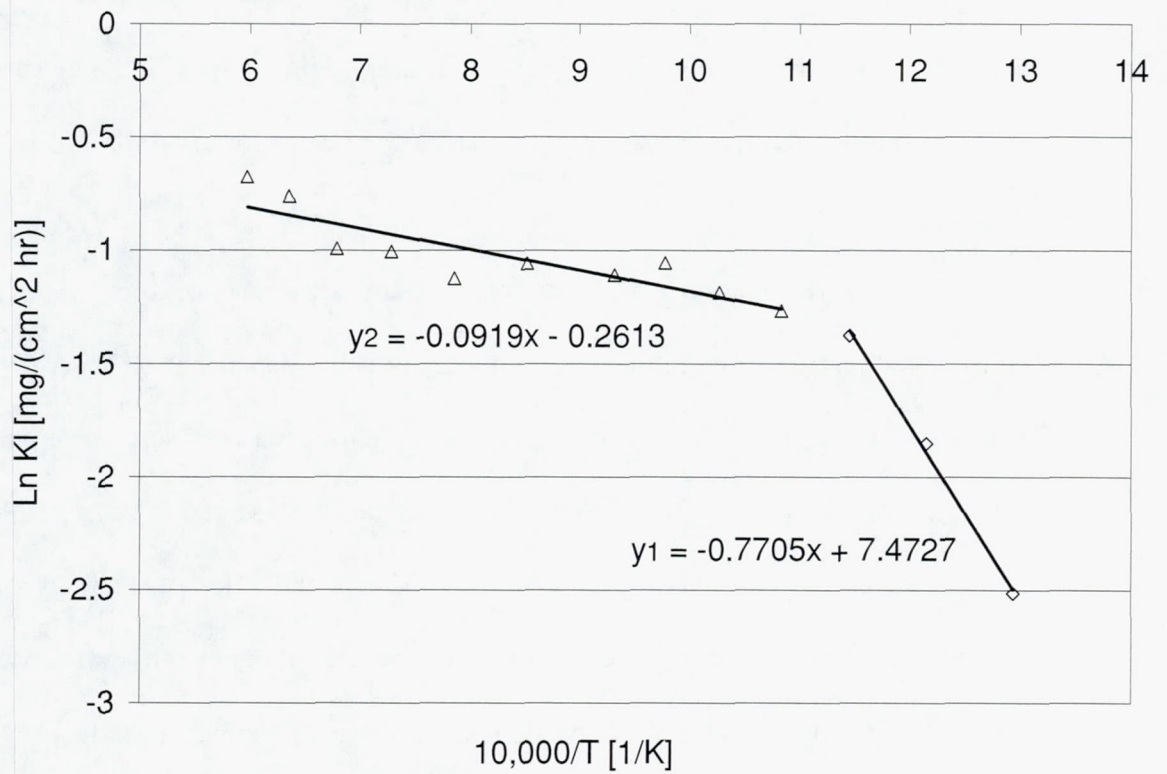


Figure 15. Determination of the activation energy of T300 carbon fiber.

### 2.3.2 TGA of C/SiC Coupons

All of the TGA results for the oxidation of C/SiC test coupons in Figure 8 are not what would initially be expected based on the results for the bare fiber in Figure 7. As expected, there was a temperature dependence on the oxidation rate at low temperatures, i.e., between 550°C-700°C. At temperatures of 750°C-800°C, the oxidation rates were slightly higher than for 700°C, but there seemed to be no significant temperature dependence and fiber burnout occurred within several hours for all of these temperatures. However as temperature was further increased, the expected trend of increasing oxidation rate was not seen. Instead, the oxidation rates decreased and there was a significant temperature dependence as the temperature approached 1100°C. At this temperature, the weight loss after 25 hours was the lowest among all tests with the weight loss only being 1%. As temperature was increased above 1100°C, the oxidation began to slightly increase however the weight loss after 25 hours was still relatively low for these high temperatures.

The trends for C/SiC weight loss in TGA tests can be explained by matrix effects. As the test temperature reaches the processing temperature (approximately 1100°C), thermal stresses are relieved and the matrix cracks begin to close as the thermal expansions of the fibers and matrix go back to the expansion that they were at when processed. At the processing temperature, crack edges have come together and seal off the supply of oxygen. Since crack edges may not align perfectly with one another, the fibers may not be completely sealed off from the supply of oxygen so oxidation of fibers may still occur. However the carbon oxidation rate will be greatly reduced as the cracks approach closure. Eckel *et al.* have shown that parabolic reaction rates begin to be

reduced once pores (crack openings) reach sizes below 1 micron and are greatly reduced once pore sizes of 10 nanometers are reached (Eckel *et al.*, 1995). Another effect of the matrix cracks was the growth of a silica scale ( $\text{SiO}_2$ ) as the SiC matrix oxidizes. The growth of the oxide scale can fill in cracks at temperatures sufficient for oxide growth and seal off the fibers from the outside environment. In the temperature range of 800°C-1100°C, the kinetics for the oxidation of SiC and the growth of  $\text{SiO}_2$  are linear while for temperatures above 1100°C, the kinetics are parabolic (Ogbuji and Opila, 1995). The minimal weight loss in the C/SiC coupon at the temperature of 1100°C is at a temperature near the presumed processing temperature and is also in the parabolic growth regime for the  $\text{SiO}_2$  scale. At higher temperatures, the oxidation rate was seen to increase and may be due to overexpansion of the SiC matrix relative to the carbon fibers. Compression of the crack edges can put a tensile stress on the fibers and cause a shift in the material so that crack edges become out of alignment and oxygen has a wider opening for ingress to the fibers. Despite the growth of the oxide scale, some oxidation is still to be expected at high temperatures due to the slow growth of oxides compared to the rate at which carbon oxidizes. TGA experiments on chemically vapor deposited SiC at temperatures of 1200-1500°C and at one atmosphere in air were conducted by Ogbuji and Opila to study the oxidation kinetics of SiC. They determined the thickness of the oxide scale on SiC after oxidation at 1300°C for 75 hr to be 1.6 micrometers (Ogbuji and Opila, 1995).

### 2.3.3 Stressed Oxidation of C/SiC Coupons

In the TGA results, the susceptibility of carbon to oxidation and two kinetic regimes were observed across the entire temperature range (550°C-1400°C) for the bare carbon fibers while self protecting matrix effects were observed for the unstressed C/SiC

coupons. The stressed oxidation results for the C/SiC coupons under a tensile load showed that the presence of a stress greatly diminishes the matrix effects and allows oxidation regimes to be observed that were similar to those seen for the oxidation of bare carbon fiber. At temperatures from 350°C-750°C, the times to failure and residual strengths had a strong dependence on temperature. At temperatures higher than 750°C (i.e, 1000°C-1500°C), the times to failure were relatively short. Stressed oxidation results had two distinguishable regimes, similar to those observed for the oxidation of bare carbon fiber, and therefore also suggest two different rate controlling kinetics as carbon oxidizes. The maximum in times to failure at 1250°C may have to do with the processing temperature or matrix effects. The increase in time to failure at this temperature can be due to two factors. First, carbon strength is known to increase with temperature (Rodrigues *et al.*, 1995). Second, relief of processing related residual stresses may contribute to the increased strength (Camus and Barbier, 1995). An increase in strength would contribute to a longer life. It is interesting to note that a point of minimal oxidation was observed in the TGA tests of C/SiC coupons near the presumed processing temperature (1100°C).

#### 2.3.4 Creep of C/SiC Coupons

Tests were conducted in an inert environment in order to determine the contribution oxygen was having on the strains observed in the stressed oxidation tests. Figure 12 shows the results of testing at 750°C in air and inert (argon) environments. The two samples in the inert environment did not show any significant change in strain out to the 25 hr. when the tests were stopped. These results suggest that, for at least the temperature of 750°C, the strains occurring during stressed oxidation are due to

oxygen/carbon reactions. Work by Holmes et al. (Holmes and Morris, 1991) has shown the significant effect oxygen concentration can have on the life of this material. In their work, an order of magnitude reduction in sample life at 1400°C was observed when the oxygen level increased from 1 to 10 ppm.

Although there was no significant change in strain in the C/SiC material under stress in an inert environment at 750°C, the constituents of the carbon fiber and silicon carbide matrix have been observed by other researchers to creep at higher temperatures. PAN based carbon fibers have been found to creep at high temperatures (2100 to 2500°C) under high stresses (400 to 800 MPa). Pan-based carbon fibers have an apparent creep activation energy of 1058 kJ/mol (Sines *et al.*, 1989). The PAN-based material tested by Sines *et al.* that had stress exponent of 7.4. Sines *et al.* proposed that processes of graphitization and deformation of their PAN-based carbon fiber occurred by vacancy formation and motion. They propose that deformation took place by whole crystallites moving instead of individual atoms. Diffusion of irregularities on the atomic level at high temperatures allow for the sliding between neighboring atoms.

The silicon carbide matrix that is chemically vapor deposited into the fiber preform provides shape to the final CMC component and protects and supports the fibers. Silicon carbide does creep at high temperatures. Wilshire and Jiang conducted creep experiments of silicon carbide across a range of stresses at temperatures of 1400°C, 1500°C and 1600°C (1673, 1773, and 1873 K) and found the n-values in the power-law creep equation to be 2.5, 6.7, and 7.6 respectively (Wilshire and Jiang, 1994).

The diffusion of oxygen through microcracks and the oxygen reactions with the carbon fiber and interphase are the processes that lead to fiber oxidation. Oxygen

diffuses down the channels created by the microcracks. Oxygen reacts with the sections of the fiber that bridge the crack. The pyro-carbon interphase oxidizes first and then the fibers begin to narrow as the outer diameters oxidize away. The oxidation activation energy of a CVD deposited carbon interphase in a SiC/SiC composite was determined in TGA studies by Windisch *et al.* At oxygen pressures of  $2.5 \times 10^{-3}$  and  $1.2 \times 10^{-3}$  Pa the activation energy was 54 and 48 kJ/mol respectively (Windisch *et al.*, 1997). This activation energy is lower than typical values for bulk carbon. Investigators have noted the preferential oxidation of pyro-carbon interphases in ceramic matrix composites (Eckel *et al.*, 1995; Crocker and McMeaney, 1991; Lamouroux *et al.*, 1994). Glime and Cawley attribute the preferential oxidation of the pyro-carbon interface to the interface having a higher degree of disorder than bulk carbon and therefore a higher tendency to react with oxygen (Glime and Cawley, 1995).

### 2.3.5 Oxidation Patterns and Trends

The oxidation patterns of the carbon fibers discussed above were observed experimentally in the stressed oxidation tests of C/SiC and help explain the permanent non-plastic deformations/strains. In strain region I the strain rate decreases after the elastic extension during load up. In strain region II, the strain rate gradually increases. Oxygen that has entered the matrix through microcracks has begun to oxidize the pyro-carbon interphase and carbon fibers. Figure 16 is a micrograph of a polished cross-section of a tested sample that illustrates how carbon/oxygen reactions occur preferentially along microcracks. Figure 17 shows the early stages of oxidation of the interphase and the outer diameter of the fiber. These early stages of oxidation cause the fibers to debond from the matrix. Debonding and the bridging of cracks gradually

increases the strain as the majority of the load is transferred to the fibers. In strain region III, the oxidation of carbon fibers is much more progressed. Bridging fibers have begun to oxidize through their cross-sections. Fibers without high localized loads may oxidize completely through their cross-sections and recede away from cracks or fibers with reduced cross sections may fail. These oxidized and failed fibers cause other fibers to bear an increased load and cause cracks to open wider. The formation of pointed fiber tips and carbon recession has been observed by other researchers (Eckel *et al.*, 1995; Glime and Cawley, 1995). Figure 18 gives an example of pointed fibers receding away from a crack. Also fibers with reduced cross-sections may begin to fail as they can no longer support their load. The effects of cracks opening, continuing oxidation, fiber failure and load redistribution causes a rapid increase in strain as the material approaches ultimate failure. It should be noted that due to the high strain to failure, i.e., 1 % strain, the strain is likely to be distributed throughout the length of the fibers rather than just along portions of the fibers that bridge cracks. Since the fibers are debonded from the matrix due to the coefficient of thermal expansion differences, strain along the entire fiber length would be possible.

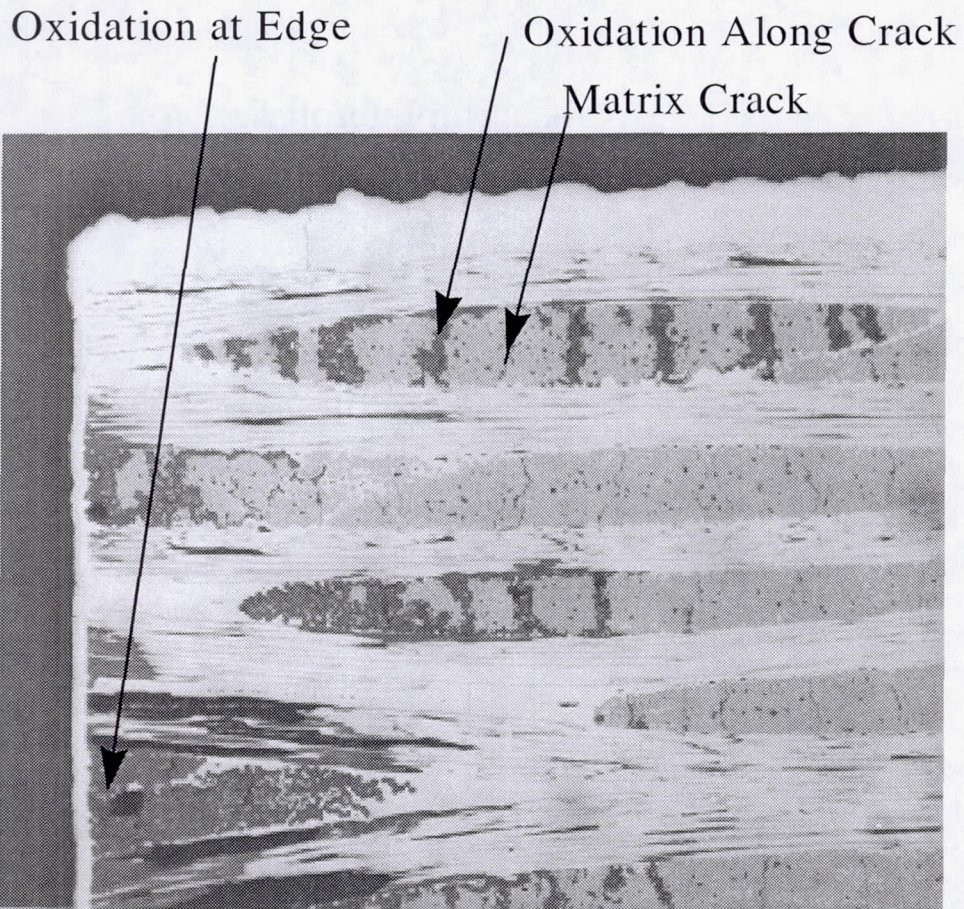


Figure 16. Polished cross-section showing oxidation of carbon fibers occurring preferentially along microcracks. 1000°C/25 ksi/air. (scale bar equals 0.1 mm)

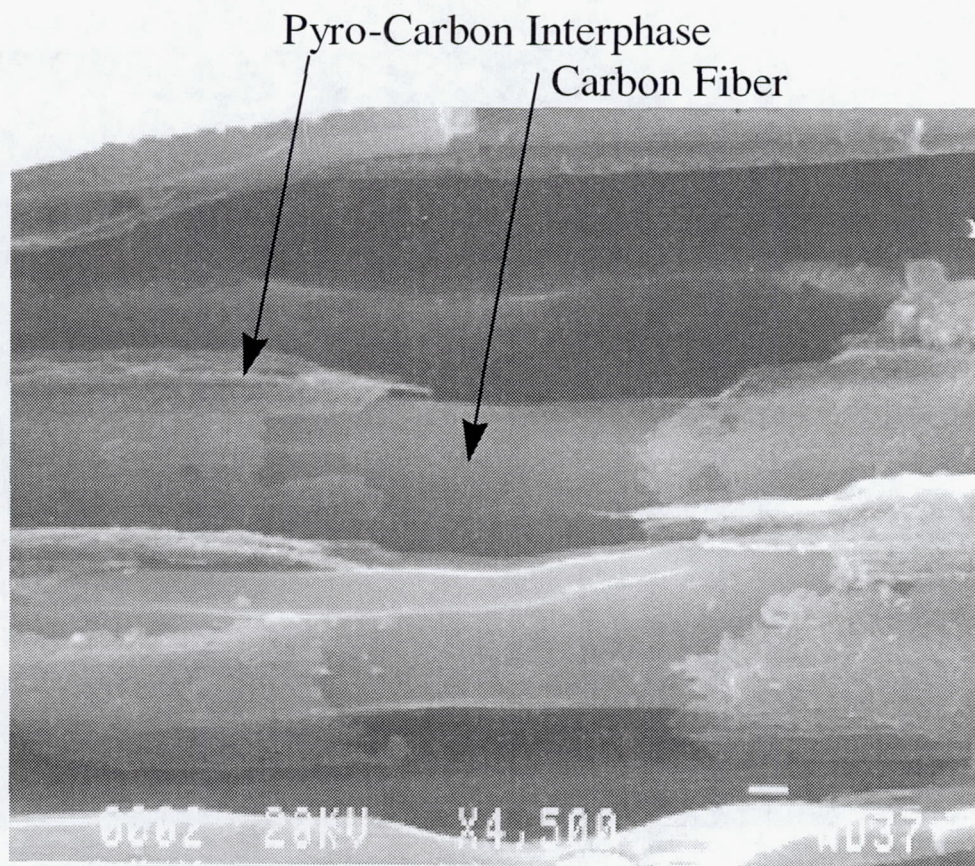


Figure 17. Fracture surface showing oxidation of the pyro-carbon interphase and narrowing of the fiber cross-section. 550°C/25 ksi/air.

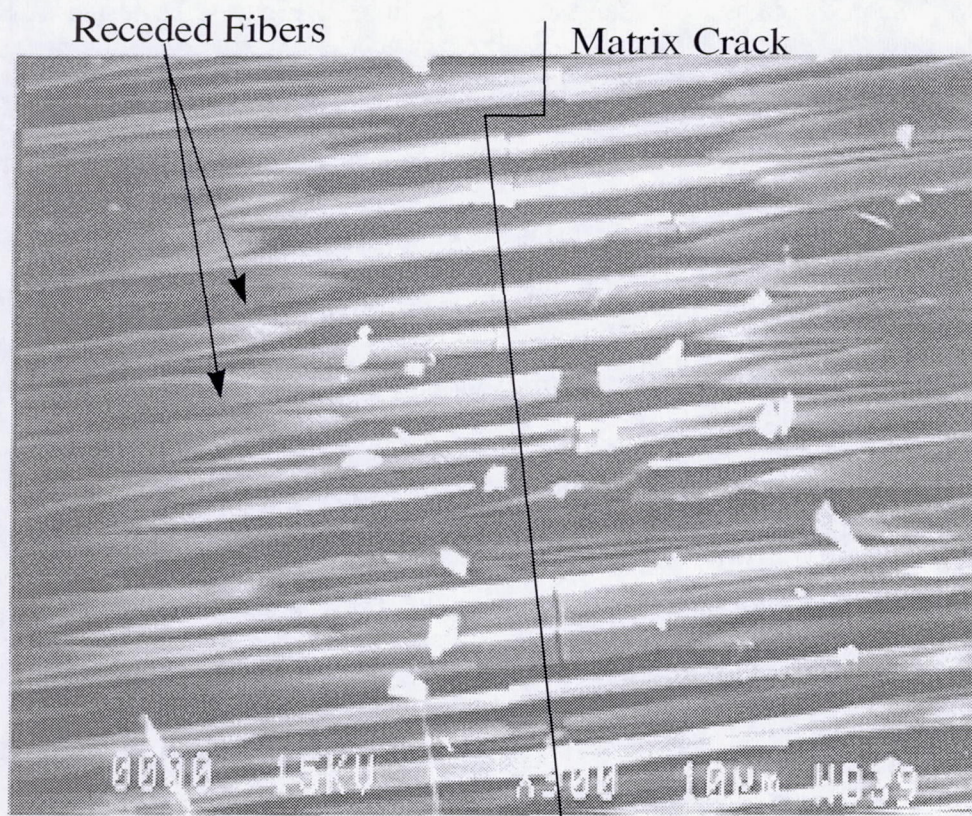
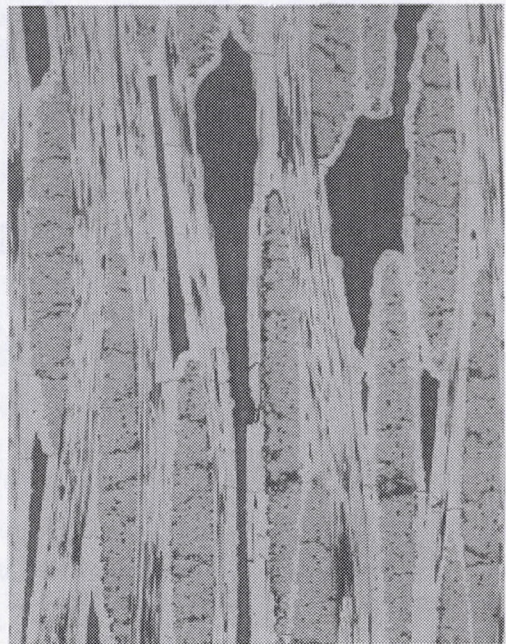
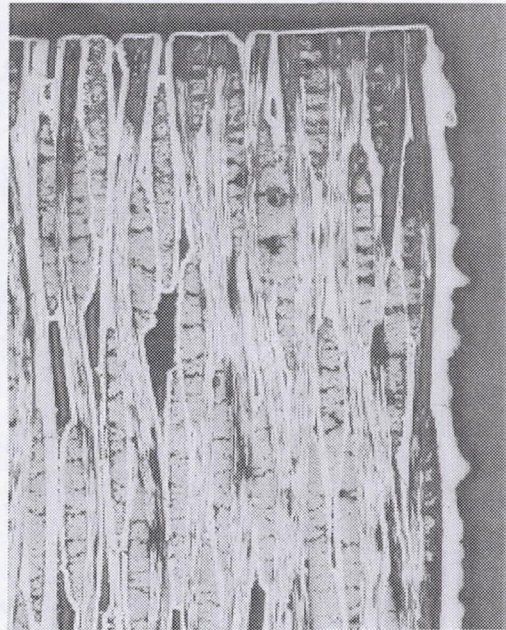
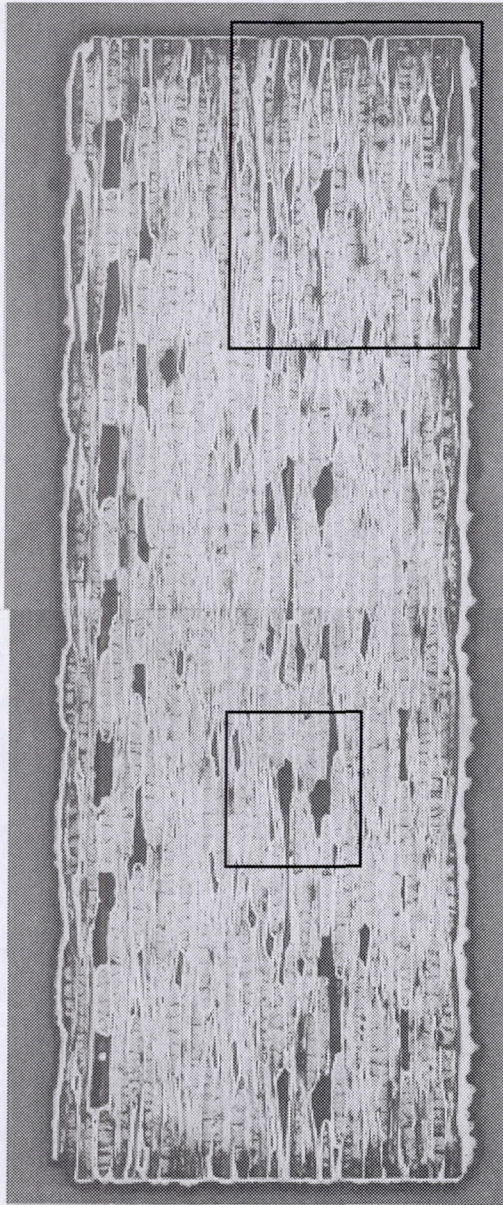
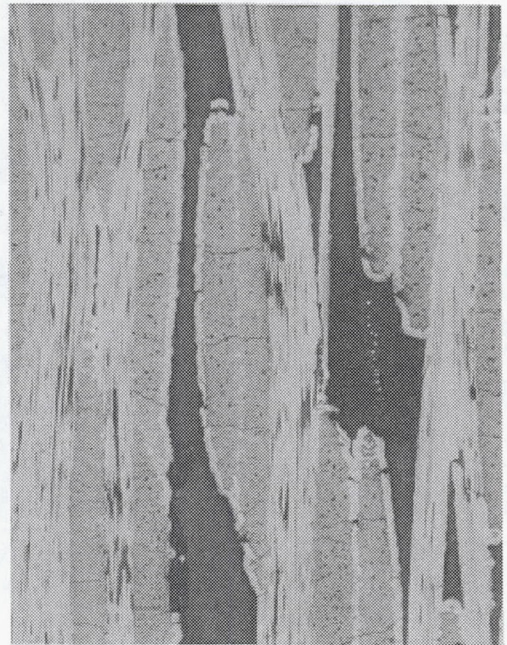
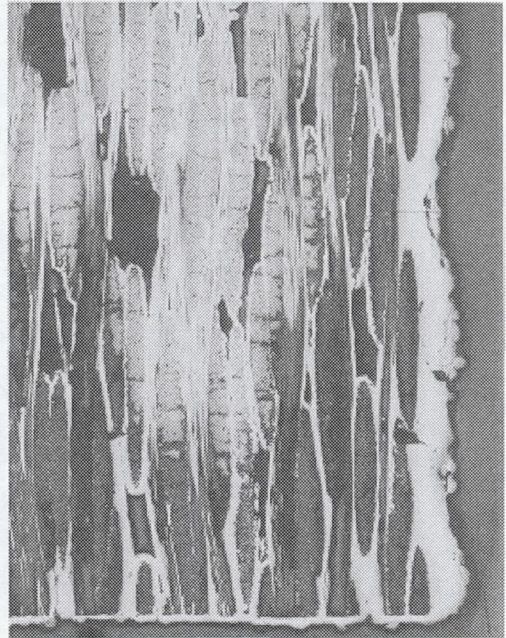
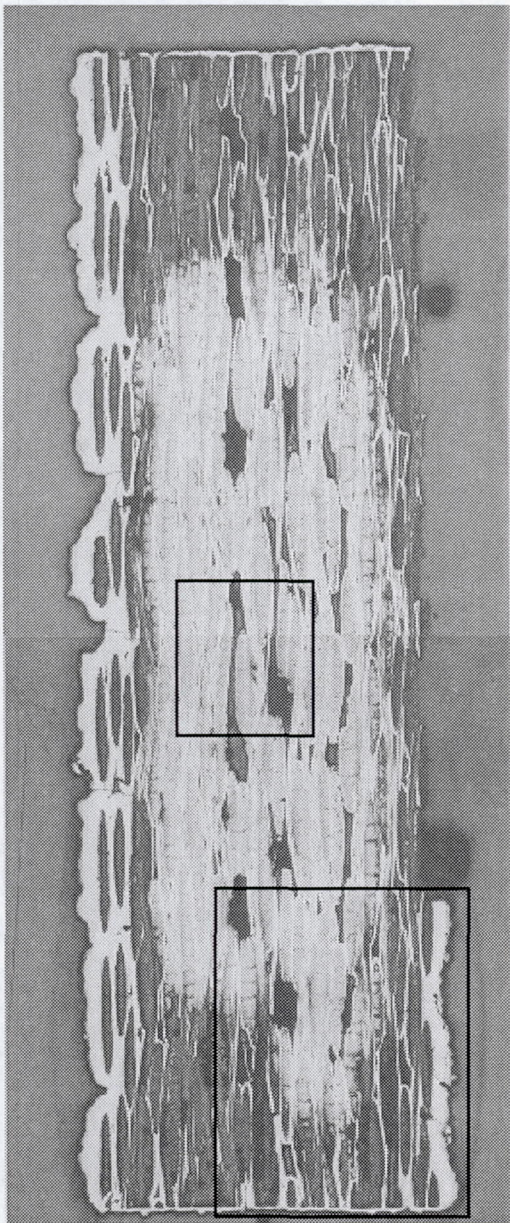


Figure 18. Fracture surface showing fibers receding to the left and right away from a matrix crack. 1000°C/25 ksi/air.

Analysis of polished cross-sections show two types of kinetics. Figure 19a shows a sample that was stressed oxidation tested at 750°C/10 ksi. Oxidation has occurred primarily along the edges but consumed fibers were also observed deep within the cross-section. The oxidation pattern suggests the reactions between carbon and oxygen were very slow. Oxygen was not consumed readily as it diffused into the matrix. The entire sample became saturated in oxygen so that evidence of the slow oxygen/carbon reactions were seen throughout the sample. The sample in Figure 20a, tested at 1400°C/10 ksi, shows much faster reactions occurred. It appears that the reactions occurred as soon as oxygen was supplied. A reaction front was observed along the outer portion of the section so that there was a shrinking core type of effect with the interior remaining virtually unaffected. Figures 20b and 20c are boxed regions from Figure 20a. Figure 20c shows an interior that is free from oxidation and Figure 20b shows the reaction front for the diffusion-controlled process. Figures 19b and 19c are boxed regions from Figure 19a. Figure 19c shows how the slow carbon/oxygen reactions occurred deep into the interior of the oxygen saturated material and Figure 19b shows generalized oxidation without a reaction front in the reaction-controlled process. It should be noted that both of these samples failed in about the same amount of time, 91 and 86 minutes respectively. It should be noted that in the views of polished cross-sections to be discussed and shown in this thesis, pores and carbon consumed areas will appear dark. Large pores or voids will be located between fiber tows. Small pores will be located within individual fiber tows.



Figures 19a-c. Cross-sections of a sample tested at 750°C/69 MPa. Figure 19a (left) is an overall view. Figures 19b (upper right) and 19c (lower right) are close-up views of an edge and the interior respectively.



Figures 20a-c. Cross-sections of a sample tested at 1400°C/69 MPa. Figure 19a (left) is an overall view. Figures 19b (upper right) and 19c (lower right) are close-up views of an edge and the interior respectively.

### 2.3.6 Stressed Oxidation of Four Different C/SiC Materials

Stressed oxidation of the four different materials at 1454°C and the two stresses of 69 MPa and 172 MPa showed the effectiveness of oxidation inhibitors. Materials A and B (DLC standard C/SiC and BFG C/SiC, respectively) did not have any enhancements or oxidation protection systems. Material B was reported by the manufacturer to have some form of proprietary oxidation inhibitor. The inhibitor was believed to be at the interphase level. However for the purpose of this discussion, material B will be classified as a material without an effective oxidation inhibitor located either in the matrix or the external seal coating. Due to materials A and B not having oxidation inhibitors, they were susceptible to oxidation. Microstructural analysis of polished cross-sections showed oxidized fibers in samples tested at both stresses. Figures 21a-c and 22a-c show optical views of polished cross-sections of samples tested at 69 MPa for material A and material B respectively. Views 21a and 22a are of the overall cross-sections. Views 21b-c and 22b-c are close up views of the reaction front. As expected at this high temperature of 1454°C, a shrinking core and moving reaction front were seen due to the kinetics being in the diffusion-controlled regime. At the higher stress of 172 MPa, similar oxidation patterns were observed, however the overall amount of oxidation was less due to the shorter lives and therefore shorter times of exposure. Fracture surfaces taken from a SEM are shown in Figures 23 and 24 for material A. In these figures, oxidation of the pyrolytic-carbon interphase, narrowing of the fibers and failure of the fibers are seen as the portions of the fibers that bridge matrix cracks have begun oxidize. This significant oxidation in materials A and B led to their short lives.

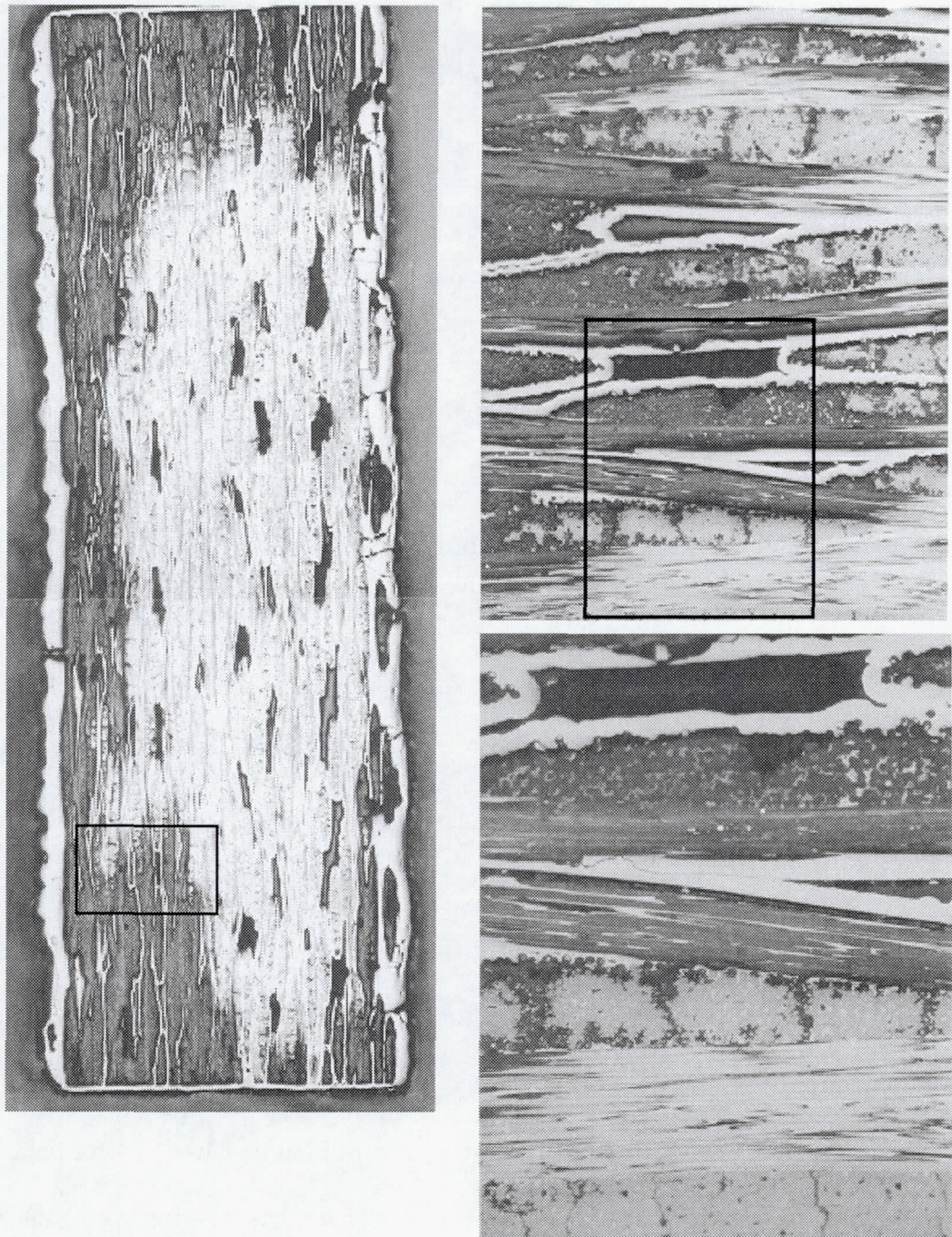
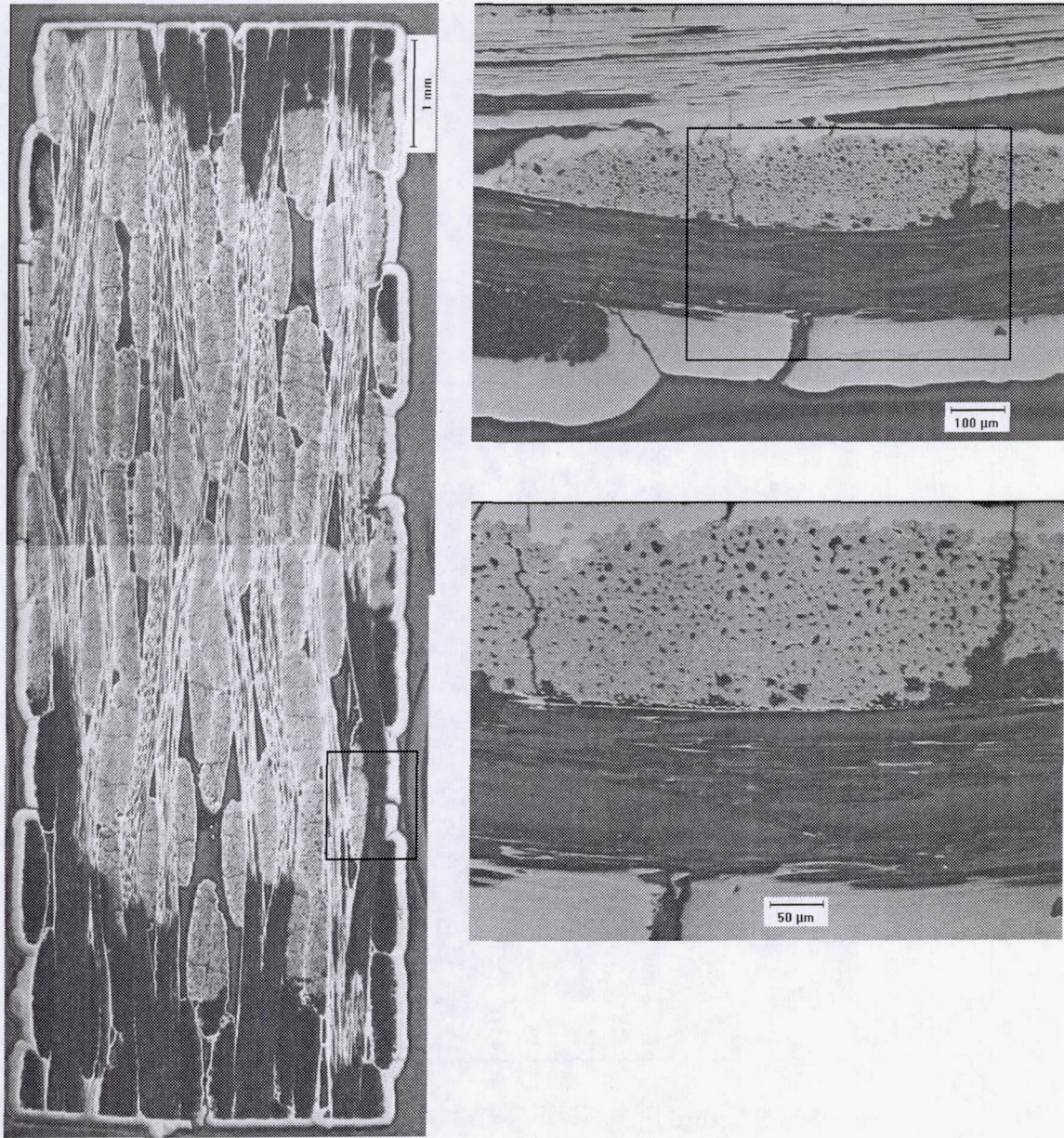


Figure 21a-c. Material A: DuPont-Lanxide standard C/SiC. Micrographs of a polished cross-section of a sample stressed oxidation tested at 1454°C/69 MPa. Figure 21a (left) is an overall view of the cross-section. Figure 21b (upper right) is a view of the reaction front. Figure 21c (lower right) is a close-up of the reaction front.



Figures 22a-c. Material B: BFG C/SiC. Micrographs of a polished cross-section of a sample stressed oxidation tested at 1454°C/69 MPa. Figure 22a (left) is an overall view of the cross-section. A (left) is an overall view of the sample. Figures 22b (upper right) and 22c (lower right) show oxidation at the edge near a crack and the reaction front.

Regions of oxidation along matrix cracks (portions of the matrix and cracks remained after failure).

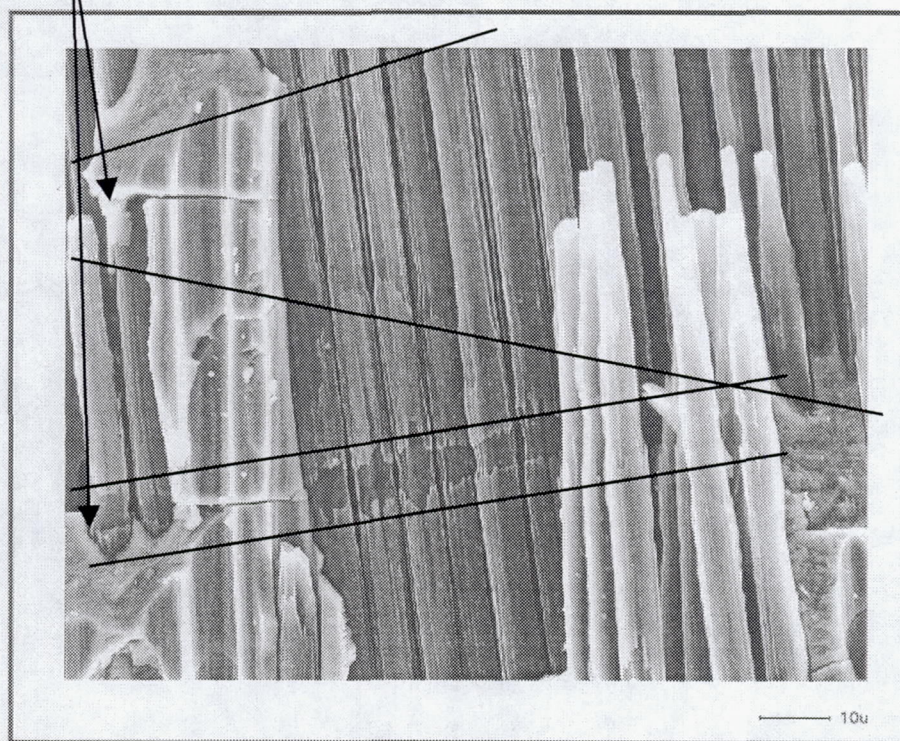


Figure 23. Fracture surface of a sample that was stressed oxidation tested at 1454°C/69 MPa.

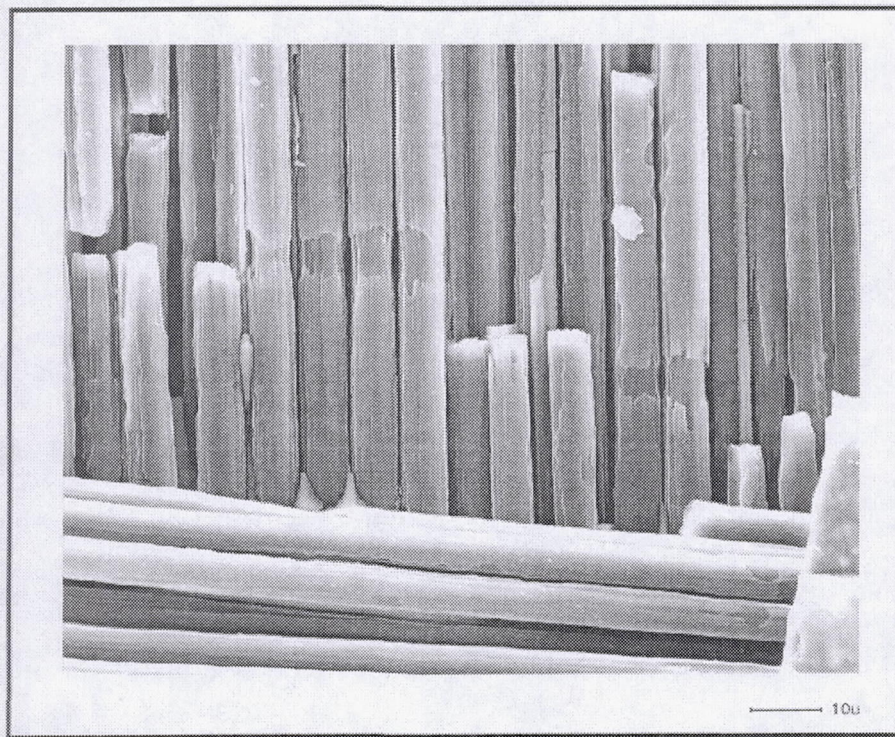
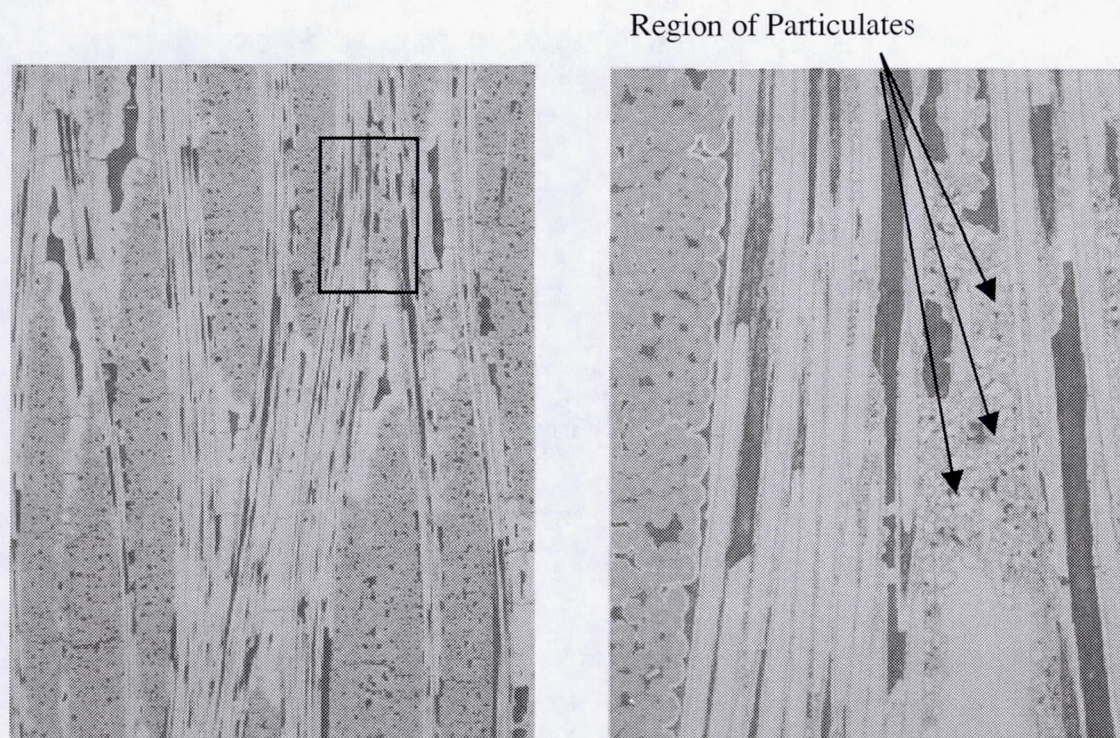


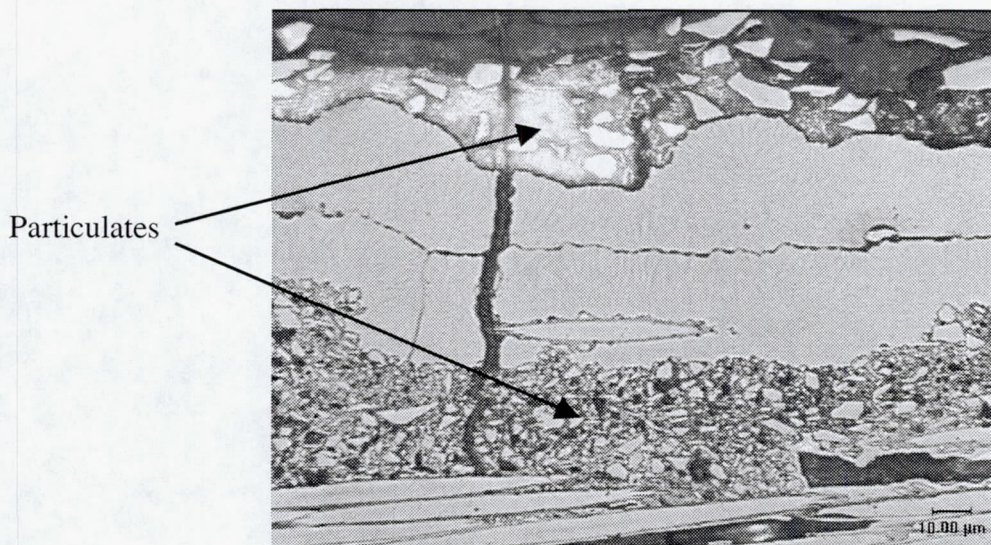
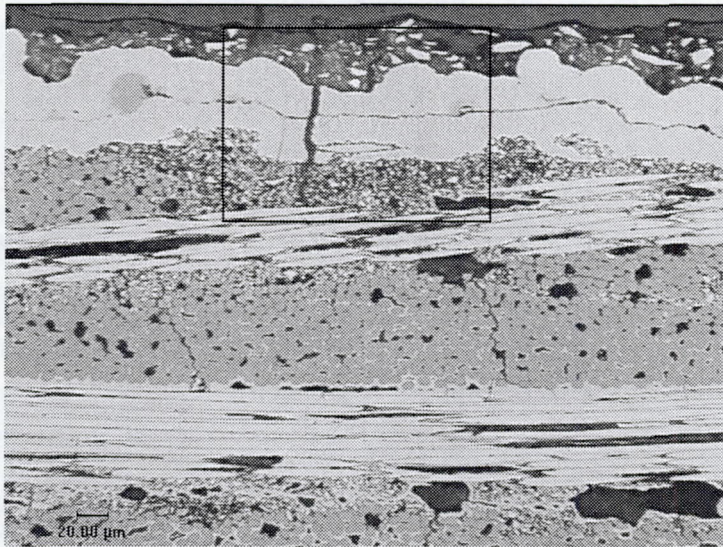
Figure 24. Fracture surface of a sample that was stressed oxidation tested at 1454°C/69 MPa.

As suggested by the time to failure data, material C (DLC enhanced C/SiC) and material D (DLC enhanced C/SiC with a CBS external seal coating) had effective oxidation inhibitors. The boron containing particulates and external seal coating may have formed borosilicate glasses that helped seal cracks and diminish the supply of oxygen to the interior. In Figure 25a-b, the boron containing particulate in the interior of material C can be seen. Interior and edge views of materials D are shown in Figure 26a-b. Both oxidation inhibitors, boron containing particulate within the interior and an external coating consisting of carbon/boron/silicon, can be seen in Figure 26a-b. Microstructural analysis confirmed that there was little oxidation in these materials. Figure 27a-d shows views of a polished cross-section of material C that was tested at 69 MPa and 1454°C. In of the overall view for material C, there was not evidence of gross oxidation (of the type observed for materials A and B which had shrinking cores and moving reaction fronts). However, closer optical analysis, see Figure 27b-d, revealed minimal oxidation of interphases of fibers located close to cracks in samples tested at the lower stress of 69 MPa. For the samples tested at the higher stress of 172 MPa, optical analysis of polished cross-sections did not show oxidation of even the interphase. This could be due to the much shorter lives and therefore the shorter times of exposure for oxidation to occur, resulting in such limited oxidation that it was not detectable by the optical microscope. Analysis of fracture surfaces using a SEM, does show oxidation damage to fibers at this higher stress which could not be determined from optical analysis. In Figure 28, less fiber pullout at the edge was observed than for the fibers in the interior. The brittle failure at the edge could be due to the oxidation of flaws in the interphase and fibers. Further into the interior where the interphase was still intact,

composite failure occurred in which there was more fiber pull-out. Figure 29 shows detail of oxidized fibers which have assumed a pointed shape as they oxidized. These fibers are no longer continuous or crack bridging. These fibers may have failed due to high local stresses acting on the oxidized and reduced cross-sections. Another possibility is that the fibers did not have high local stresses and just oxidized completely through their cross-sections. Once the fibers were discontinuous the fiber ends continued to oxidize and recede from one another and from the crack. It should be noted again that material C survived 25 hours at 69 MPa and had high residual strengths, however at 172 MPa the times to failure were much like those for the materials without oxidation inhibitors.



Figures 25 a-b. Polished cross-section of the interior of material C (DLC enhanced C/SiC) which shows boron containing particulates.



Figures 26 a-b. Polished cross-section of the interior of material d (DLC enhanced C/SiC with CBS coating) which shows boron containing particulates. In both views, oxidation inhibitors can be seen in the interior and on the exterior of the material.

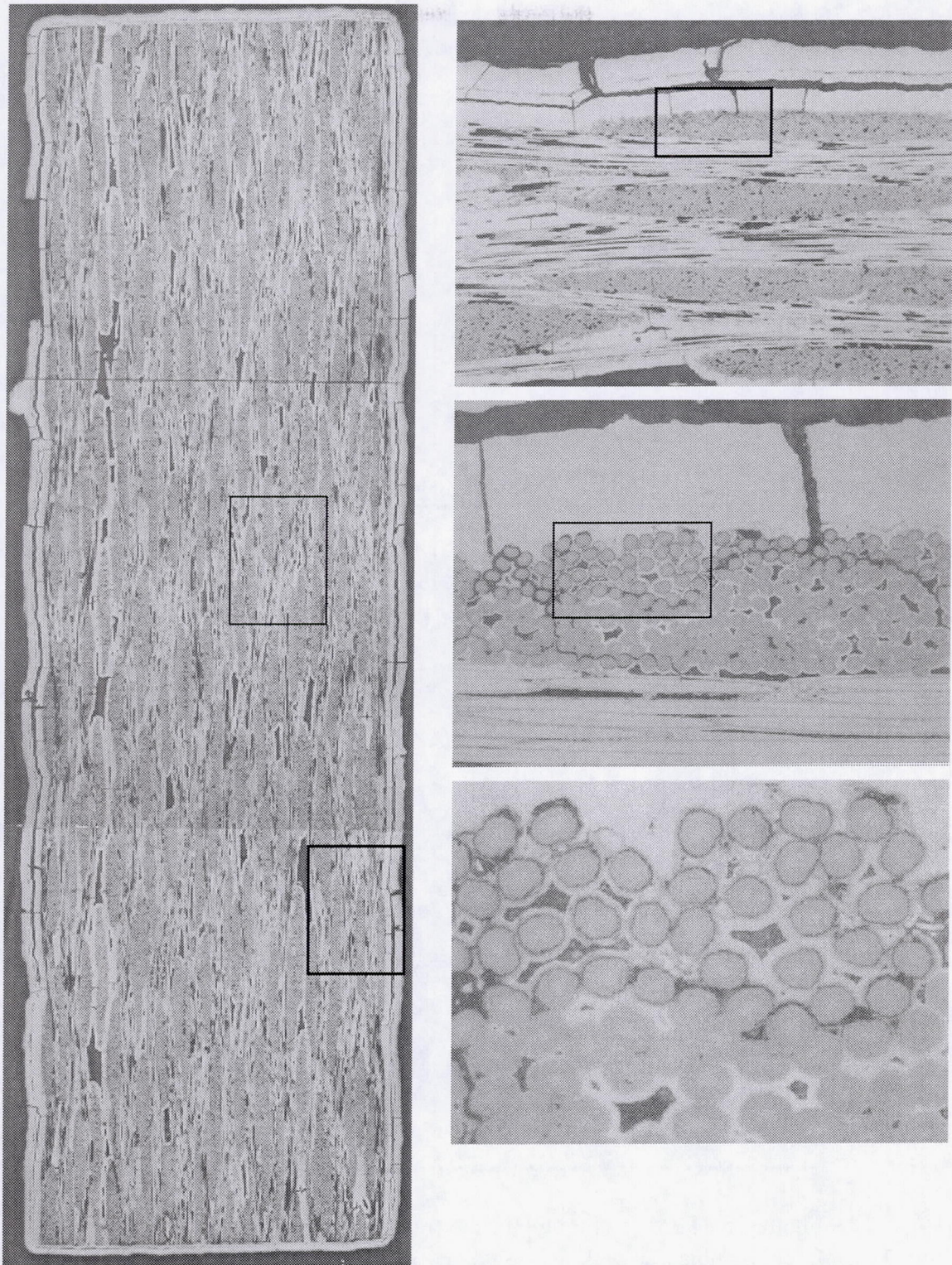


Fig. 27 a-d. Material C: DuPont-Lanxide enhanced C/SiC. Micrographs of a polished cross-section of a sample stressed oxidation tested at 1454°C/69 MPa. Figure 27a (left) is an overall view of the cross-section. Figure 27b (upper right) is a view near the edge. Figures 27c (middle right) and 27d (lower right) are close-up views near an edge where oxidation of the interphase occurred near a crack.

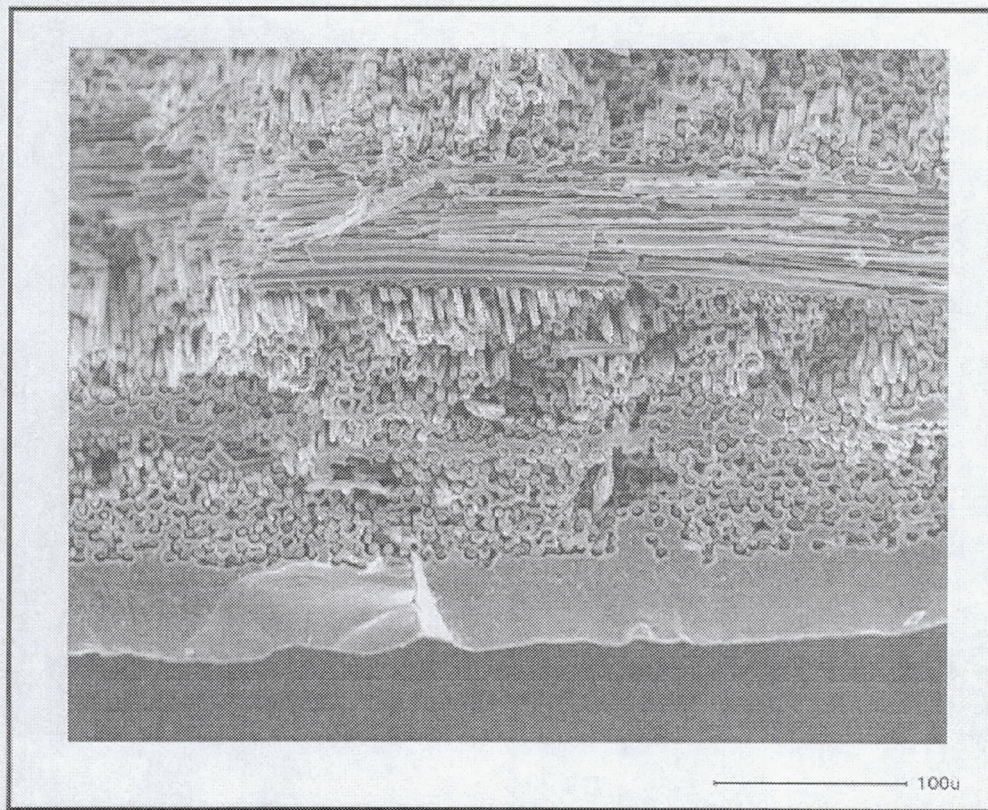


Figure 28. SEM micrograph of the fracture surface of a DLC enhanced C/SiC sample that was stressed oxidation tested at 1454°C/172 MPa.

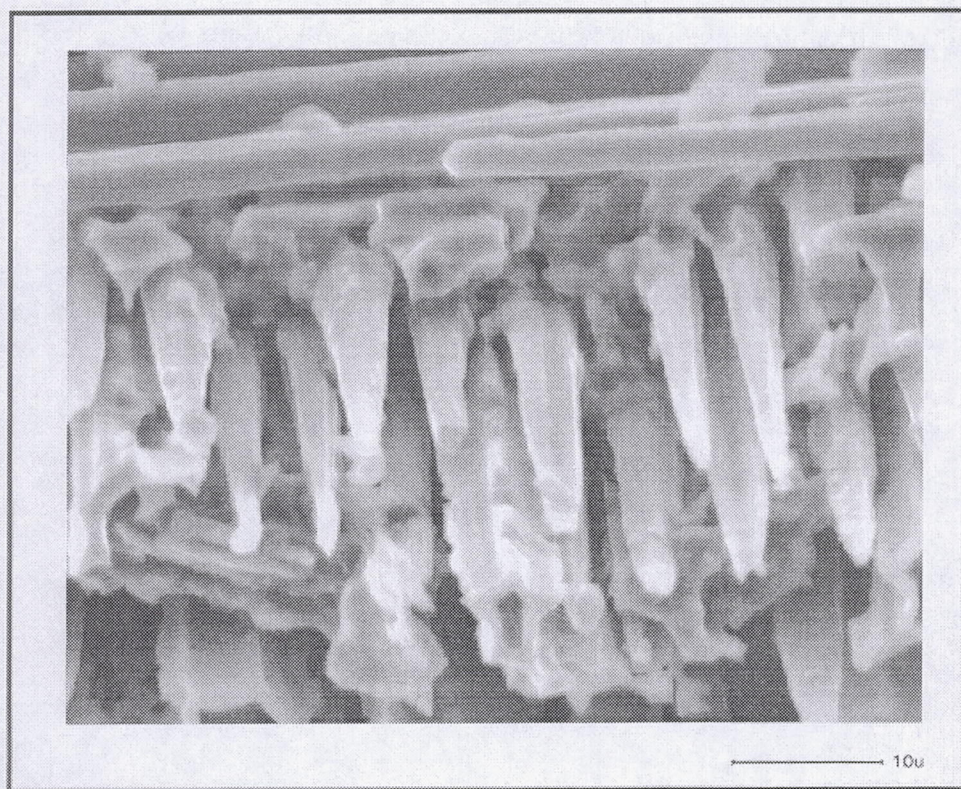


Figure 29. SEM micrograph of the fracture surface of a DLC enhanced C/SiC sample that was stressed oxidation tested at 1454°C/172 MPa.

These short lives at the higher stress are attributed to oxidation susceptibility at intermediate temperatures as suggested by the failure locations. At the stress of 69 MPa, materials A, B, and D (D fractured at room temperature during residual strength tensile tests) failed in the gage section while material C failed in thermal gradient region. At the stress of 172 MPa, materials A, and B failed in the gage while materials C and D failed in the thermal gradient region. The thermal gradient region was beyond the neck of the sample and was located more near the grip end. The thermal gradient arose due to heating the gage section with a SiC susceptor and cooling the end with water cooled grips. Examples of typical failures are shown in Figure 30a-b.

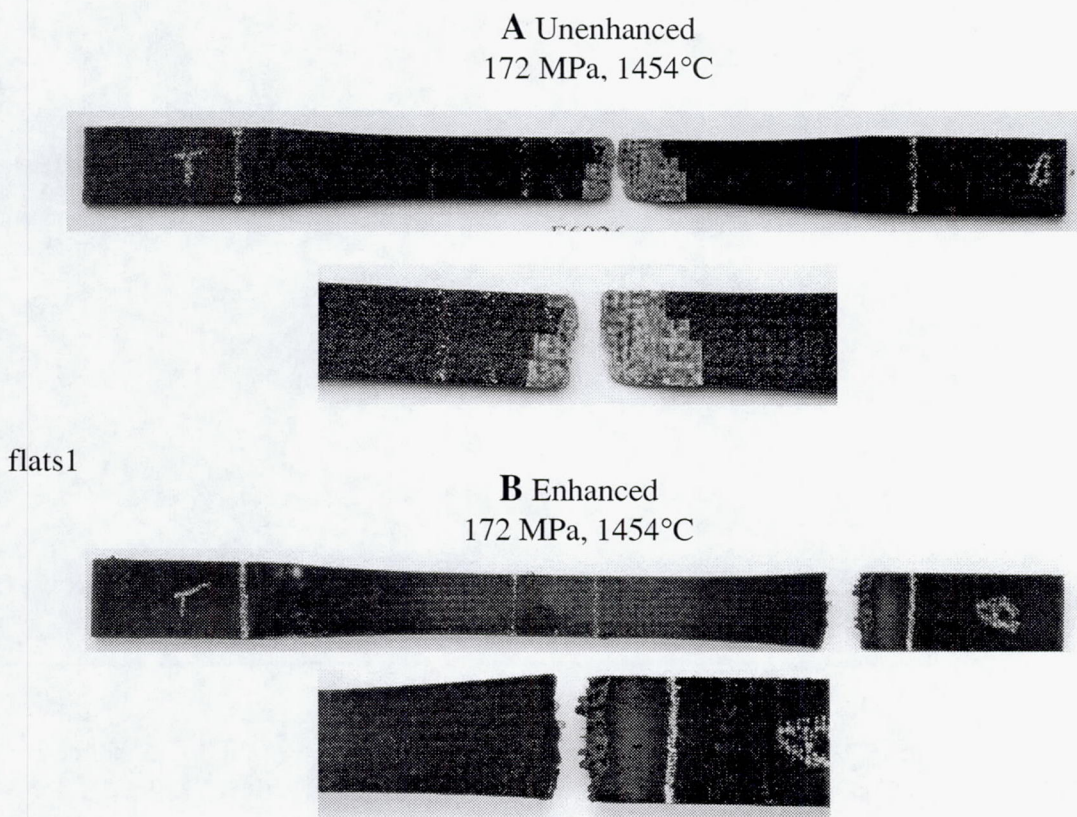


Figure 30a-b. Test coupon failure locations. View a (top) is an example of failure in gage section as was typically seen in the two unenhanced material. View b (bottom) is an example of failure in the thermal gradient region as was typically seen in the two enhanced materials.

The other material with oxidation inhibitors, materials D, did not show significant oxidation in the microstructural analysis of a polished cross-section. An overall view and additional views of a sample tested at 69 MPa are shown in Figure 31a-c. Only one small region of oxidation could be found in which the interphases of fibers near a crack had oxidized as seen in Figure 31c. In the overall view, Figure 31a, the region in the middle right of the section would at first appear to be a region of material degradation due to oxidation. However this is actually a region where complete infiltration of the matrix did not occur. Better detail of the incomplete infiltration can be seen in Figure 32a-b. This could be due to the boron containing particulate material which surrounds the fiber tows. As seen in Figure 32b, the poorly infiltrated fiber tow is completely surrounded by boron particulate which may have inhibited the chemical vapor infiltration of the silicon carbide matrix during processing. At the higher stress, very little oxidation was observed in the analyzed cross-section. Minimal oxidation in the heated gage section and failures in the thermal gradient region would suggest a susceptibility to oxidation at intermediate temperatures. A section of material that spans the high and low part of the thermal gradient region along the tensile bar was taken from a sample tested at 172 MPa. Low in the thermal gradient region, much more oxidation was observed than for the section that was taken from the hot-zone. Figure 33a and the close up view in Figure 33b, show that oxidation of the interphase and fiber near cracks and along the edge of the sample lead to fibers with reduced cross-sections.

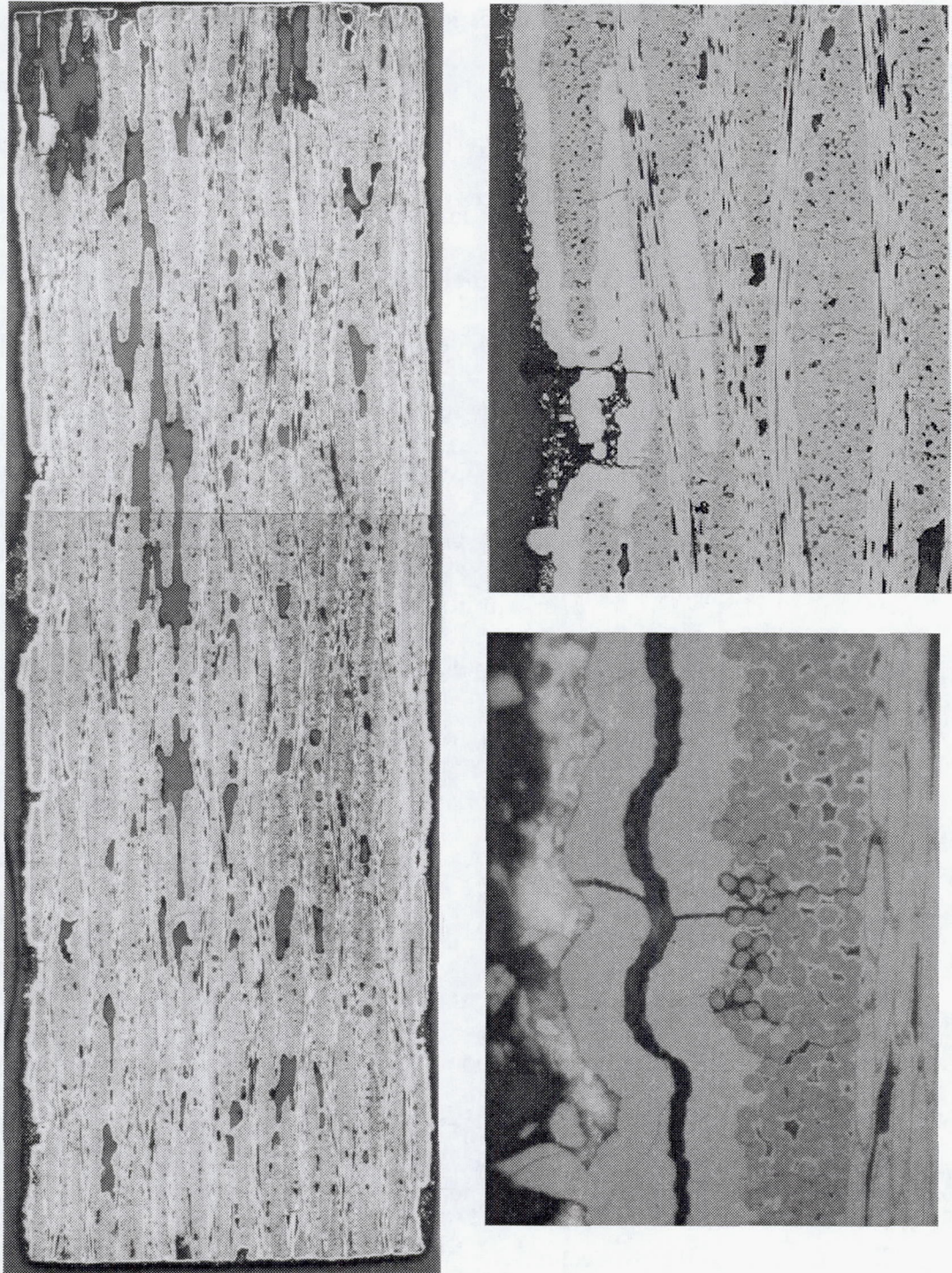


Figure 31a-c. Material D: DuPont-Lanxide enhanced C/SiC with CBS. Micrographs of a polished cross-section of a sample stressed oxidation tested at 1454°C/69 MPa. Figure 31a (left) is an overall view of the cross-section. Figure 31b (upper right) is a view near the edge. Figure 31c (lower right) is a close-up view near an edge where oxidation of the interphase occurred near a crack.

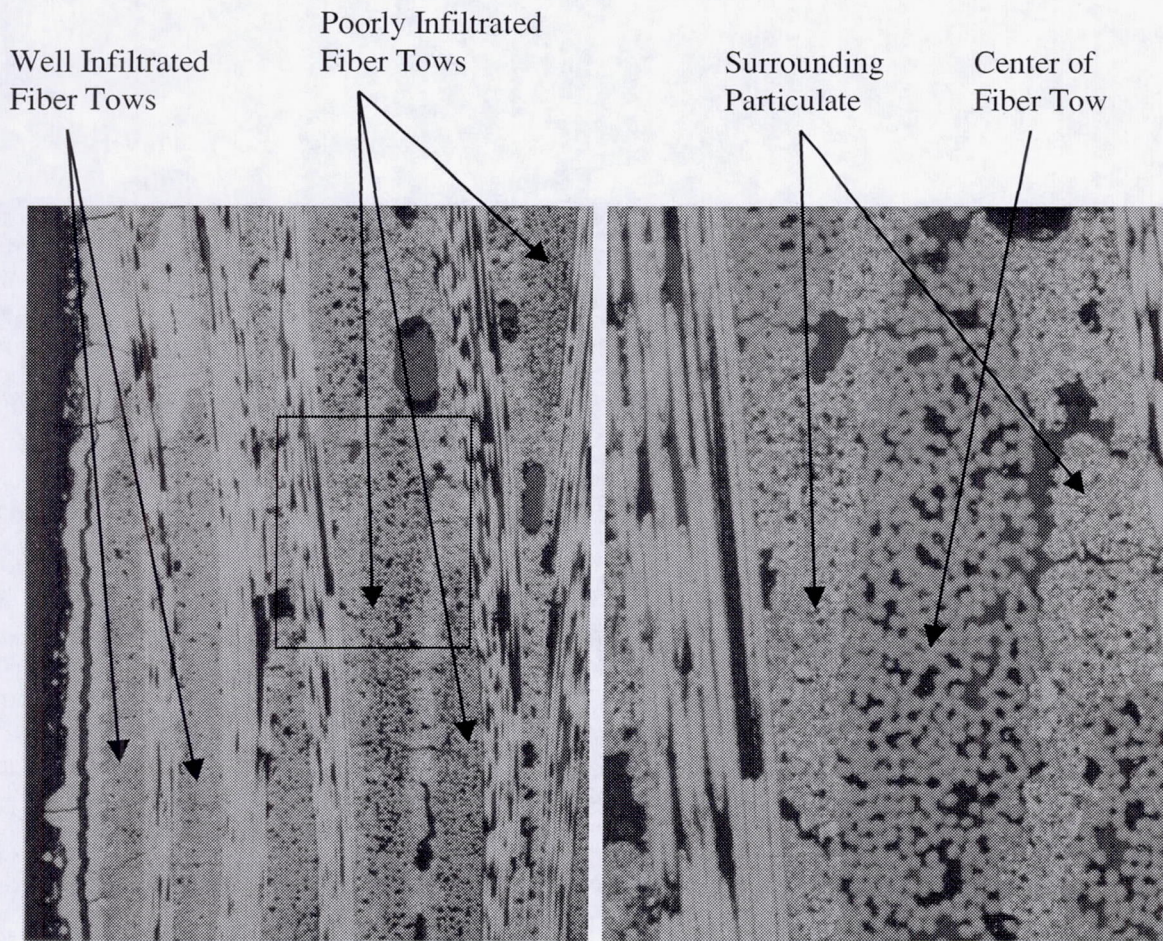


Figure 32a-b. Incomplete chemical vapor infiltration of silicon carbide into fiber tows. Figure 32a (left) shows well infiltrated carbon fiber tows to the left and poorly infiltrated tows to the right. Figure 32b (right) shows detail of a poorly infiltrated

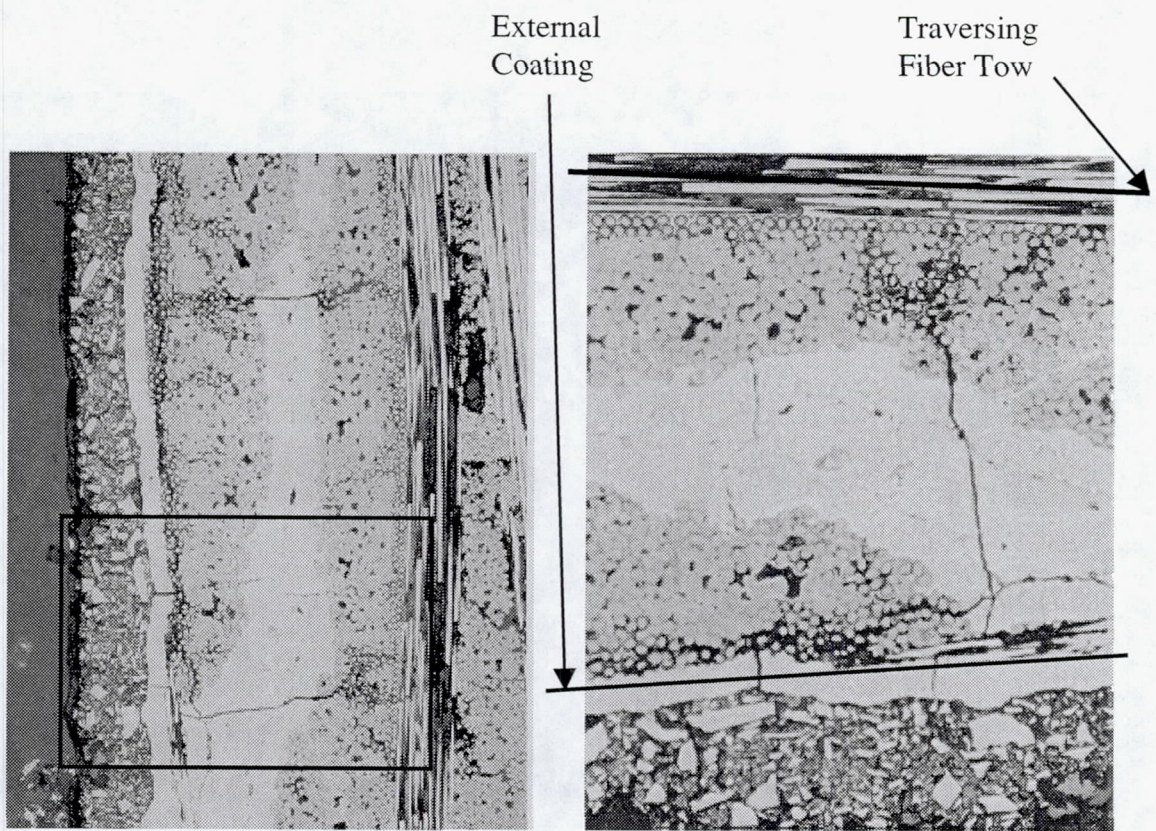


Figure 33a-b. Oxidation in a cross-section taken from the thermal gradient region. Figure 32a (left) shows oxidation of fibers along cracks, along the inside of external coating and along a traversing fiber tow. Figure 32b (right) is a close-up view.

## 2.4 Experimental Summary

The susceptibility of carbon fiber to oxidation in a flowing oxygen environment was investigated by TGA of bare carbon fiber and of C/SiC test coupons. The bare carbon fiber was very susceptible to oxidation at all temperatures, 500°C-1400°C. A reaction-controlled regime was observed at temperatures from 500°C-600°C and had an activation energy of 64.1 kJ/mol. At higher temperatures, 600°C-1400°C, a diffusion-controlled regime was observed and had an apparent activation energy of 7.6 kJ/mol which was not a real activation energy due to applying linear data to a parabolic regime where the temperature relation is really  $T^{3/2}$ . However the apparent activation energy does signify that a transition in kinetics did occur. In the results of TGA test of C/SiC coupons, it was seen that the two distinct regimes do not occur. This was due to the material's susceptibility to oxidation at low temperatures and the self-protecting effect at higher temperatures. At low temperatures, i.e., 550°C-900°C, the as-fabricated cracks allow for ingress of oxygen, which reacts with the carbon fiber. However, at high temperatures, i.e., 950°C-1400°C, crack closure due to fiber and matrix expansion and the formation of silica scales greatly diminished or eliminated the supply of oxygen to the interior.

When a stress was applied, as for the stressed oxidation tests, the cracks were open wide enough that the self-protecting effects were not observed. When the C/SiC material was under stress, two regimes were observed. The times to failure would suggest regime 1 occurred at temperatures of 350°C-750°C and regime 2 occurred from 750°C-1500°C. The reason why the transition temperature in the TGA tests occurred at a lower temperature is due to the high velocity gasses effectively increasing the Sherwood

number at a given temperature as compared to in the stressed oxidation tests which occurred in a stagnant gas. The creep tests of C/SiC in an inert environment helped confirm, at least at low temperatures (750°C), that the inelastic strains observed in stressed oxidation were due to oxidation damage effects to the material.

Oxidation inhibitors were effective in prolonging life and retaining strength even when the materials were under stress in a high temperature, oxidizing environment, i.e., 10 and 25 ksi and 1454°C. The two inhibiting methods, boron containing particulate in the matrix and CBS external seal coating, were effective as they reacted to form borosilicate glasses that sealed cracks. Even at 25 ksi, the material with both boron containing particulate and a CBS external seal coating, protected the material and gave much longer lives. Both enhanced materials did show susceptibility at intermediate temperatures. These were intermediate temperatures along the thermal gradient of the material where the temperature is too low for borosilicate glasses to form.

### 3. MODELING

#### 3.1 Model Development

Finite difference and relaxation methods can be used to estimate solutions to the mathematically complex equations that are involved in heat and mass transport (Gaskell, 1992; Geankoplis, 1978). For this analysis, an existing finite difference model was extended in order to gain a better understanding of the diffusion and reaction-controlled kinetic regimes observed in the experiments. The finite difference method used is an adaptation of the finite difference method developed by Glime and Cawley to study the profiles of carbon fibers as they oxidize (Glime and Cawley, 1995). In the current use of this method, the diffusion of oxygen into a cross-section of a matrix that is bridged by an array of carbon fiber tows was studied. The oxygen concentrations at steady-state gave indications about the oxidation kinetics. The next step that will be discussed is the removal of carbon as the carbon fiber tow cross-sections were oxidized. In reacting away surfaces of a circle of carbon that are represented by square cells that give a rough surface, a geometry correction had to be included. This correction, which was not considered in Glime's initial development of the model, will be discussed. Reacted cross-sections which correlate to diffusion-controlled and reaction-controlled were compared to experimental observations. Finally, the model was studied for different geometries and was compared to analytical solutions. A study on the effect of randomly flawed carbon regions is presented in the an Appendix.

##### 3.1.1 Oxygen Concentration at Steady-State

The model considered the case of an array of carbon fibers that bridge a matrix crack, as was illustrated in Figure 3 in the introduction. This representation was chosen

based on the experimental observations discussed in the introduction and shown in Figures 1 and 2. A cross-section of a 2-D plane in the open region being bridged by the carbon fiber tows was analyzed using the finite difference model.

A 3-D illustration of a 12x12 array of crack bridging fiber tows is illustrated in Figure 34. An additional assumption was that the crack opening was sufficiently narrow so that there was no oxygen gradient in the direction parallel to the fiber axis, therefore a 2-D plane from within the open crack bridging region was considered. The 2-D plane was laid out as a cell pattern consisting of a 250 x 250 mesh of square cells with a 12 x 12 array of carbon fiber tows. An illustration of the cross-section is shown in Figure 35a-b. Detail of one quarter of the cell pattern (125 x 125 cells) is shown in Figure 35b. Cells within the mesh pattern were designated as either external boundary cells, open space cells in the interior which contain the diffusing gases, or as carbon containing cells. Carbon fiber tows had a diameter of 10 cells. Fiber tows were spaced a distance of 10 cells from one another and 10 cells from the outer edge. The midlines through the full cell pattern are shown in Figure 35a. Oxygen concentrations calculated from the model will be presented later in this thesis as either one-quarter sections or 1-D plots of the concentration along the midline.

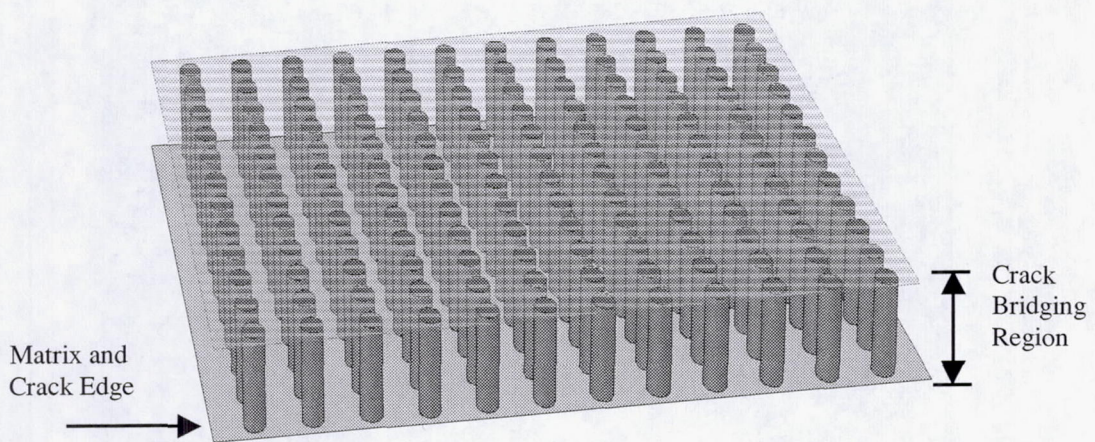


Figure 34. Illustration of a 12x12 array of crack bridging fiber tows.

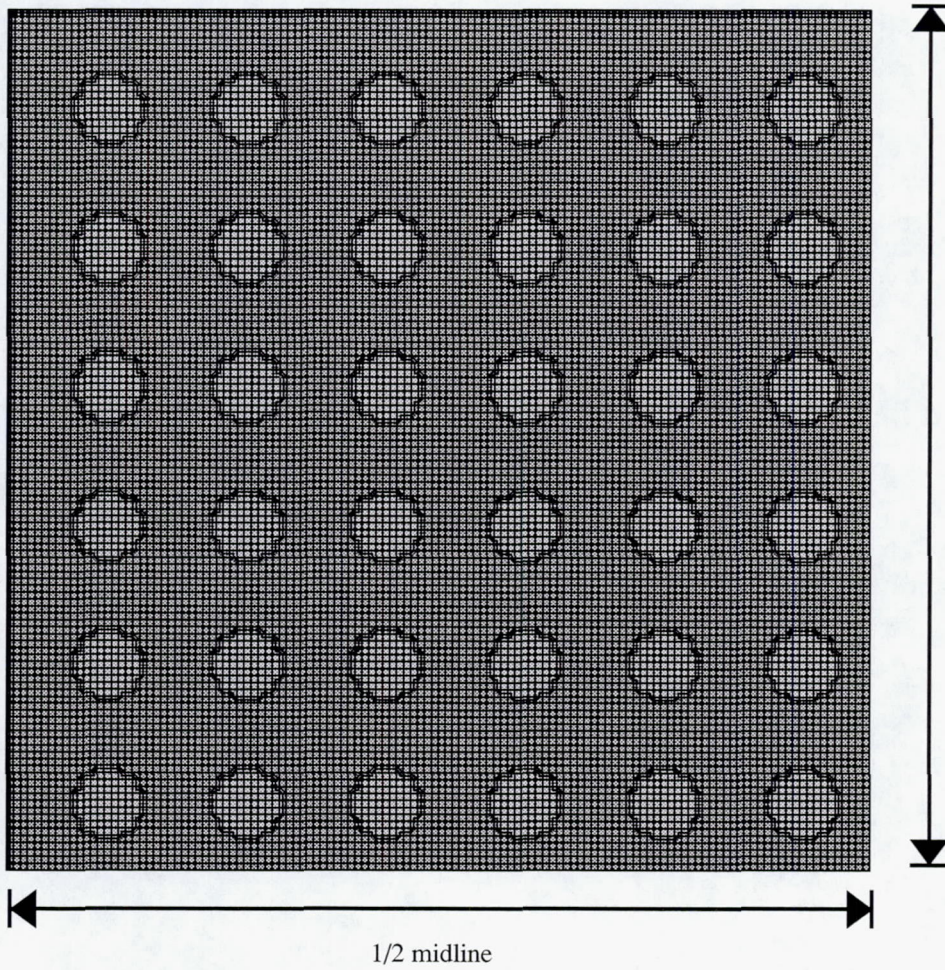
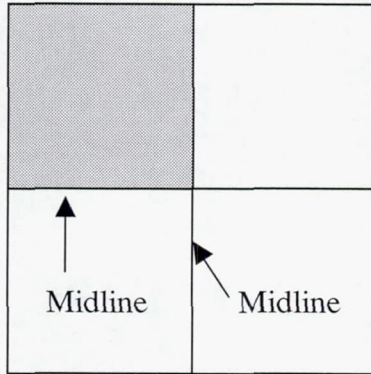


Figure 35a-b. One-quarter plot of the matrix pattern (b, below) orientated as shown in the sectioned square (a, above).

In the model, the outer boundary had an initial oxygen concentration arbitrarily set at 1.0. Therefore the steady-state oxygen concentration of cells in the interior was a fraction of the ambient concentration. Oxygen concentrations were calculated throughout the matrix based on mass transfer flux equations in which both the reaction rate constant and diffusion coefficient are dependent on temperature. Due to the differing temperature dependencies, the rate of carbon/oxygen reactions or the rate of oxygen supply had the potential to limit the overall oxidation process.

In the introduction, the concept of the Sherwood number was introduced as the dimensionless concentration gradient at the surface. The Sherwood number can also be thought of as the ratio between the flux contributions of diffusion and mass convection (reaction at the interface of solid phase and a gas phase) to mass transport through a concentration boundary layer (Gaskell, 1992). When mass transport occurs by diffusion, the flux,  $F_D$  (mol/m<sup>2</sup> s), is given by,

$$F_D = D_{A,B} \frac{(C_{A,S} - C_{A,\infty})}{L} \quad (15)$$

where  $C_{A,S}$  is the oxygen concentration at the solid surface (mol/m<sup>3</sup>),  $C_{A,\infty}$  is the oxygen concentration in the bulk gas (mol/m<sup>3</sup>),  $D_{AB}$  is the binary diffusion coefficient for oxygen and the oxide (m<sup>2</sup>/s), and  $L$  is the thickness of the stagnant gas film (m).

When mass transport occurs by mass convection at the solid and gas phase interface, the flux,  $F_C$  (mol/m<sup>2</sup> s), is given by,

$$F_C = h (C_{A,S} - C_{A,\infty}) \quad (16)$$

where  $h$  is the local mass transfer coefficient or the reaction rate constant (m/s). It is inevitably recognized that the form of Eqn. (16) is exactly that associated with the

assumption of first order reaction kinetics and, therefore, one special case of the mass transfer coefficient is the reaction rate constant, i.e.,  $h=K$ . When the ratio of the fluxes is taken, the Sherwood number can be obtained such that

$$\text{Sh} = \frac{F_C}{F_D} = \frac{KL}{D_{AB}} \quad (17)$$

The local Sherwood number, which occurs in the simulations is defined as

$$\text{Sh}_x = \frac{K\Delta x}{D_{AB}} \quad (18)$$

where  $\Delta x$  is a characteristic distance (in units of cells or grid spacing). The local Sherwood number was used extensively throughout the model. The value of the local Sherwood number correlates with either the diffusion-controlled kinetics regime or the reaction-controlled kinetics regime. The limiting kinetics occurs in different regimes due to temperature dependencies. As discussed in the introduction, the reaction rate constant can change by several orders of magnitude whereas the diffusion coefficient can change only by a factor of three across the temperature range of 500-1500°C. Low values of the reaction rate constant give low local Sherwood numbers and limit the kinetics, i.e., reaction-controlled kinetics. At high temperatures, the reaction rate constant is significantly larger while the diffusion coefficient is only modestly larger. Therefore at high temperatures, high local Sherwood numbers are obtained but the kinetics are limited by the less contributing factor (i.e., the diffusion coefficient). In this case the kinetics are diffusion-controlled kinetics.

Detail of the cell pattern showing half of a carbon fiber tow and surrounding open pore space is illustrated in Figure 36. The oxygen concentration of each cell was determined by relaxation using the values of its four neighbors. In these calculations, the fluxes between the central cell and its four neighboring cells were evaluated, and the value at each site was sequentially replaced until steady-state was closely approximated, i.e., the net flux into and out of the each cell was zero. A standard explicit finite difference was used to iteratively replace the values of each site. For a site completely surrounded by sites containing only the diffusing gases, i.e., cell 1 in Figure 36, the oxygen concentration is

$$C(i, j) = \frac{[C(i, j-1) + C(i-1, j) + C(i, j+1) + C(i+1, j)]}{4} \quad (19)$$

When one of the neighboring cells contains carbon, as for cell 2 in Figure 36, mass transport occurs by chemical reaction, which is a similar process as for convection in heat transport, between the central cell and the carbon containing cell. For the other three cells, mass transport occurs by diffusion. The equation for the oxygen concentration of the central cell becomes

$$C(i, j) = \frac{[C(i, j-1) + C(i-1, j) + C(i, j+1)] + Sh_x [C(i+1, j)]}{(3 + Sh_x)} \quad (20)$$

When two neighboring cells contain carbon and two contain the stagnant gas, as for cell 3 in Figure 36, the equation becomes

$$C(i, j) = \frac{[C(i, j-1) + C(i-1, j)] + Sh_x [C(i, j+1) + C(i+1, j)]}{(2 + 2 Sh_x)} \quad (21)$$

It should be noted that when a cell is completely filled with carbon, it will have zero oxygen concentration. Therefore in Equations (20) and (21) above, the terms in the numerator that are multiplied by the local Sherwood number will be equal to zero.

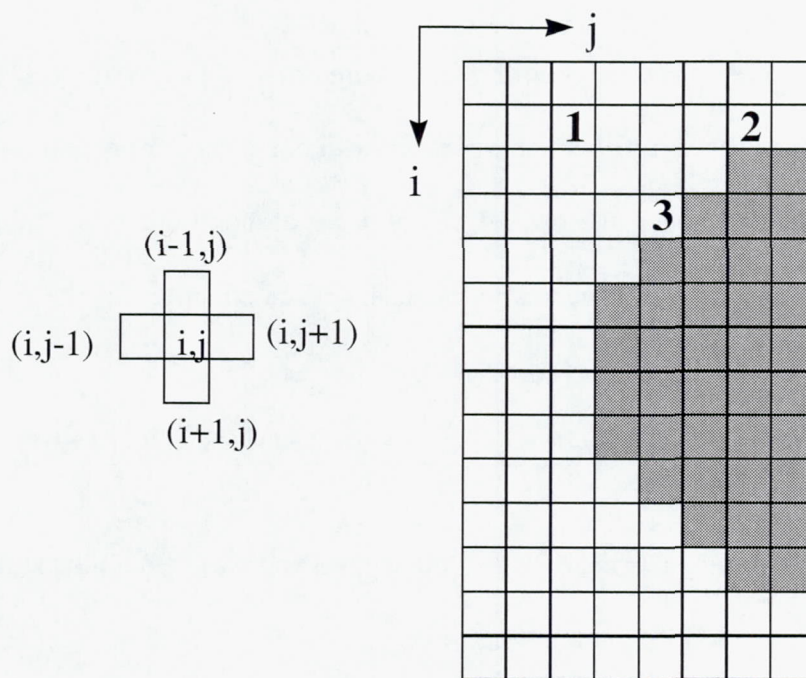


Figure 36. Detail of the cell pattern near a fiber tow.

The program was run for several different  $Sh_x$  values: 0.0001, 0.001, 0.01, 0.1, 1.0, and 10. The oxygen concentration for each cell was determined throughout the 2-D plane based on the boundary condition and the equations for oxygen concentration. The program was run until steady-state was reached. Carbon was not removed at this stage in the model development. Steady-state in the program may be thought of as the model having a continuous supply of oxygen from the edge and a continuous supply of carbon from the fiber tow array, or equivalently, as the state achieved just at the instant when the carbon is to react. The local oxygen concentration for each cell throughout the mesh pattern was calculated. The process was carried out over hundreds of iterations until the convergence criterion is met, i.e., oxygen concentrations no longer change (less than 0.1% change). The continuous supplies of carbon and oxygen and the specific local Sherwood number will determine an overall gradient in oxygen concentration from the edge to the interior at steady-state. Calculated oxygen concentrations will be presented in the results section.

### 3.1.2 Carbon Consumption

The next step in the model development was to include volume loss of carbon due to the carbon/oxygen reactions. The reaction rate at a given temperature is dependent on the rates of oxygen supply and carbon reactivity. Therefore diffusion coefficients and reaction rate constants had to be determined for each temperature. These inputs provided specific local Sherwood numbers that correlated with temperature.

The reaction rate constant was determined from the following equation:

$$K = \frac{(k_1 N)}{\chi C_t} \quad (22)$$

where  $N$  is the molar density of the carbon ( $\text{mol/m}^3$ ),  $C_t$  is the total gas concentration ( $\text{mol/m}^3$ ),  $k_1$  is the linear rate of carbon recession ( $\text{m/s}$ ), and  $\chi$  is the oxygen partial pressure in air. The reaction rate constant at  $800^\circ\text{C}$  was of interest since  $800^\circ\text{C}$  is often considered the transfer temperature from reaction-controlled to diffusion-controlled kinetics (Lamouroux *et al.* 1993; Eckel *et al.*, 1995) and since experimental data is available at this temperature (Eckel *et al.*, 1995). The density of carbon was taken as  $1.65 \text{ g/cc}$ . The total gas concentration was determined from the ideal gas equation where the temperature was  $800^\circ\text{C}$  and the pressure was  $1.013 \times 10^5 \text{ Pa}$  ( $1.0 \text{ atmosphere}$ ). The linear reaction rate was an experimentally determined value of  $2.5 \times 10^{-7} \text{ cm/s}$  for the oxidation of SCS-6 carbon at  $800^\circ\text{C}$  in air (Eckel *et al.*, 1995; Eckel, 1999). This gave a reaction rate constant of  $0.0153 \text{ m/sec}$ . Assuming a diffusion coefficient of  $1.79 \times 10^{-4} \text{ m}^2/\text{sec}$  (determined from Chapman-Enskog theory using the Lennard-Jones potential energy function) and a  $\Delta x$  of  $5 \times 10^{-5} \text{ m}$  (taken as one-half the distance between fiber tow arrays in the model and based on real composite geometries), the calculated local Sherwood value was  $4.25 \times 10^{-3}$ . For other temperatures, the diffusion coefficient was calculated using Chapman-Enskog theory. The reaction rate constants at other temperatures were determined by taking the ratio of the reaction rate constants at  $800^\circ\text{C}$  and another temperature of interest such that

$$\frac{K_T}{K_{800\text{C}}} = \frac{k_o \exp\left(\frac{-Q}{RT}\right)}{k_o \exp\left(\frac{-Q}{RT_{800\text{C}}}\right)} \quad (23)$$

In the above equation, the same activation energy was used for all temperatures. The

activation energy determined for regime 1 from TGA test of carbon fiber was used (64.1 kJ/mol). The main purpose in the analysis was to obtain fairly realistic low and high local Sherwood numbers which correlate to temperature so that reaction-controlled and diffusion-controlled kinetics could be modeled.

The next step in the generalization of the model was to include the process of carbon recession within the carbon fiber tow array. This involved allowing incremental carbon recession, in a method used by Glime and Cawley (Glime and Cawley, 1995). In this method, a quasi-steady-state of oxygen concentration throughout the cell pattern was determined. Then the entire array was examined to determine the time necessary for each exposed carbon cell to be completely reacted at the instantaneous local oxygen concentration. The smallest time increment was determined from this set, and then, oxidation was allowed to occur throughout the array for that amount of time. The oxygen concentrations were then recalculated until a quasi-steady-state was again reached. The process of carbon removal in short time steps and recalculations of all local oxygen concentrations was repeated iteratively until the desired amount of carbon had been removed.

When analyzing the results from initial calculations using this model, it was observed that certain surfaces of the 'circular' fiber tows were reacting at a faster rate so that the circle assumed a diamond shape. This effect, due to representing a circular region with square cells, can be understood by the 2-D illustration in Figure 37. This circle shows the smooth surfaces (edges) and rough surfaces (diagonals) that make up the circle. Cell 1, located on the diagonal, has two sides exposed while cell 2, located on the smooth edge, only has one side exposed. By determining the

net flux, setting it equal to zero and solving for the oxygen concentration in cell 1, the oxygen concentration was found to be equal to

$$C(i, j) = \frac{C(i-1, j) + C(i, j+1)}{(2 + 2 Sh_x)} \quad (24)$$

At quasi-steady-state the open oxygen containing cells,  $C(i-1, j)$  and  $C(i, j+1)$ , will have nearly the same oxygen concentration. Therefore equation (3) becomes

$$C(i, j) = \frac{2C(i-1, j)}{(2 + 2 Sh_x)} \quad (25)$$

The oxygen concentration for a partially oxidized carbon containing cell on the smooth edge, cell 2, was calculated to be

$$C(i, j) = \frac{C(i, j-1)}{(1 + 1 Sh_x)} \quad (26)$$

which will have nearly the same concentration at quasi-steady-state as cell 1. The time to oxidize cell 2 was

$$t = \frac{d \Delta x}{K C(i, j)} \quad (27)$$

where  $d$  is the density of carbon. The same time equation was being used for both cell 1 and cell 2. However the exposed edge for cell 1 does not have a length of one cell as for cell 2. A geometry correction was needed so that the square cell was considered as a triangle to more closely represent the smooth arc of the overall circle. The exposed surface area is along the diagonal of the cell and has a length of the square root of 2 cell lengths. With the geometry correction the time for cell 1 to oxidize was

$$t = \frac{d \Delta x}{\sqrt{2} K C(i, j)} \quad (28)$$

A circular core of bulk carbon with a radius of 59 cells was reacted without the geometry correction and with the geometry correction. Oxidation patterns as the core was reacted is shown in the results and continues this approach. The rates of carbon recession along the rough and smooth surfaces will be presented in the discussion. The carbon recession rate along the smooth surface was tracked by recording the radius of the shrinking core from the center out to the smooth surface (i.e, the radius at 0 degrees form horizontal). The carbon recession rate along the rough surface was tracked by recording the radius of the core from the center out to the rough surface (i.e, the radius at 45 degrees form horizontal). The oxidation of a 12 x 12 array of carbon fiber tows for a low and a high local Sherwood number will also be presented in the results. The conditions at 700°C gave a low local Sherwood number. The conditions at 1400°C gave a high local Sherwood number. An activation energy of 64.1 kJ/mol was used. Inputs for the local Sherwood numbers at each temperature were given in Table I. The oxygen concentration at the external boundary also had a temperature dependency.

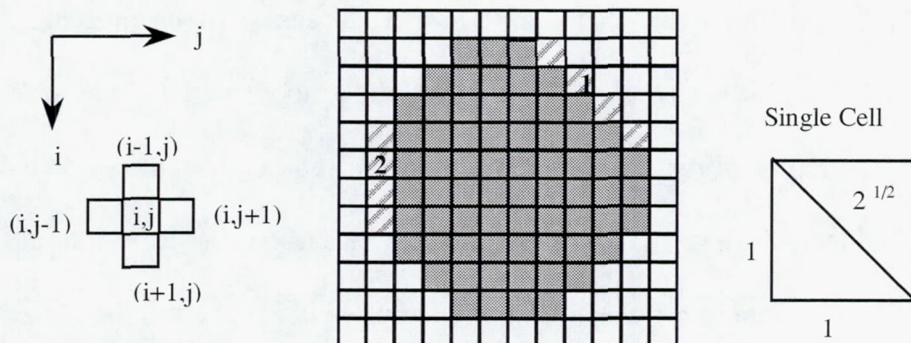


Figure 37. Circular core of carbon represented by square cells. Cell orientation is shown at the left. Center figure shows the 10 cell diameter pattern used to represent a fiber tow showing smooth and rough edges. Side and diagonal lengths are shown in the single cell to the right.

### 3.1.3 Model Geometry Study and Comparison to Analytical Solutions

Further analysis of the model was conducted at steady-state conditions. Steady-state oxygen concentrations were calculated using the finite difference model for several different geometries. The geometries considered were a square and several different sized rectangles. The main purpose of the geometry studies was to determine when the section was sufficiently wide so that oxygen diffusion from the long ends did not significantly contribute to the final oxygen concentration obtained for the center of the section, i.e., end effects are absent. In this case, the oxygen concentration in the center of the section would be primarily due to diffusion from the ends of the shorter dimension, i.e., the thickness. The first rectangle had a width that was twice the thickness. The

second rectangle had a width three times the thickness. A square that had the same width and thickness was also considered. In the final rectangle considered, the thickness was the same as for the square and the other rectangles, however the width was infinitely large. The infinitely large width was achieved by using periodic boundary conditions.

The model was also used to study oxygen diffusion down a single column that is bounded by reactive continuous carbon walls. This allowed the model to be compared to analytical solutions. Agreement between the analytical solutions and the finite difference model allowed for a check for the finite difference modeling method that was used. The comparison also helped determine which method of analysis would be sufficiently accurate for future cases/geometries to be investigated.

Illustrations of the square and rectangles are shown in Figures 38a-c. These illustrations represent cross sections of crack bridging planes that include an array of crack bridging fiber tows. They represent the different models: the 12 x 12, 12 x 24, and 12 x 36 fiber tow array finite difference models (the 12x12, 12x24, and 12x36 FTA models respectively). The overall dimension of cells in these models were 250x250, 250x490, and 250x730 respectively. In Figure 38a-c, fiber tows were 10 cells in diameter and were spaced 10 cells from one another and from the edge. It should be noted that Figure 38 only illustrates the boundaries, fiber tows, and open bridged regions. Detail of the square mesh patterns are not shown. The finite difference models were used to calculate the steady-state oxygen concentration for the diffusion of oxygen from the external edge to the interior of the sample. In the analysis, only the initial steady-state condition was considered, no effort was effort was made to study the kinetics.

Figure 38d illustrates the case of diffusion of oxygen down a single column bounded by fiber tows whose profiles extend into the column. In this model, called the bumped wall finite difference model (BW model) the outer walls are no flux boundaries which allow the model to consider the case of an infinitely wide fiber tow array (i.e., 12 x infinity). There was no diffusion of oxygen into the column from the sides. The resulting oxygen concentration in the column arises only from the diffusion of oxygen from the open ends into the column. Again the fiber tows were 10 cells in diameter and they were spaced 10 cells apart. The column was 250 cells long. Results from the BW model will be compared to oxygen concentrations along the midline of the 12x12, 12x24, 12x36 FTA models in order to determine when large geometries can be simplified to the BW model.

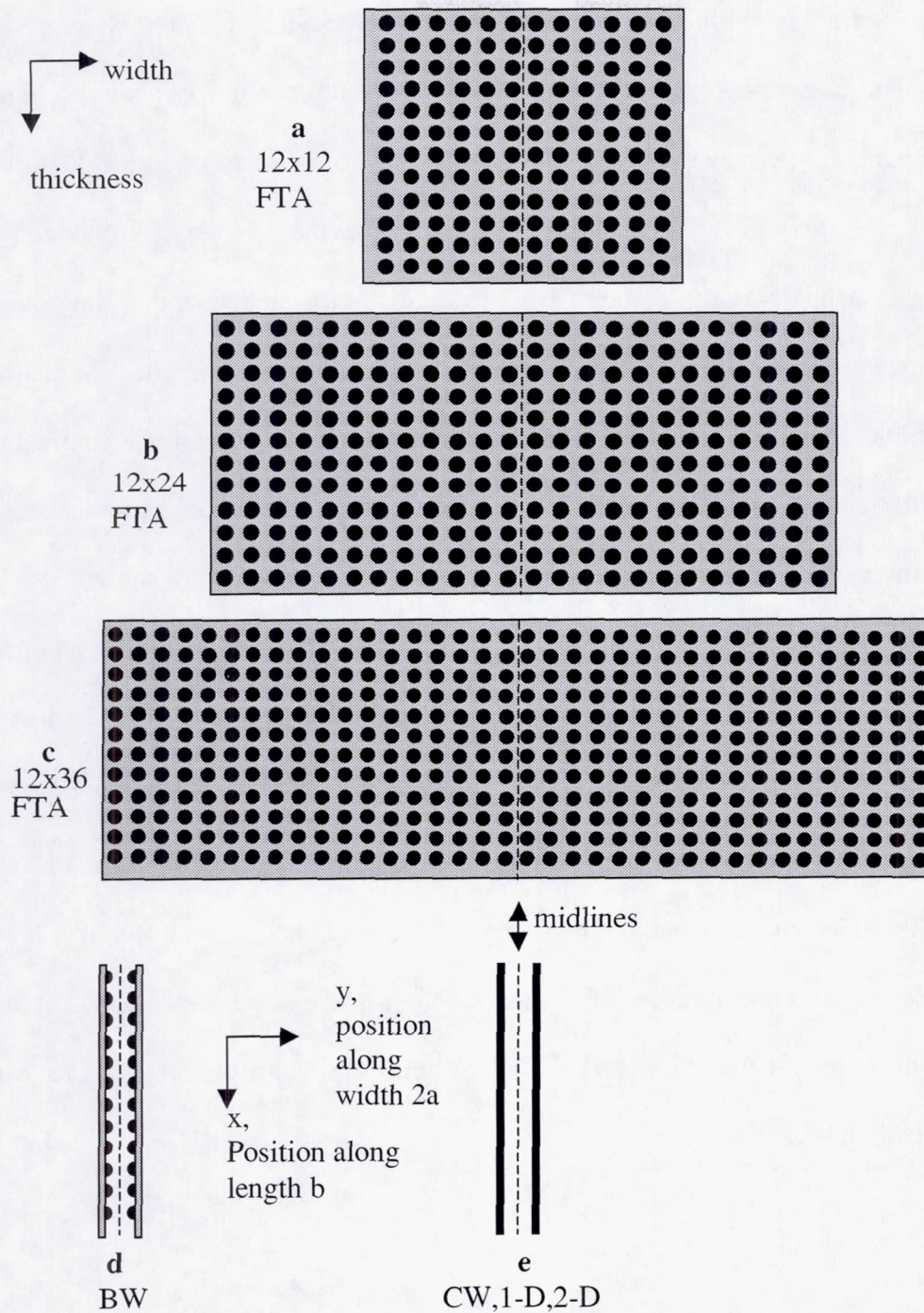


Figure 38a-e. Cases considered in the models. Cross-sections of arrays of fiber tows that bridge a crack in a matrix are shown in Figure 38a-c. Figures a, b, and c illustrate the 12 x 12, 12 x 24 and 12 x 36 FTA models of bridging reactive carbon fiber tows. Figure 38d illustrates the BW model of a single column bounded by fiber tow profiles evenly spaced on each side with no-flux boundary walls. Figure 38e is a single column bounded by reactive carbon walls (used for the CW model and the 1-D and 2-D analytical solutions).

The final scenario to be considered in the analysis was for the case represented in Figure 38e. This was for the diffusion of oxygen down the length of a single column that was bounded by two walls of reactive carbon. The column was open for diffusion from the ends. The geometry may be thought of as similar to the geometry for the bumped wall model but in this case the carbon fiber tows are so close together that they make up a continuous wall of carbon. This geometry was analyzed using the finite difference method and analytical solutions. A finite difference model, called the continuous wall finite difference model (CW model), was used to determine the oxygen concentration at steady-state. One-dimensional (1-D) and two-dimensional (2-D) analytical solutions were also used to calculate the oxygen concentrations at steady-state. Results from the CW model were compared to the 1-D and 2-D analytical solutions in order to see how well the finite difference method compared to analytical mass transport expressions.

The geometry for the analysis of diffusion down a single column is illustrated in Figure 39. Each end of the column was exposed to the atmosphere, which was arbitrarily set at an oxygen concentration of 1. The column had a width of  $2a$  and length of  $2b$ , where the length of the column was 250 cells and the width was 10 cells from carbon wall to carbon wall.

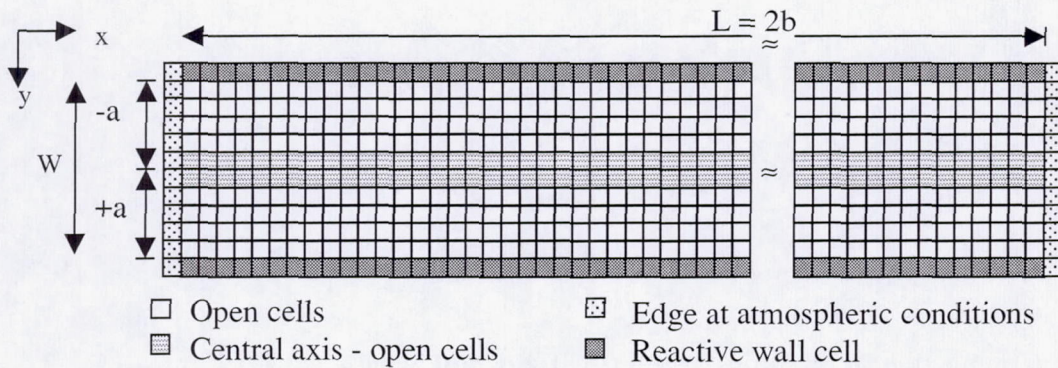


Figure 39. Geometry of cracked carbon material where oxygen diffuses down an open column bounded by carbon.

The first analytical solution to be analyzed for the oxygen concentration at steady-state is the 1-D case for a finite rod with the ends at a fixed oxygen concentration. The solution for this case of mass transport is entirely analogous to Carslaw and Jaeger's solution for heat transfer. The derivation here will be in mass transport. The equation for the change in concentration with time is

$$\frac{\delta C}{\delta t} = \frac{D \delta^2 C}{\delta x^2} - \frac{K p C}{\omega} \quad (29)$$

The term,  $\omega$ , is the cross-sectional area of the rod ( $2b \times 2a$ ). The term,  $p$ , is the perimeter of the rod ( $4b + 4a$ ). When the length is much greater than the width, the perimeter can be approximated as  $4b$ . By rearranging Equation (29) and substituting, the following 2<sup>nd</sup> order equation is obtained:

$$\frac{\delta^2 C}{\delta x^2} - \mu^2 C = 0 \quad (30)$$

The term  $\mu$  is defined by:

$$\mu^2 = \frac{K p}{D \omega} \quad (31)$$

By substituting for the cross-sectional area and the perimeter, Equation (31) becomes:

$$\mu^2 = \frac{4bK}{2b \cdot 2aD} = \frac{K}{Da} \quad (32)$$

which is equal to

$$\mu^2 = \frac{Sh_x}{a^2} \quad (33)$$

The boundary conditions give us the following equations:

$$C = C_1, \text{ at } x = 0, \text{ and} \quad (34)$$

$$C = C_2, \text{ at } x = 2b. \quad (35)$$

The solution is

$$C = Ae^{\mu x} + Be^{-\mu x} \quad (36)$$

Where

$$C_1 = A + B \quad (37)$$

$$C_2 = Ae^{\mu 2b} + Be^{-\mu 2b} \quad (38)$$

The 1-D analytical solution for the oxygen concentration in a column bounded by reactive carbon walls, is

$$C(x) = \frac{C_1 \sinh[(Sh_x/a^2)^{1/2} (2b-x)] + C_2 \sinh[(Sh_x/a^2)^{1/2} x]}{\sinh[(Sh_x/a^2)^{1/2} (2b)]} \quad (39)$$

Equation (39) correlates with Carslaw and Jaeger's 1-D solution for heat transfer and is similar to the mass transport equation used by Geankoplis (Carslaw and Jaeger, 1950; Geankoplis, 1978). The oxygen concentration at each end is  $C_1$  and  $C_2$  respectively and they are equal in our case. The position along the length is  $x$  and the column length is  $b$ . Note that Equation (39) has a term for the total width of the rod, where  $a$  is one-half the width. However, the equation does not allow for oxygen concentration to be determined

at different positions along the width, i.e, values of  $y$ . Therefore this solution is only good for small cross-sections since the oxygen concentration at a given position along  $2a$  is the same for all points along the width.

The derivation of the 2-D mass transport analytical solution, again, will follow a derivation similar to Carslaw and Jaeger's derivation for heat transfer (Carslaw and Jaeger, 1950). The difference will be that this solution and discussion will involve mass transport terms and a substitution for an alpha term. For steady-state conditions, mass transport due to diffusion into a medium and reactions at the surface, the following differential equation is used:

$$\frac{\partial^2 C}{\partial x^2} + \frac{\partial^2 C}{\partial y^2} = 0 \quad (40)$$

The geometry is the same as for the 1-D derivation, however one quarter of the rod shown in Figure 39 defines the boundary. The boundary conditions are

$$C = f(y) \quad \text{at } x=0, \text{ for } 0 < y < a, \quad (41)$$

$$\frac{\partial C}{\partial y} = 0 \quad \text{at } y=0, \text{ for } 0 < x < b, \quad (42)$$

$$\frac{\partial C}{\partial x} = 0 \quad \text{at } x=b, \text{ for } 0 < y < a, \text{ and} \quad (43)$$

$$\frac{\partial C}{\partial y} + fC = 0 \quad \text{at } y=b, \text{ for } 0 < x < b \quad (44)$$

A solution to Equations (40), (42) and (43) is  $[\cos \alpha y \cosh \alpha(b-x)]$  and also satisfies Equation (44) if  $\alpha$  is a root of (Carslaw and Jaeger, 1950)

$$\alpha \tan a\alpha = f \quad (45)$$

where

$$f = \frac{Sh_x}{a} = \frac{K}{D} \quad (46)$$

Multiply both sides of Equation (39) by the width term,  $a$ , such that

$$a\alpha \tan a\alpha = \alpha' \tan \alpha' = f a = Sh_x \quad (47)$$

where  $\alpha' = a\alpha$

The analytical solution for the 2-D case when  $C = f(y)$  is a constant is

$$C(x, y) = 2 \frac{Sh_x}{a} C_o \sum_{n=1}^{\infty} \frac{\cos(\alpha'_n y / a) \cosh[(\alpha'_n / a)(b-x)]}{\{[(\alpha'_n / a)^2 + ((Sh_x / a)^2)a] + Sh_x / a\} \cos(\alpha'_n) \cosh(\alpha'_n b / a)} \quad (48)$$

The 2-D mass-transport solution represented in Equation (48) is similar to Carslaw and Jaeger's heat transfer solution (Carslaw and Jaeger, 1950). The oxygen concentrations are the same at both ends,  $C_o$ . It is seen that this 2-D solution allows for variations in the position ( $y$ ) along width ( $2a$ ). This 2-D solution allows geometries that have a large cross-section to be considered. Thus local oxygen concentrations for specific positions and gradients in oxygen concentration can be determined in both the  $x$  and  $y$  directions.

It should be noted that in comparing the CW model with the 1-D and 2-D analytical solutions, an adjustment had to be included so that the analytical solutions considered exactly the same local Sherwood number as the CW model which used the finite difference method. In the finite difference method, even though the reactive carbon walls were spaced 10 cells apart,  $\Delta x$  was taken as one cell space. For the analytical solutions, the carbon walls were also spaced 10 units apart, however  $\Delta x$  was taken as 5 unit spaces. Therefore the analytical solutions, were analyzed with a local Sherwood number that was 5 times the local Sherwood number used in the finite difference method so that the  $K/D$  value was the same in all methods of analysis. An alternate way of considering this

adjustment is if the factor of five in front of the local Sherwood number is taken to the other side, the local Sherwood numbers will be the same. For example the equations for the local Sherwood number used in the analytical solutions is

$$5 \text{Sh}_x = \frac{K \Delta x}{D} \quad (49)$$

while for the finite difference method the solution is

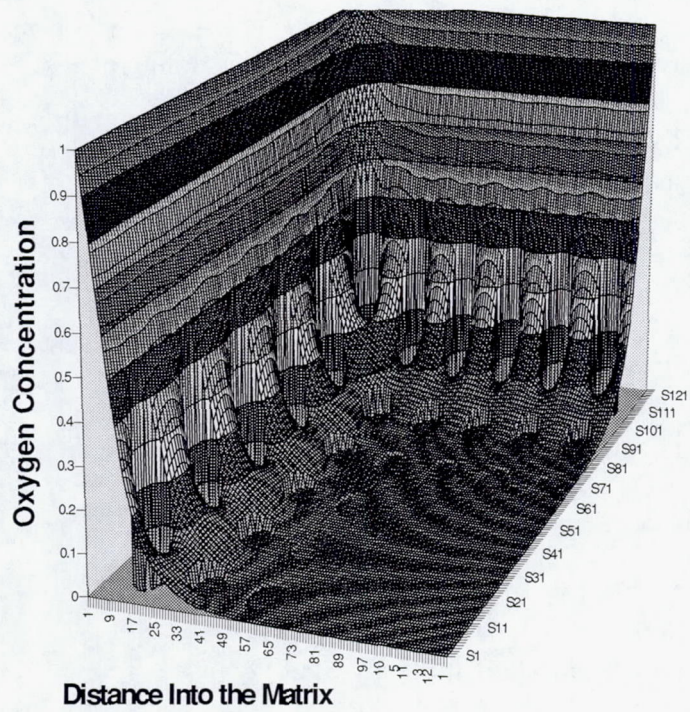
$$\text{Sh}_x = \frac{K \Delta x}{D} \quad (50)$$

When the factor of 5 is taken away from both sides of Equation (49), Equations (49) and (50) are equivalent.

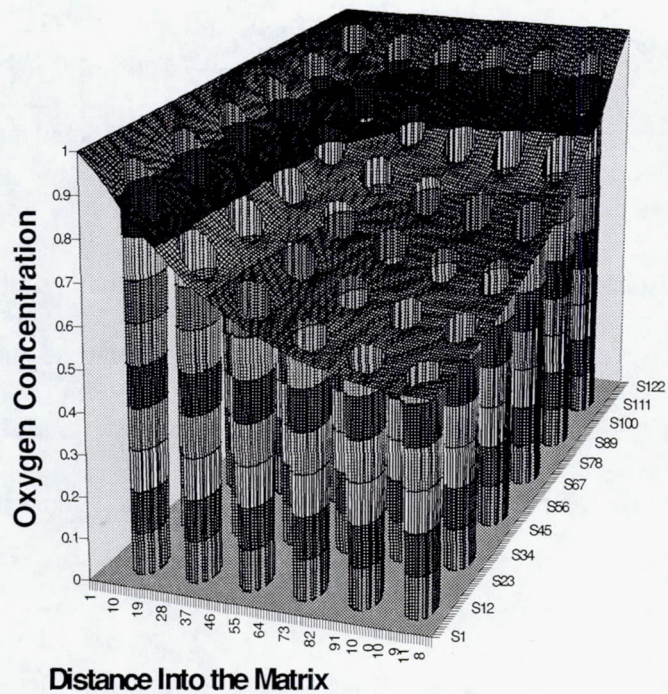
## 3.2 Results

### 3.2.1 Oxygen Concentration at Steady-State

For a given local Sherwood number, the calculated oxygen concentration at steady-state was used to prepare 3-D plots that represent the entire 2-D plane within the fiber bridged region. Sample plots for the oxygen concentration at a low local Sherwood number and a high local Sherwood number are given. Figure 40a shows the oxygen concentrations for one-quarter of the whole 2-Dimensional plane for a relatively high local Sherwood number,  $\text{Sh}_x=0.1$ . The case for a relatively low local Sherwood number,  $\text{Sh}_x=0.001$ , is shown in Figure 40b. The plots show gradients in oxygen concentration from the edge to the interior and the degree of oxygen saturation or depletion in the interior.



Distance Into the Matrix



Distance Into the Matrix

Figure 40a-b. Oxygen concentration at steady-state for  $Sh_x=0.1$  (above) and  $Sh_x=0.0001$  (below). One-quarter plots (125x125) of a 250x250 matrix with a 12x12 fiber array. Interated to equilibrium/steady-state.

In the previous figure, the curves at the edges of the plots represent the oxygen concentration through one-half of the thickness of the section. Full plots of the oxygen concentrations across the midline are shown in Figure 41 for several local Sherwood numbers. This represents the oxygen concentration from edge to edge across the middle of the 250x250 cell pattern for the 12x12 fiber tow array.

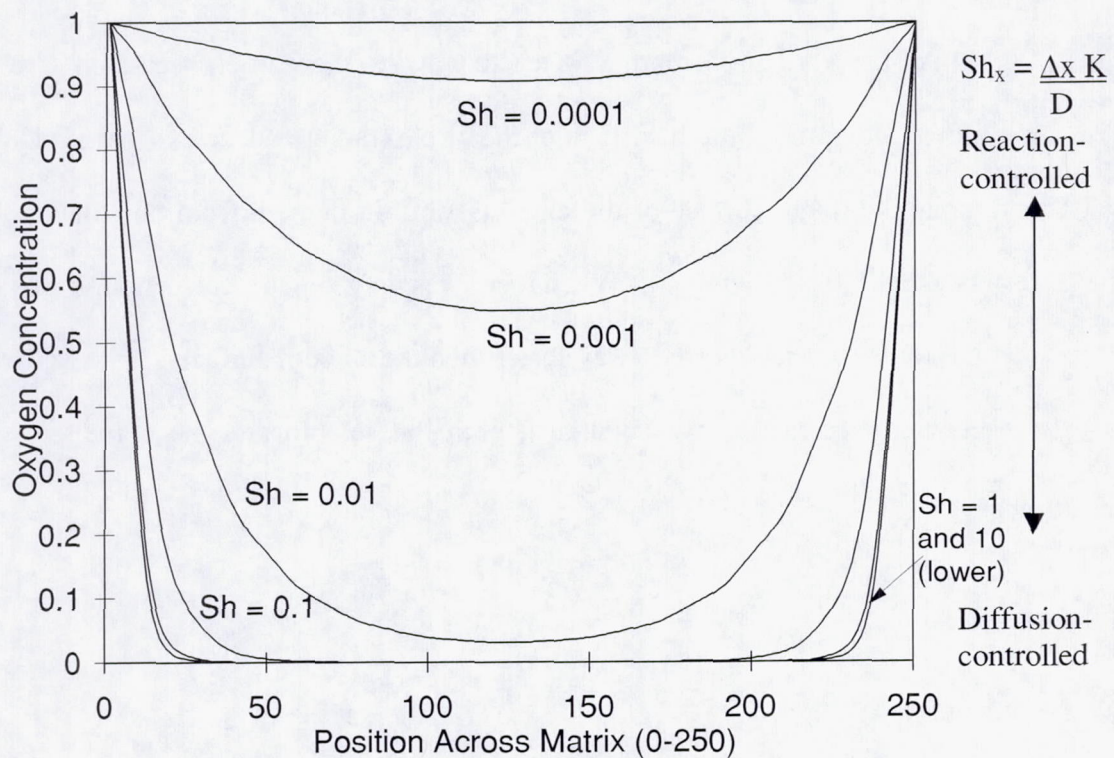


Figure 41. Oxygen concentrations across the center of the surface for several local Sherwood ( $Sh_x$ ) values.

### 3.2.2 Carbon Consumption

Due to the circular core of carbon being represented by square cells, a rough edge consisting of square cells was observed to react faster than an edge that was represented as smooth. An example of the oxidation pattern obtained for a circular core of carbon with a radius of 59 cells is shown in Figure 42 for several stages of oxidation. The oxidation pattern obtained when the geometry correction was included is shown in Figure 43.

As the core of carbon was reacted away, the carbon recession rate was monitored along the smooth surface of the circle (radius 0 degrees from horizontal) and along the rough surface of the circle (radius 45 degrees from horizontal). The results are shown in Figure 44. When there was no geometry correction, it was seen that the rough surface reacted away faster than the smooth surface. However, when the geometry correction was included, both the smooth and the corrected rough surfaces reacted at the same rate.

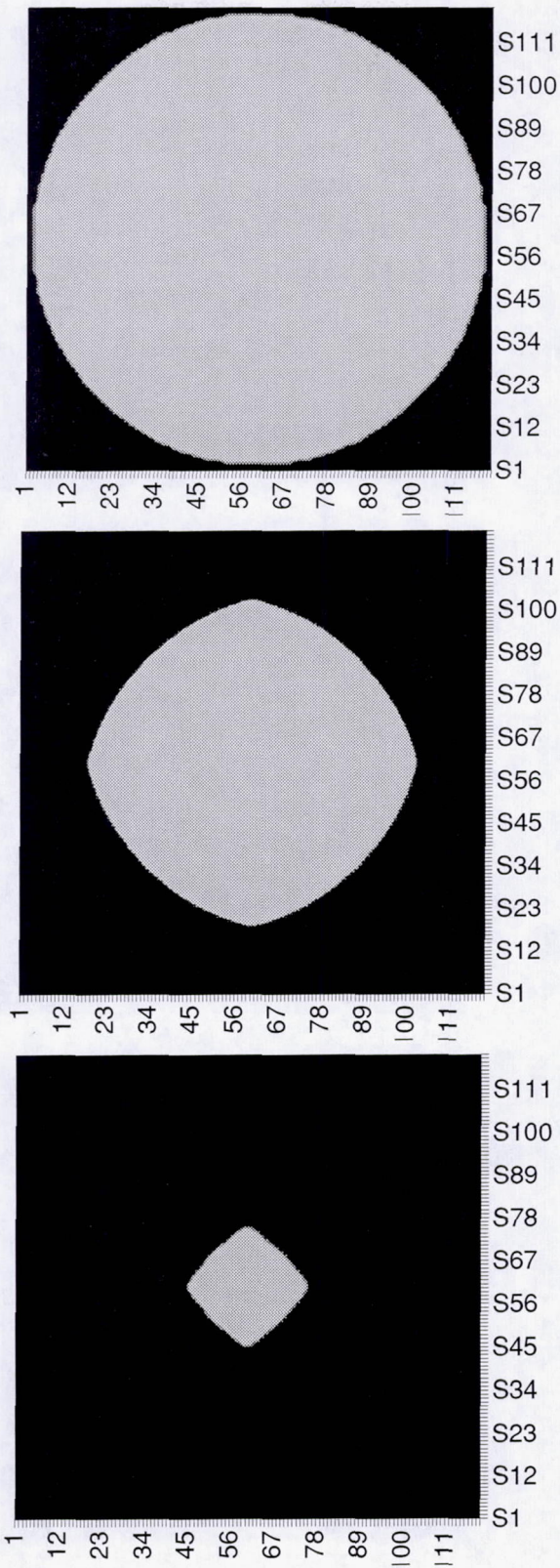


Figure 42. Shrinking core without geometry correction. The percentage of carbon consumed from the top to the bottom plot is 5%, 50%, and 95% reacted. Diamond shape is obtained.

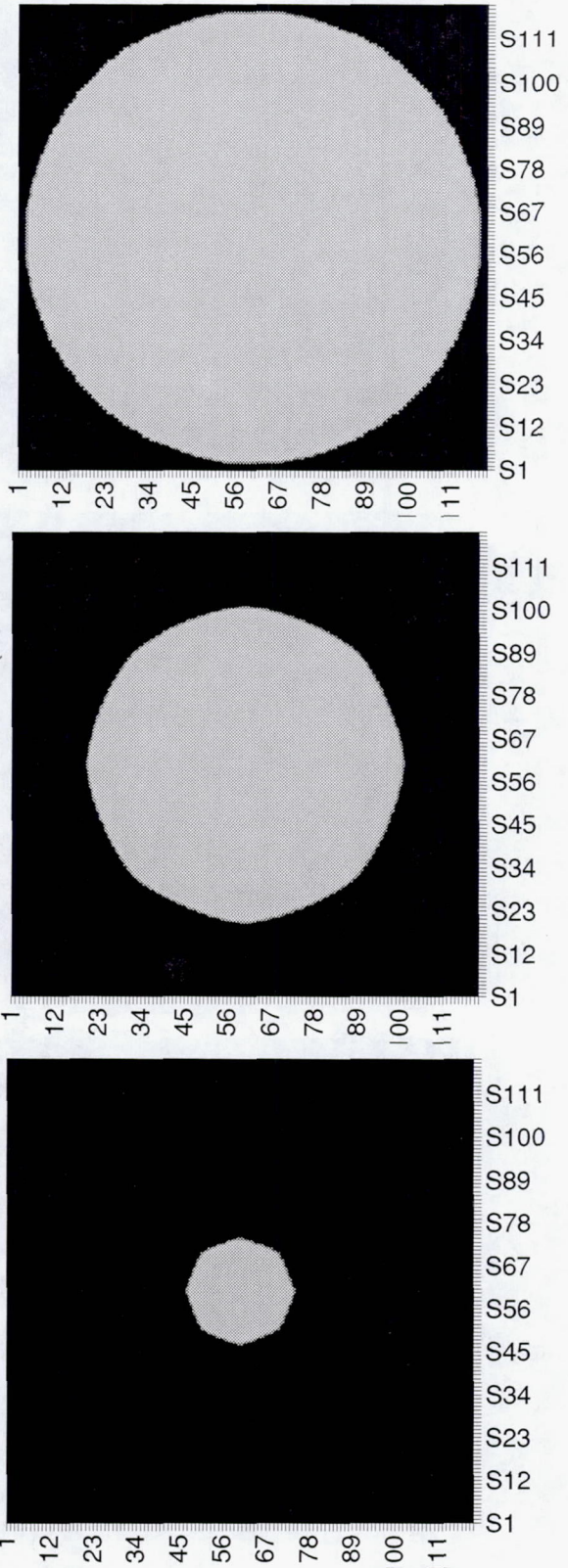


Figure 43. Shrinking core with geometry correction. The percentage of carbon consumed from the top to the bottom plot is 5%, 50%, and 95% reacted. Circular shape is more closely maintained.

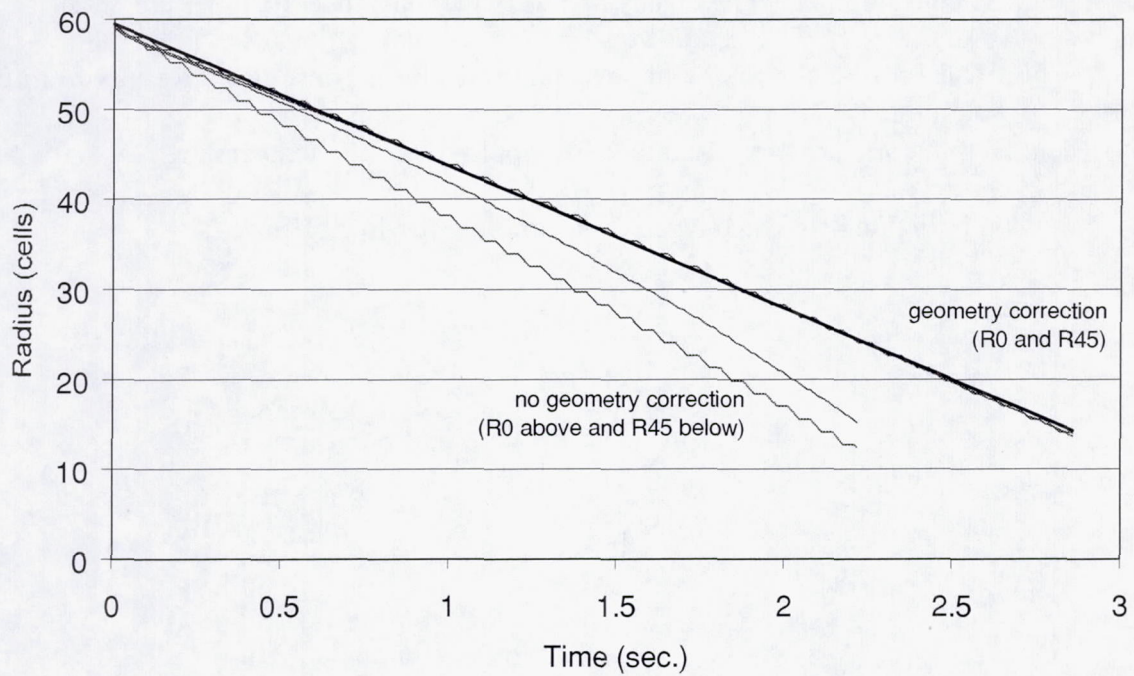


Figure 44. Radius reduction for reacting carbon core with and without geometry correction. The local Sherwood number was  $1.53 \text{ E-}3$ .

Now that the finite difference model had been advanced to consider carbon/oxygen reactions, the kinetics of oxidation in a fiber tow array were investigated and compared to experimental observations. Results from the model that correlate to the kinetics that would occur at a temperature of 700°C are shown in Figure 45 for a 250x250 mesh pattern with a 12x12 array of fiber tows. The carbon volume for the whole 2-D surface and the corresponding oxygen concentrations for one-quarter of the section are shown at various percentages of carbon consumption. The stages of the oxidation process shown are when 25%, 75%, and 95% of the total carbon volume had been consumed. Results from the model that correlate to the kinetics that would occur at a temperature of 1400°C are shown in Figure 46. The oxygen concentrations are in mol/cm<sup>3</sup>.

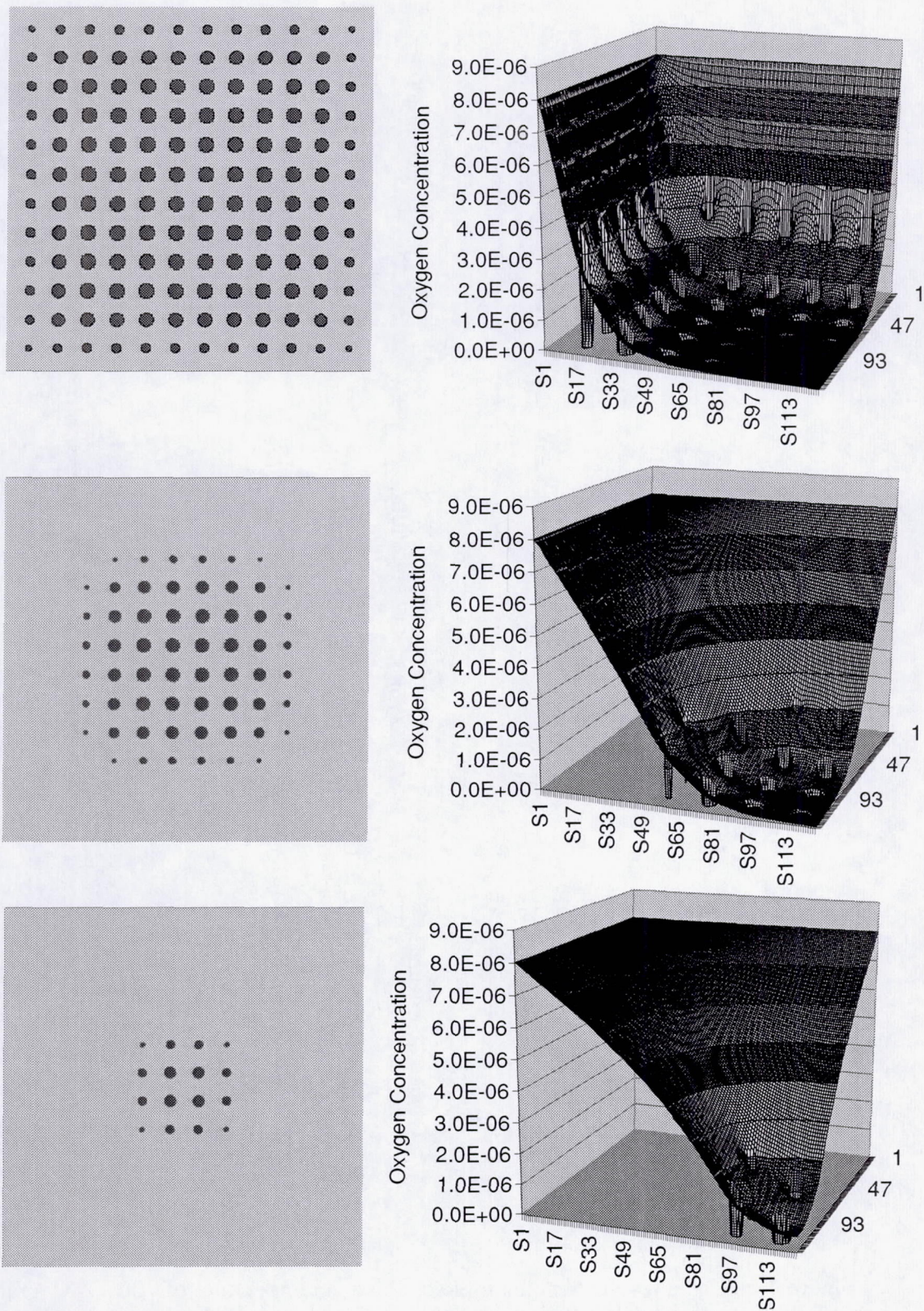


Figure 45. Model results for the cross-section at 1400°C. Overall oxidation pattern (left) and oxygen concentration for one-quarter section (right) for 25 %, 75 %, and 95 % of the carbon consumed (top to bottom).

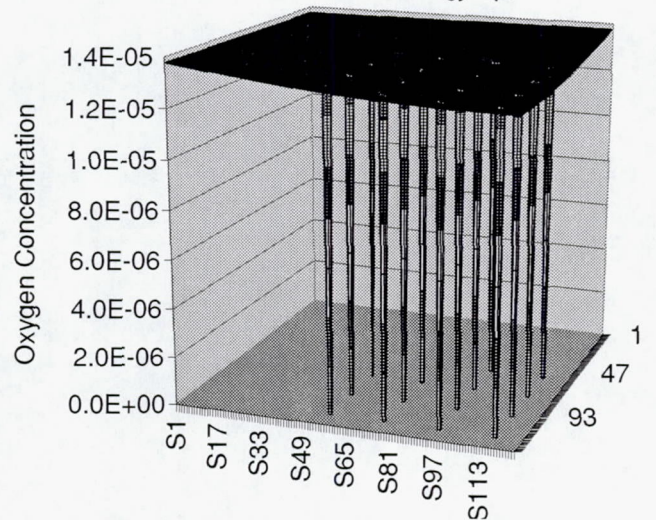
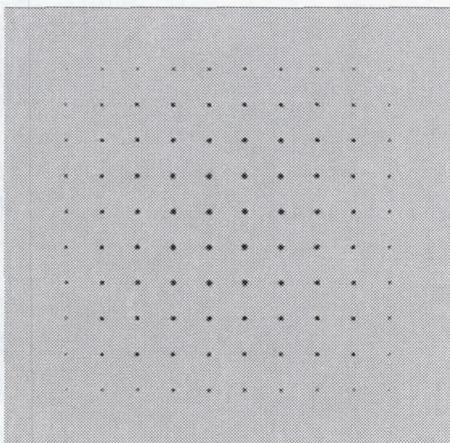
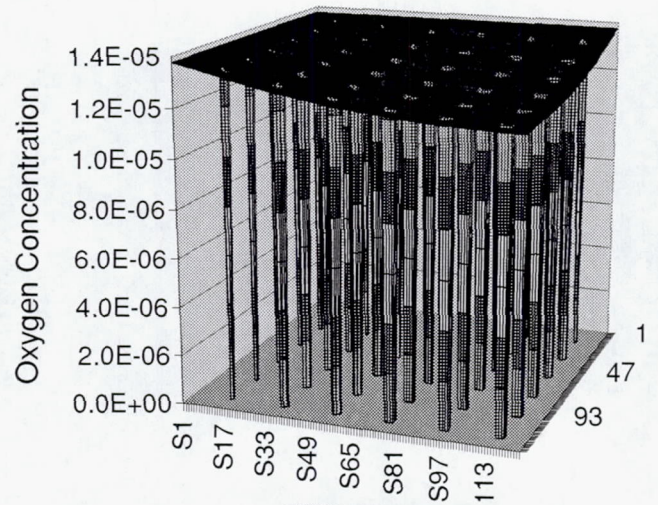
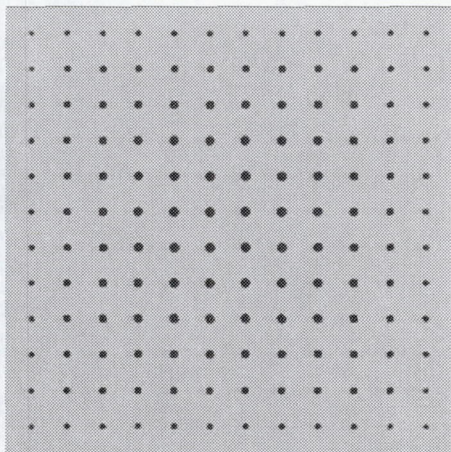
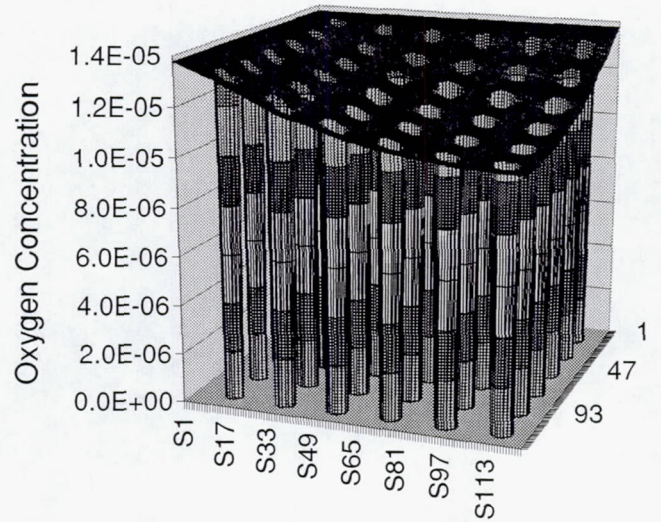
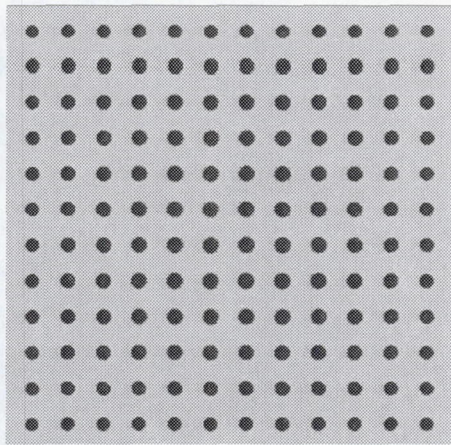


Figure 46. Model results for the cross-section at a temperature of 700°C. Overall oxidation pattern (left) and oxygen concentration for one-quarter section (right) for 25 %, 75 %, and 95 % of the carbon consumed (top to bottom).

### 3.2.3 Model Geometry Study and Comparison to Analytical Solution

The oxygen concentrations determined by the finite difference CW model, the 1-D analytical mass transfer solution, and the 2-D analytical mass transfer solution were compared. Resulting oxygen concentrations along the midline for these three types of analysis for the reactive wall case, as was illustrated in Figure 38e, are shown in Figure 47. All three methods gave a very similar prediction in oxygen concentration for low local Sherwood numbers. However, for higher local Sherwood numbers, i.e.  $Sh_x > 0.1$ , the 1-D analytical solution predicted a higher gradient in oxygen concentration than for the midlines of the CW model and 2-D analytical solution.

The 2-D analytical solution and the CW model allowed the oxygen concentration along any line for the 5 cell positions of a (one-half the width) to be determined. The oxygen concentrations for the five lines going from the midline to the line parallel to and adjacent to the carbon wall, are shown in Figure 48 for one-eighth of the distance into the column length. The CW model and the 2-D analytical solution compared very well with one another in both specific oxygen concentrations and in trends. At high local Sherwood numbers, the effect of position along the width can be seen. There was more of a gradient for the curve directly adjacent to the carbon wall compared to the midline. In each packet of five curves for each local Sherwood number, the curve with the lowest gradient in oxygen concentration is for the midline while the curve with the largest gradient in oxygen concentration is along the line directly adjacent to the carbon wall. The one curve predicted by the 1-D solution for each local Sherwood number appears in Figure 48 as the tick marked line.

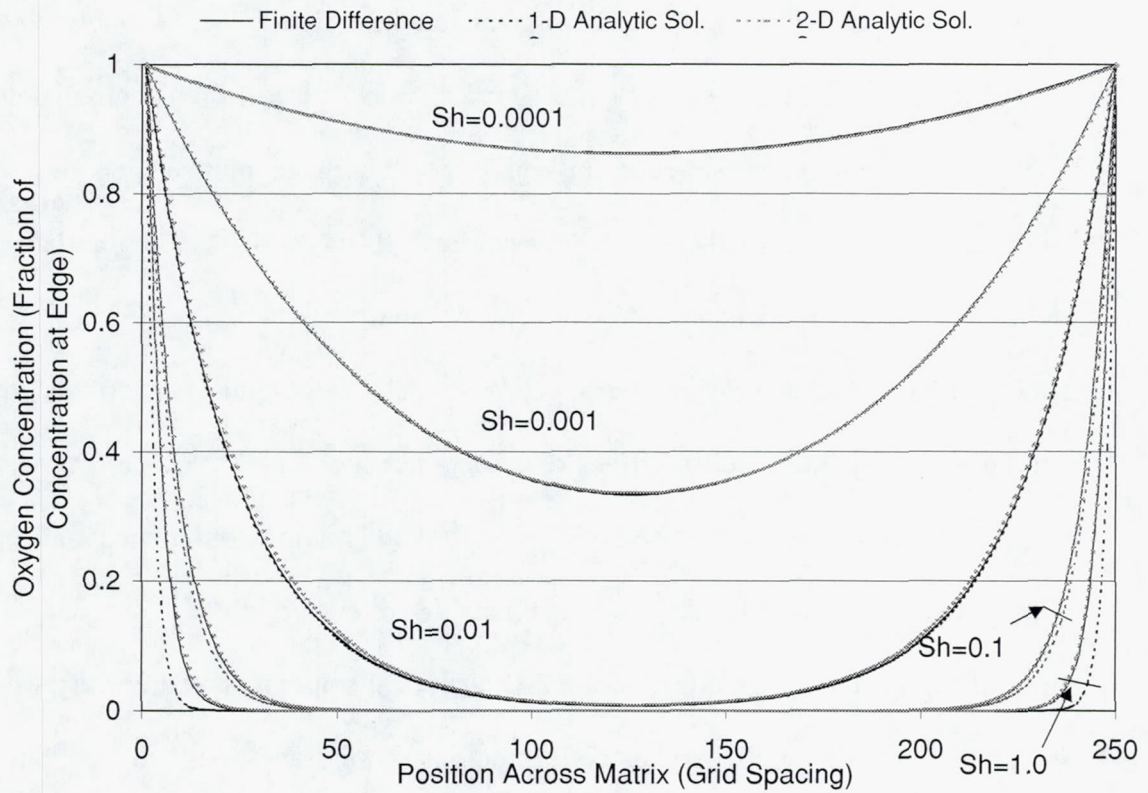


Figure 47. Oxygen concentration along the midline for the analysis of the case of diffusion of down a column bounded by continuous wall of carbon. The case was analyzed using the finite difference CW model, the 1-D analytical solution, and the 2-D analytical solution. Sherwood numbers are local Sherwood numbers.

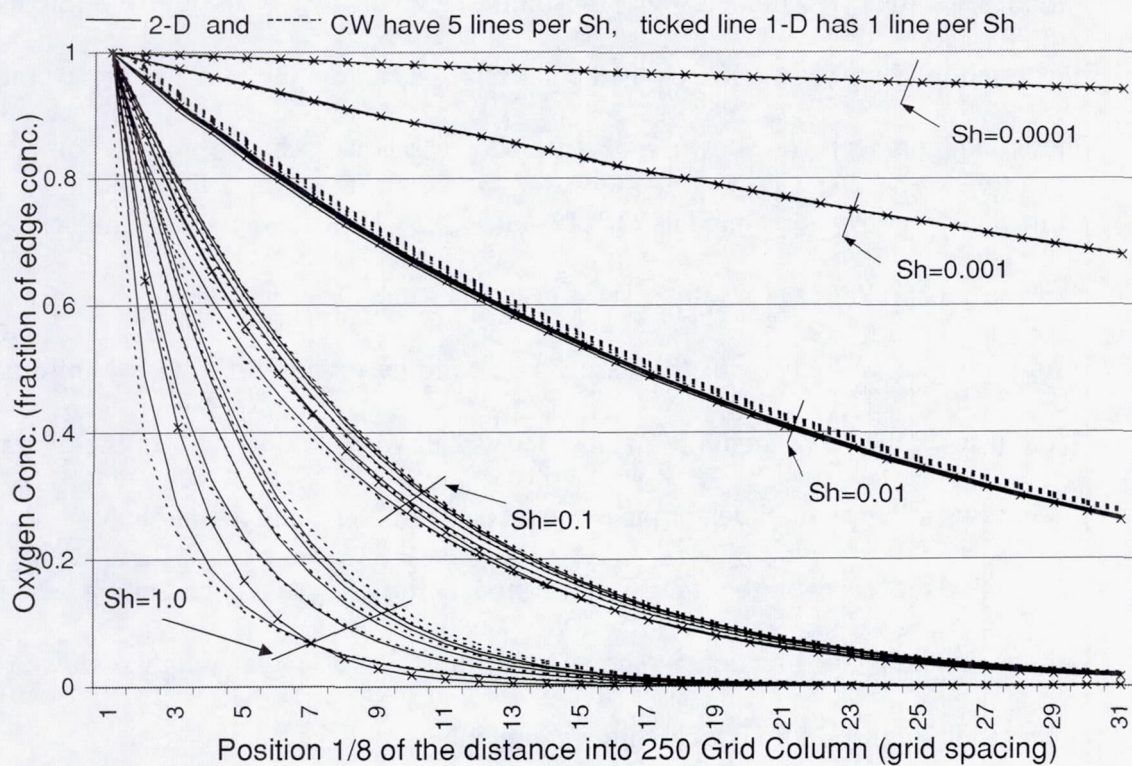


Figure 48. Oxygen concentrations one-eighth of the distance down the column length for the CW model and the 2-D analytical solution for the five line positions of width parallel to the midline. Concentrations for each Sherwood number are shown. Also the one line of oxygen concentration predicted by the 1-D model is shown. Sherwood numbers are local Sherwood numbers.

The finite difference model was used to study the effect of geometry. Specifically, how diffusion down the longer dimension of the width contributed to the overall oxygen concentration across the shorter dimension of thickness. The steady-state oxygen concentrations for the 12x12, 12x24, 12x36 FTA models, and the BW model were determined by the finite difference method. Illustrations of the geometries and the midlines for the FTA models were illustrated in Figure 38a-c and the BW model was illustrated in Figure 38d. The oxygen concentrations across the midline for several local Sherwood numbers are shown in Figure 49. At low local Sherwood numbers the narrower fiber tow array models (12x12 and 12x24 FTA models) gave higher oxygen concentrations along the midline. However when the array was larger, ie., 12x36, the results matched closely with the case for an infinitely wide array (12 x infinity also referred to as the BW model). At high local Sherwood numbers, all of the geometries gave very similar predictions for the oxygen concentration along the midline.

For the case of the 12x36 FTA model, the oxygen concentration across the midline in the long direction is shown in Figure 50. A wide trough of low oxygen concentration is seen for all local Sherwood numbers.

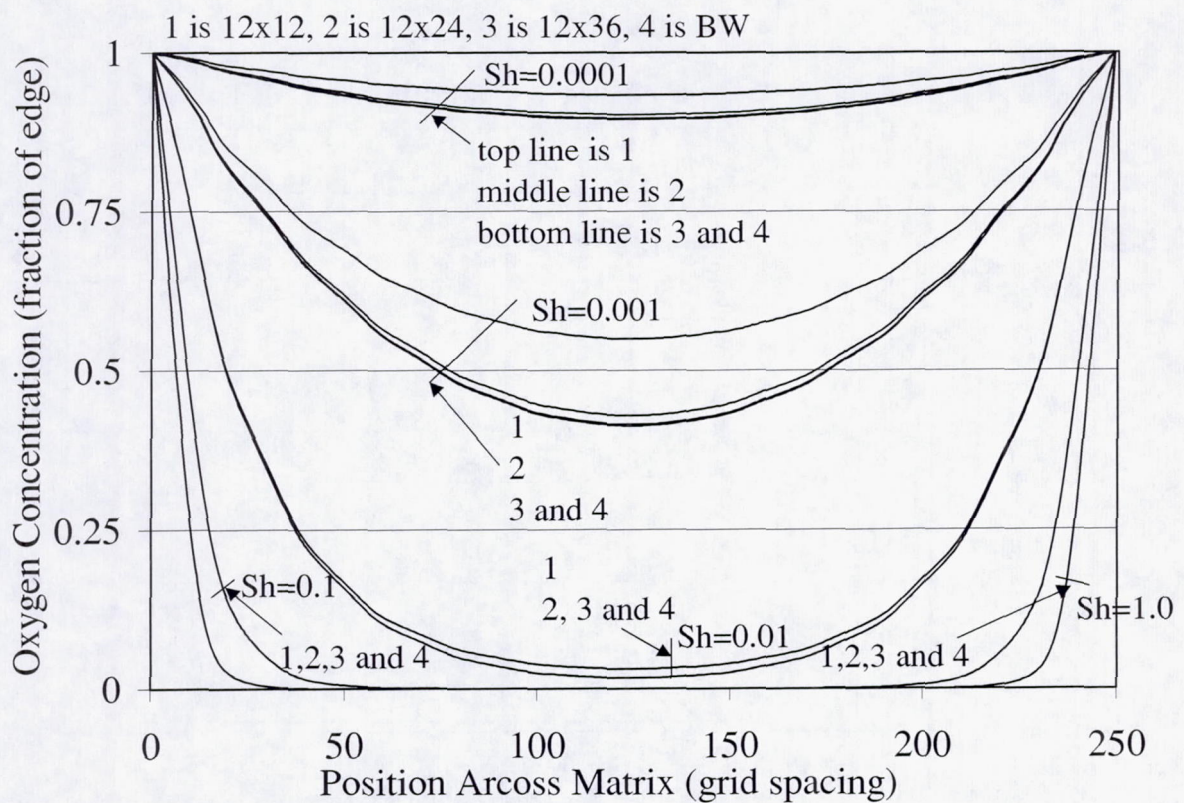


Figure 49. Oxygen concentrations across the midline for different geometries. Midlines were shown in Figure 38a-d for the 12x12, 12x24, and 12x36 FTA models and the BW model. The Sherwood numbers are local Sherwood numbers

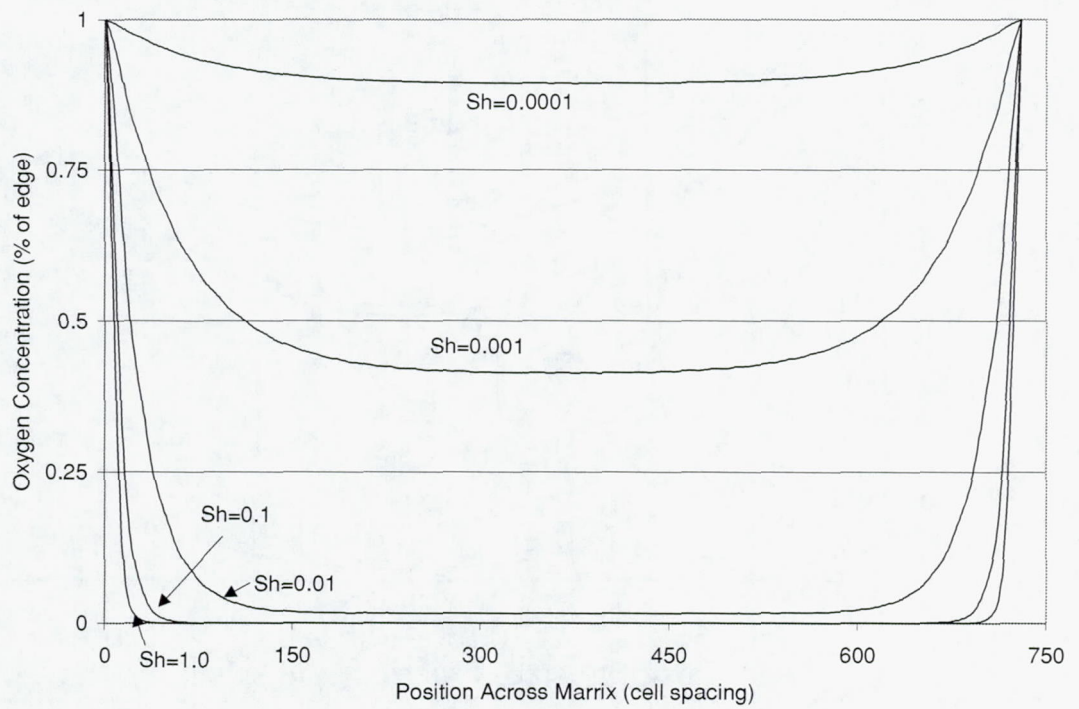


Figure 50. Oxygen concentration across the long dimension of the 12 x 36 FTA model. The Sherwood numbers are local Sherwood numbers.

### 3.3 DISCUSSION

#### 3.3.1 Oxygen Concentration at Steady-State

In the initial development of the model, the oxygen concentration at steady-state in a 250x250 mesh pattern with a 12x12 array of fiber tows was considered. Figure 40a-b showed the oxygen concentration for one quarter of the section at a high local Sherwood number and at a low local Sherwood number. In the plot for a low local Sherwood number, it was seen that the interior of the mesh pattern became highly saturated in oxygen concentration. The carbon was so slowly reactive that oxygen was able to bypass the carbon fiber tows at the perimeter and enter the interior. This pattern of a shallow gradient in oxygen concentration from the edge to the interior and an interior that is highly saturated in oxygen is the pattern that would be expected for reaction-controlled kinetics. Reaction-controlled kinetics occur at low temperatures and are characterized by a strong temperature dependence. However for a high local Sherwood number, it was seen that there was a sharp gradient in oxygen concentration from the edge to the interior. The carbon was so reactive that upon the oxygen's initial contact with carbon, a carbon/oxygen reaction occurs and no oxygen is able to bypass the outer perimeter of carbon fiber tows so that the interior became devoid of oxygen. This is the pattern that would be expected for diffusion-controlled kinetics. Diffusion-controlled kinetics occur at high temperatures. These patterns for the two main oxidation kinetics regimes will be discussed further in the Carbon Consumption section where the carbon is reacted away and realistic local Sherwood numbers are used.

The oxygen concentration at steady-state across the midline of the 12 x12 fiber tow array was compared for several different local Sherwood numbers. The results were

shown in Figure 41. The effect of the local Sherwood number on the resulting oxygen concentration can be seen for a wide range of values. At low local Sherwood numbers, oxygen is able to bypass the carbon so that it saturates the interior and is there in high concentrations. At high local Sherwood numbers oxygen is quickly consumed so that there is a large gradient in oxygen concentration from the edge to the interior. This type of analysis of a wide range of local Sherwood numbers can allow realistic values of the local Sherwood number to be calculated and then the plot can be referenced in order to determine the predicted kinetics regime and the gradients in oxygen concentration. Also, if two of the three variables for the local Sherwood number are known ( $K$ ,  $D$ , and  $\Delta x$ ), the effect of variation in the third variable can be determined.

### 3.3.2 Carbon Consumption

The geometry correction that was used in the analysis of the reactive circle allowed the circular shape to be more closely maintained. The radius at the smooth surface and at the rough surface oxidized at the same rate. However, it was unclear why both surfaces reacted at a slower rate than for the circle that had no geometry correction. In the circle that had no geometry correction, both radii may have reacted at a faster rate due to the "corner" cells that were shared between both the smooth surface and the rough surface. The rough surface was reacting at a faster rate and therefore the shared cell reacted at a faster rate. The shared cell may have caused the smooth surface to react at a faster rate due to its two outer cells reacting at a faster rate. When the geometry correction was added, this caused not only the rough surface to react more slowly but also the smooth surface. Figure 51 a-b show how the diameters compared at  $0^\circ$  from horizontal and  $45^\circ$  from horizontal for the cores when they were 95% reacted. When the diameter at  $45^\circ$  is

compared to the diameter at 0° for the core that did not have a geometry correction, it is seen that the diameter at 45° was only about 81% as large as the diameter at 0°. However for the core that had a geometry correction, the diameter at 45° was about 99.5% as long as for the diameter at 0°.

An example of the oxidation pattern within the fiber tow array and the corresponding oxygen concentration for reaction-controlled and diffusion-controlled kinetics were shown at the stages of 25%, 75%, and 95% of the carbon reacted. These results confirmed the trends for both kinetic regimes that were suggested by the analysis for steady-state conditions. However, the reduction in carbon area was also able to be analyzed and the progression of oxidation of the fiber tow array could be seen at various stages in the carbon area fraction plots and in the corresponding oxygen concentration plots.

The extension of the model to include carbon reactivity and a modification of the mesh pattern allowed for the analysis of a geometry that more closely corresponded to the cross sections of tested C/SiC samples. A mesh pattern of 970x330 cells was laid out to give a geometry comparable to the cross-sections of C/SiC tensile bars. With a cell having a length of  $1 \times 10^{-3}$  cm, this gave a cross section of 0.97x 0.33 cm (0.38"x0.13"). The mesh included an array of more realistically sized and shaped fiber tows. The fiber tows were an array of 16x16 fiber tows. The elliptical fiber tows were 10 cells in one dimension and 50 cells in the other. This geometry was studied at local Sherwood numbers that were calculated to correlate with temperatures of 700°C and 1400°C. The activation energy used in the calculations was 64.1 kJ/mol. Figure 52 shows the cross-sections for both temperatures at 25% of the carbon reacted. Computer difficulties

prevented the programs from running to a higher percentage of carbon consumed. However, in the cross-section correlating to 700°C a general minimal oxidation can be seen throughout the cross-section. For the cross-section correlating to 1400°C, a shrinking core and moving reaction front can be seen. These trends agree with those seen in Figures 19 and 20 for actual experimental cross-sections.

There were two observations in this analysis which helped lead to the geometry study to be discussed in the next section. First, a typical run of the model required 1.7 million array iterations, 136 billion program iterations, and 1 week to calculate on a PC to reach the point where 95% of the carbon had been reacted away. The calculations were quite intensive even though calculations for only one quarter of the mesh pattern were calculated and the other three quarters were mirrored from the first quarter. Therefore, a simplified geometry could possibly cut down on the number of calculations and the amount of time required for the analysis. Second, in the cross-sections for both the oxidized C/SiC coupon from experimentation and the oxidized fiber tow array from the model, it was seen that oxidation along the edge of the long dimension was uniform throughout the middle section of the sample. Oxidation along this middle section seemed to be primarily due to oxidation into and out (downward and upward directions) of the horizontal plane at both long edges and there appeared to be no contribution from left and right. Therefore a simplified geometry could possibly be found that matched the oxidation pattern along this uniformly oxidized region so that results from a simplified case could be used to approximate the oxidation of a much larger region.

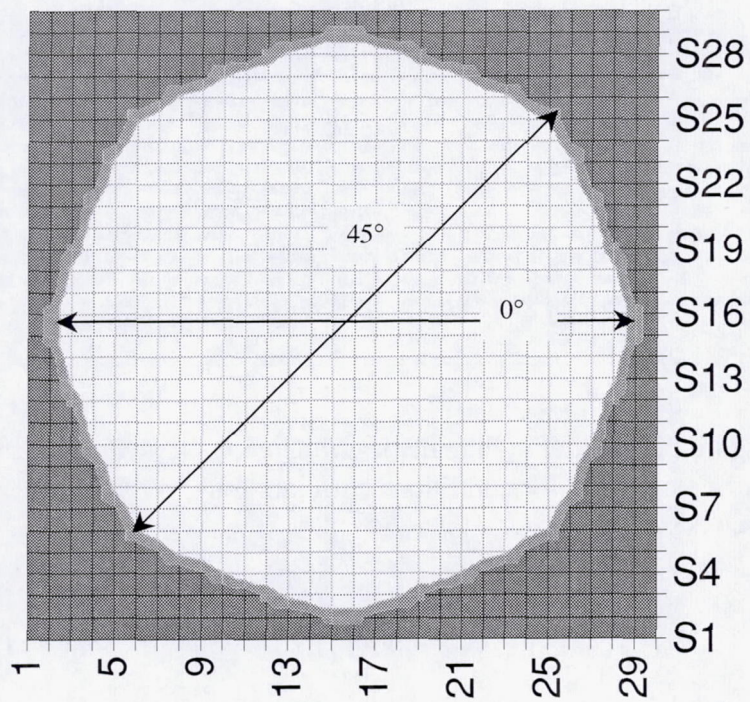
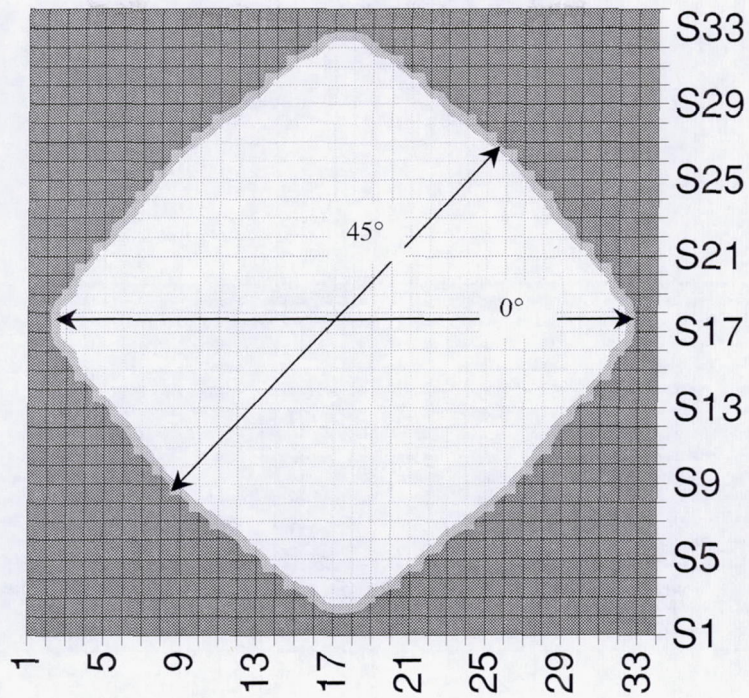


Figure 51 a-b. Close-up view of carbon core originally of 59 cells in radius at 95% reacted without a geometry correction (above) and with a geometry correction (below).

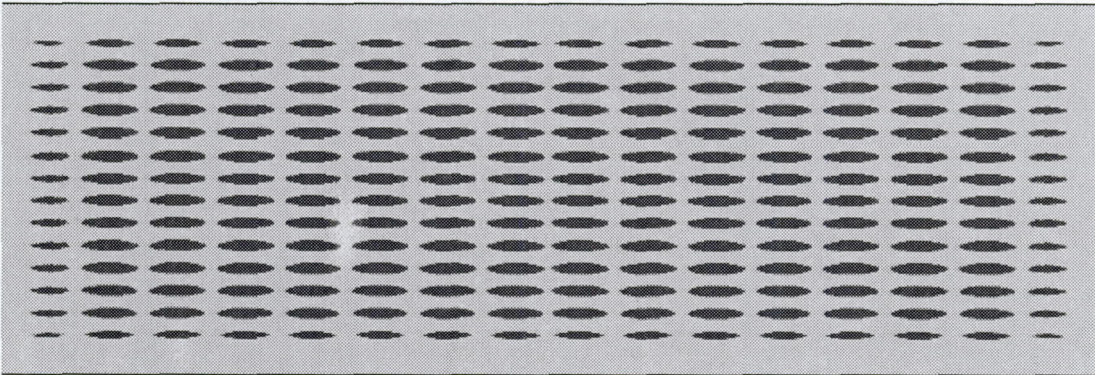
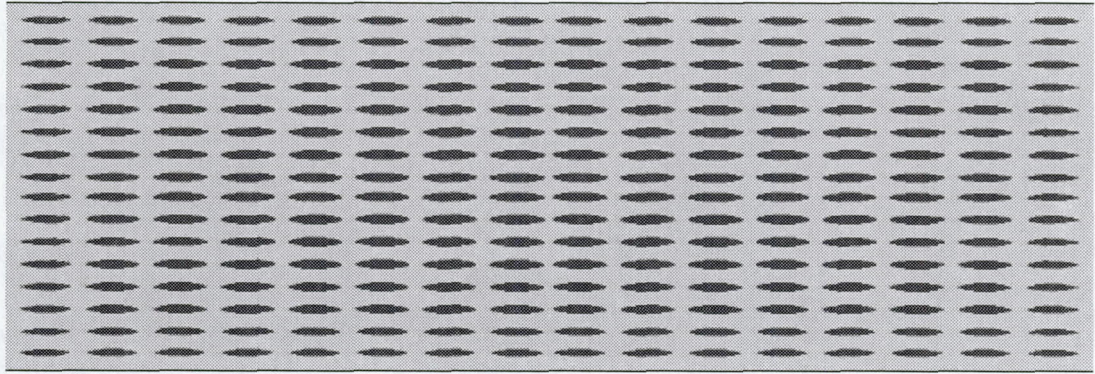


Figure 52. Modeling a realistic C/SiC geometry. Cross-sections at 25% of the carbon oxidized for conditions correlating to 700°C (above) and 1400°C (below).

### 3.3.3 Model Geometry Study and Comparison to Analytical Solutions

In the analysis for the diffusion of oxygen down a single column bounded by reactive carbon walls, the finite difference method (specifically the CW model) was compared to the analytical solutions for mass transport. The 1-D analytical solution agreed well with the finite difference CW model and the 2-D analytical solution at low local Sherwood numbers. However it was not accurate at high local Sherwood numbers where the high reactivity of carbon also causes gradients in oxygen concentration along the width of the column. At high local Sherwood numbers, the carbon is very reactive and the oxygen is therefore more quickly depleted. Because of the high carbon reactivity, there was not only a significant gradient in oxygen concentration along the length of the column, but also across its width. Since the 1-D solutions were the same for all positions along a given width (midpoint of column width to carbon wall), the predicted oxygen concentrations along the column are the same throughout the column for all lines from the midline to along the line directly adjacent to and parallel to the carbon wall.

The finite difference method was used to study the effect of geometry in the oxygen concentration obtained for the midline. For the FTA finite difference models, it was found that when the width was three times greater than the overall thickness (i.e. 12x36), the solution for the midline was much like that for the case of a column with no flux walls. The column with no flux walls represents the case for an infinitely wide fiber tow array (i.e. BW model which correlates to 12 x infinity). It is unclear why a width of three times the thickness had very little or no effect on the midline across the thickness for all local Sherwood numbers.

The relation between the large fiber tow array models and the much simpler column is very important in analysis. The large arrays can require thousands of iterative calculations that are quite time consuming especially when analysis includes actual carbon loss over hundreds of small time steps. When studying diffusion and oxidation kinetics in ceramic matrix composites of sufficient width and thickness, the BW model can allow for much simpler and quicker analysis of the oxidation kinetics.

Further analysis has found that even the case for the BW model can be simplified so that the finite difference model does not have to be used at all. Instead, an analytical solution may be used. The finite difference BW model was compared to the finite difference CW model and the 1-D analytical solution. The CW model and the 1-D analytical solution, which both considered the case for diffusion down a column bounded by continuous reactive walls, had a 10 cell insulation region included at the tip to match the pattern in the BW model which had the first fiber tow at ten cells into the column. Also since the BW model had fiber tows of 10 cells in diameter spaced 10 cells apart from one another, a correction had to be included to consider the difference in carbon volume for the different methods of analysis. It was found that a reaction rate constant of 0.75 K in the 1-D analytical solution and the CW Wall model gave good agreement with the BW model which had a reaction rate constant of 1.0 K. The oxygen concentrations across the middle of the column length is shown in Figure 53.

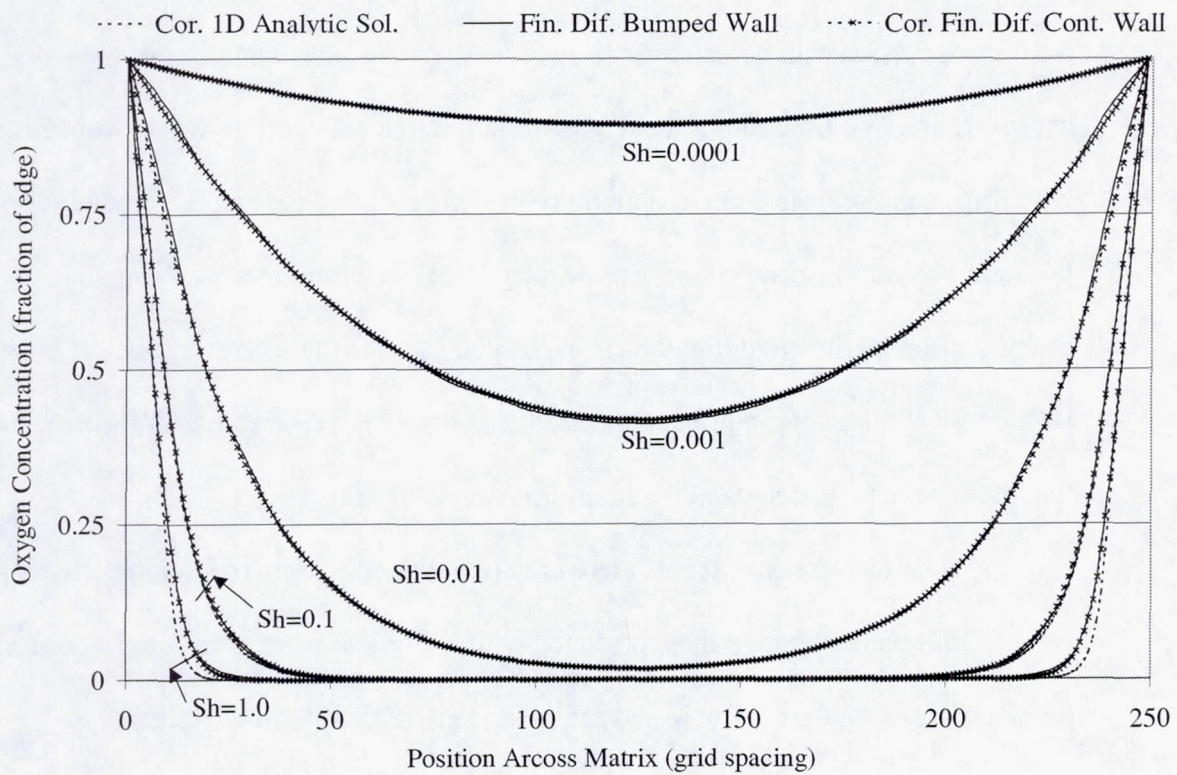


Figure 53. Correcting the Continuous wall models to fit the bumped wall model. Sherwood numbers are local Sherwood numbers.

### 3.4 Modeling Summary

An existing finite difference method was adapted to consider oxidation of crack bridging fiber tows in a crack bridging plane. The model was first investigated at steady-state. The oxygen concentration across the 2-D plane was determined for several different local Sherwood numbers. Plots of the oxygen concentration along the midline showed the effect of the local Sherwood number, which in turn could be used to determine the contributions from other variables, i.e., reaction rate constant, diffusion coefficient, temperature, and characteristic length. Also the effect of other variables such as the product and reactant gases, pressure, and activation energy could be determined from the diffusion coefficient and the reaction rate constant. The plots of the oxygen concentration as a function of local Sherwood number show regimes that would correlate with diffusion-controlled and reaction-controlled kinetics based on the gradients and levels of oxygen concentration. At low local Sherwood numbers, gradients in oxygen concentration are low and high levels of oxygen saturate the interior of the 2-D surface. At high local Sherwood numbers, the gradients in oxygen concentration from the edge to the interior are very steep and the interior is deprived of oxygen.

When the model also considered the removal of carbon, oxidation patterns for the two regimes were obtained that correlated with the oxidation patterns observed from the microstructural analysis of polished cross-sections of samples that were stressed oxidation tested. For a high local Sherwood number in the diffusion-controlled regime, the model predicted a shrinking core type of effect where the outer perimeter of fiber tows would be completely consumed before oxidation would progress further inward. Fiber tows in the center of the 2-D plane remained unreacted until the reaction front had

reached them. For a low local Sherwood number in the reaction-controlled regime, the model predicted a generalized oxidation throughout the 2-D plane. Fiber tows at the outer perimeter showed signs of oxidation as well as for the fiber tows in the very center. Even when 95% of the carbon had been reacted, remnants of carbon tows remained throughout most of the 2-D plane.

The geometry analysis showed that for wide enough cross-sections (i.e., a width three times greater than the thickness) the bumped wall finite difference model could be used to predict the oxygen concentration across the thickness in the center of the section. The oxygen concentration along this midline would give a good approximation for much of the overall cross-section (approximately the central two-thirds across of the width of the rectangular cross-section). It was shown that the single column models (1-D analytical solution and the continuous wall finite difference model) could be corrected to fit the bumped wall model. This would allow a slightly simpler finite difference model or a much simpler analytical solution to be used in the analysis of a cross-section's oxidation and kinetics.

#### 4. CONCLUSIONS

1. As seen from environmental studies, microstructural analysis, and theoretical modeling, the oxidation of carbon occurs in two primary regimes, i.e, the diffusion-controlled regime and the reaction-controlled regime. The temperature range for the reaction-controlled regime was 500°C-800°C. The temperature range for the diffusion-controlled regime was 800°C-1500°C.
2. In the reaction-controlled regime, there was a strong temperature dependence. In this regime, component lives were longer and strains to failure were lower when the material was under tension and weight loss rates were lower. Calculations indicate that the interior was saturated in oxygen and relatively slow oxygen/carbon reactions occurred throughout.
3. In the diffusion-controlled regime, there was a less of a temperature dependence. In this regime, component lives were shorter and strains to failure were higher when the material was under tension and weight loss rates were higher. Calculations indicate that there was a sharp gradient in oxygen concentration up to the moving reaction front and a shrinking core of the carbon fiber tow arrays was seen.

4. Thermogravimetric analysis of carbon fiber in flowing oxygen gave an activation energy of 64.1 kJ/mol in the temperature range of 500°C-600°C and an apparent activation energy of 7.6 kJ/mol for temperatures from 600°C-1400°C.
  
5. The carbon fiber within a matrix oxidized very differently depending on if the composite was under stress or not. Without stress, the material became self-protected at temperatures from 900°C-1400°C due to matrix effects, i.e., the formation of silica and the closing of matrix cracks. However, when the composite was under stresses of 10 and 25 ksi, the carbon was susceptible to oxidation across the whole temperature range (550°C-1500°C). At temperatures from 750°C-1500°C, an increase in stress from 10 to 25 ksi caused a 67-82% reduction in times to failure.
  
6. The addition of boron containing oxidation inhibitors were effective in significantly prolonging life and retaining strength even when the composite was under stresses as high as 10 and 25 ksi at a temperature of 1454°C.
  
7. The finite difference model is an effective method for studying the oxidation trends and oxidation kinetics of carbon fibers in cracked composites. The local oxygen concentrations, gradients in oxygen concentration, and the local Sherwood number directly relate to the kinetics. The use of the local Sherwood number as a variable also allows the influence of several other variables to be determined, i.e., the diffusion coefficient, the reaction rate constant and temperature.

8. Simplified finite difference models, and 1-D and 2-D analytical solutions can be used to predict the oxygen concentration and kinetics for much of a cross-section. In most cases, depending on the accuracy required, the 1-D model can be sufficient for most types of analysis. For thorough investigations, a complete finite difference model for the whole crack bridging plane (or mirrored one-quarter or one-eighth sections, depending on the geometry) will be required for corner and end effects (ends of the long dimension) to be determined.

## 5. APPENDIX - STUDYING THE EFFECT OF FLAWS

The effects of flaws were analyzed using the finite difference model. The analysis was conducted in order to determine their effect on the oxidation pattern of a crack bridging cross-section consisting of a 24x24 array of crack bridging fiber tows. The oxidation of the fiber tow array in the 2-D plane was studied for conditions for the diffusion controlled regime and for the reaction controlled regime. Flaws were randomly introduced into 25% of the carbon containing cells. These cells were assigned a reaction rate constant that varied randomly from 7.5 to 10 times the reaction rate constant for the rest of the carbon containing cells. As in the previous analyses using the finite difference model, the fiber tows are ten cells in diameter.

Oxidation patterns at 25%, 75%, and 95% of the carbon reacted are shown for both kinetic regimes for one-quarter of the overall cross-section. Examples of the oxidation patterns for the diffusion controlled regime are shown in Figures A1-A3 for 25%, 75%, and 95% carbon reacted. In all of the figures, A1-A6, the center of the cross-section is located at the lower, right-hand corner. It is seen that in this regime which is very dependent on the supply of oxygen, the presence of flaws had little effect. Oxidation occurred primarily along the outer perimeters of carbon. Once the outer perimeter was consumed, the reaction front continued to move inward.

Examples of the oxidation patterns for the reaction controlled regime are shown in Figures A4-A6 for 25%, 75%, and 95% carbon reacted. Again, it was seen that the presence of flaws had little effect. A generalized minimal oxidation of most of the fiber tows was observed as oxidation progressed. Pockets of consumed carbon fiber tows in the interior surrounded by less reacted regions were not observed.

In conclusion, for the flaws and flaw distribution investigated, the presence of flaws had little effect in the oxidation patterns. In the reaction controlled regime, the flaws only had a localized effect. In the diffusion controlled regime, the effect was also localized but the supply of oxygen was the primary factor in determining the overall oxidation pattern.

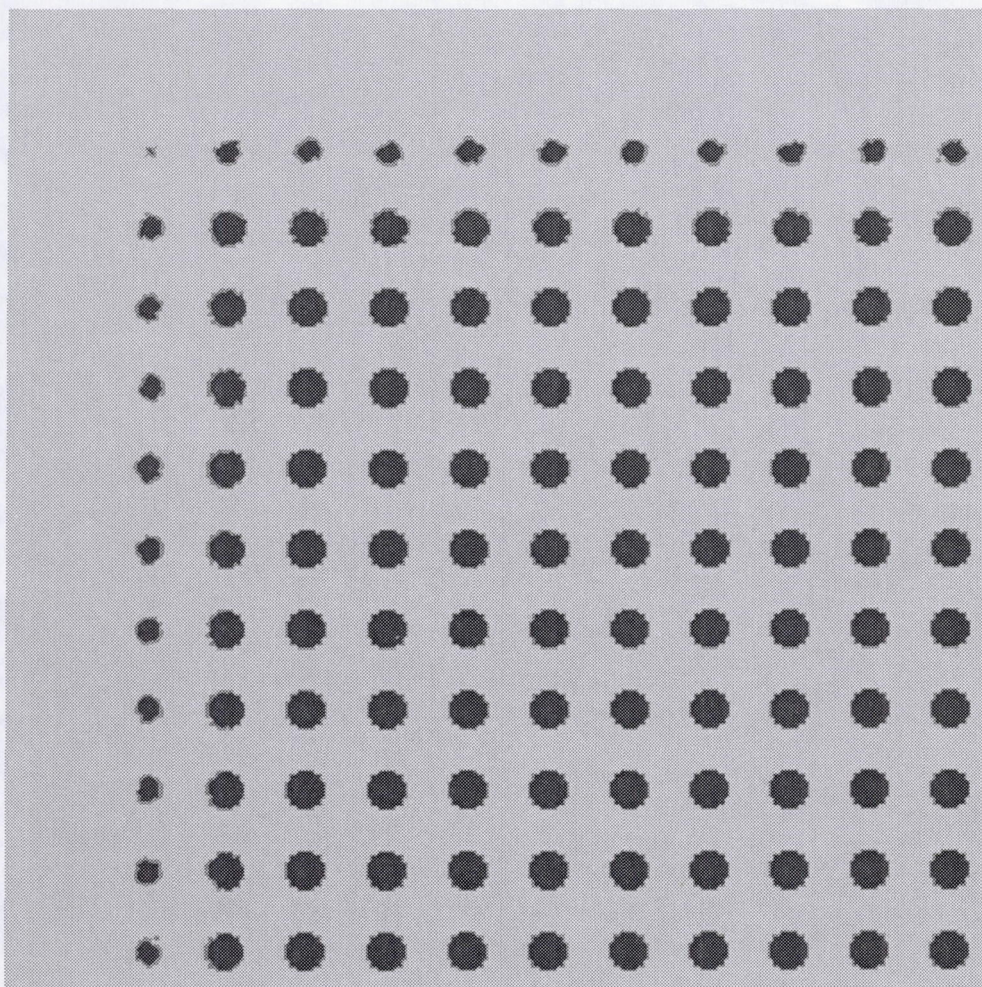


Figure A1. Example of a 25% carbon reacted cross-section for the diffusion controlled regime. One-quarter plot of a 24x24 fiber tow array.

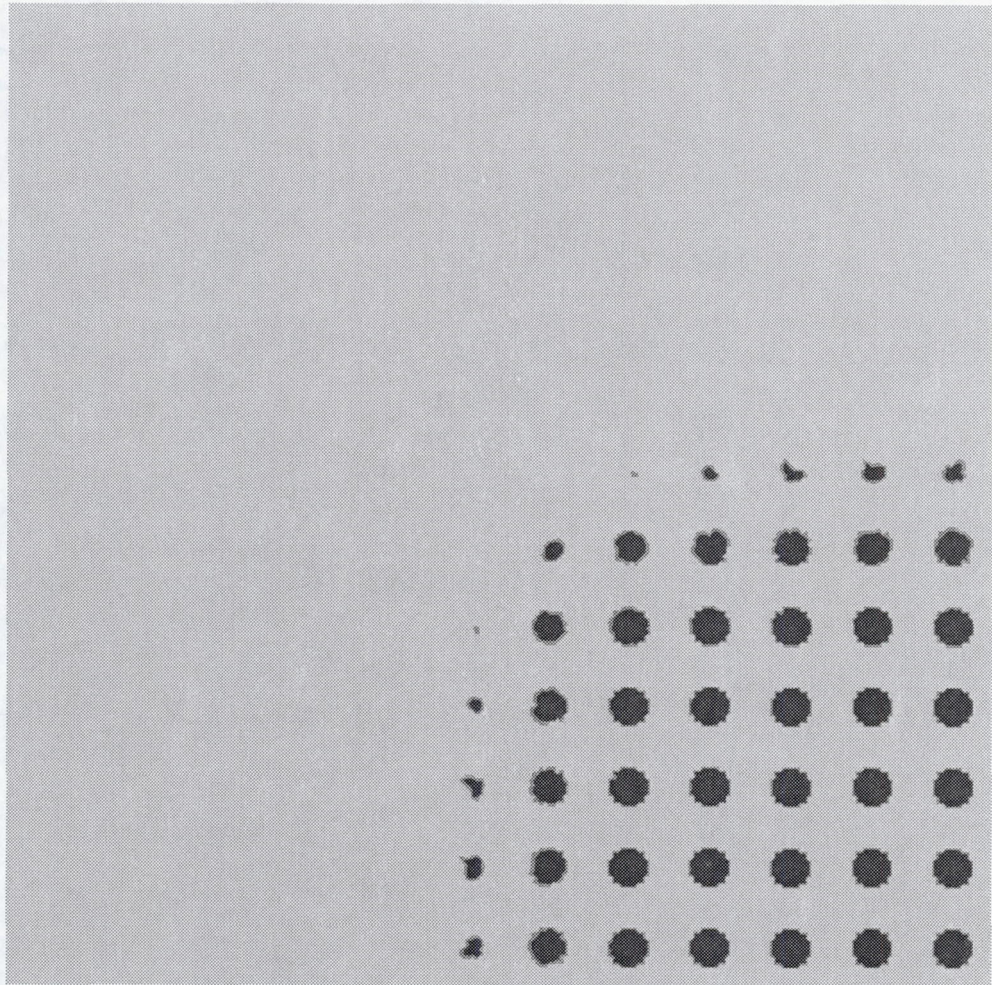


Figure A2. Example of a 75% carbon reacted cross-section for the diffusion controlled regime. One-quarter plot of a 24x24 fiber tow array.

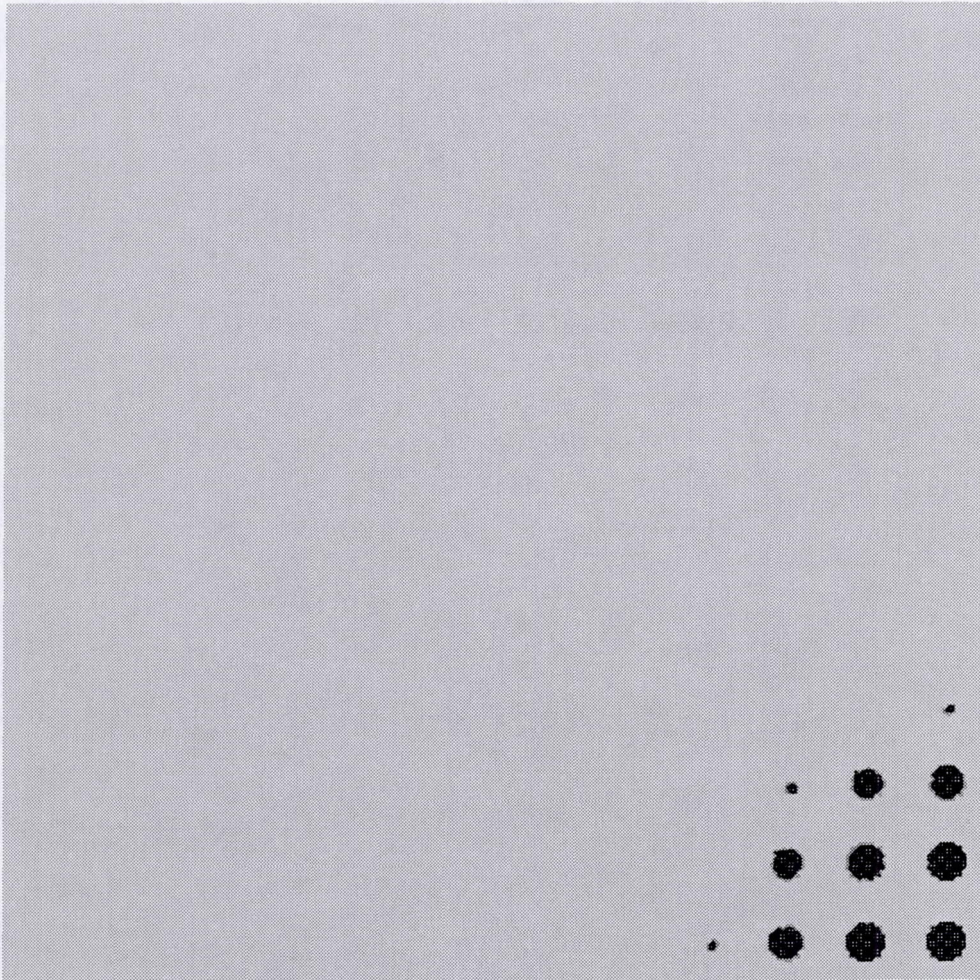


Figure A3. Example of a 95% carbon reacted cross-section for the diffusion controlled regime. One-quarter plot of a 24x24 fiber tow array.

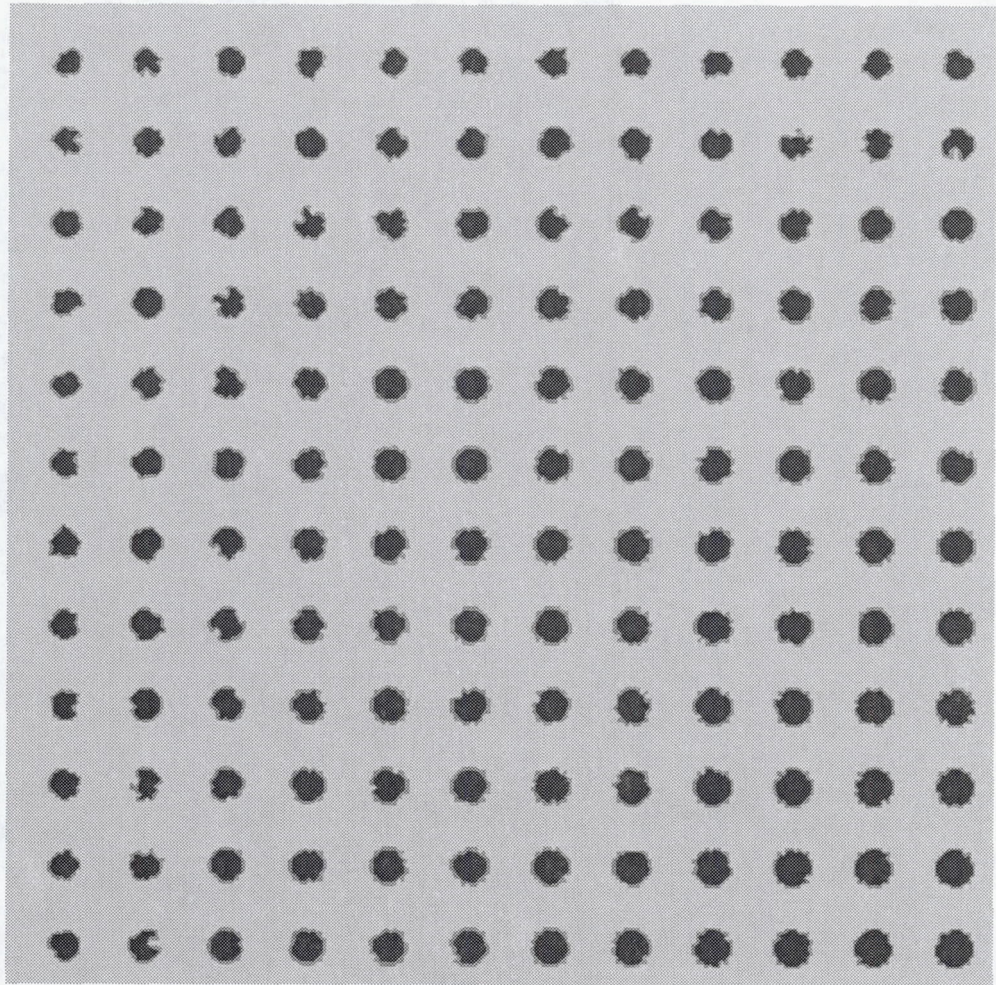


Figure A4. Example of a 25% carbon reacted cross-section for the reaction controlled regime. One-quarter plot of a 24x24 fiber tow array.

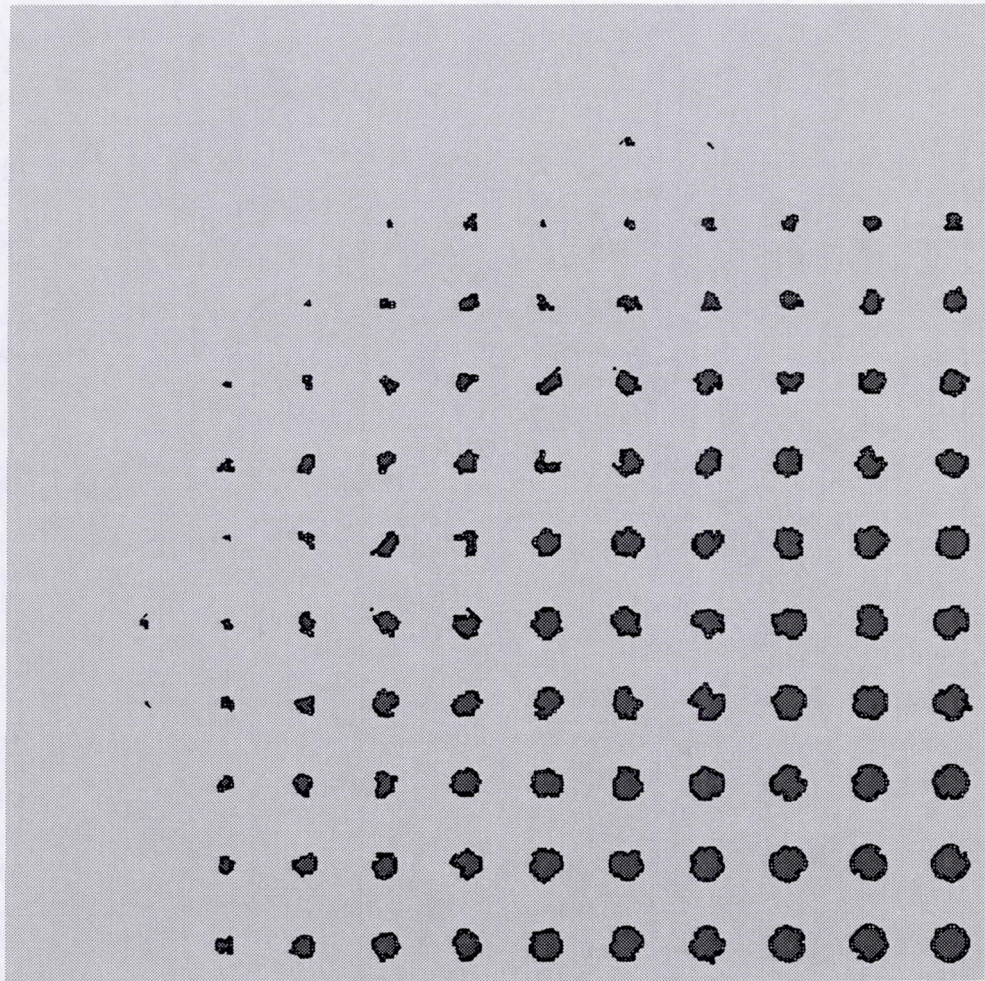


Figure A5. Example of a 75% carbon reacted cross-section for the reaction controlled regime. One-quarter plot of a 24x24 fiber tow array.

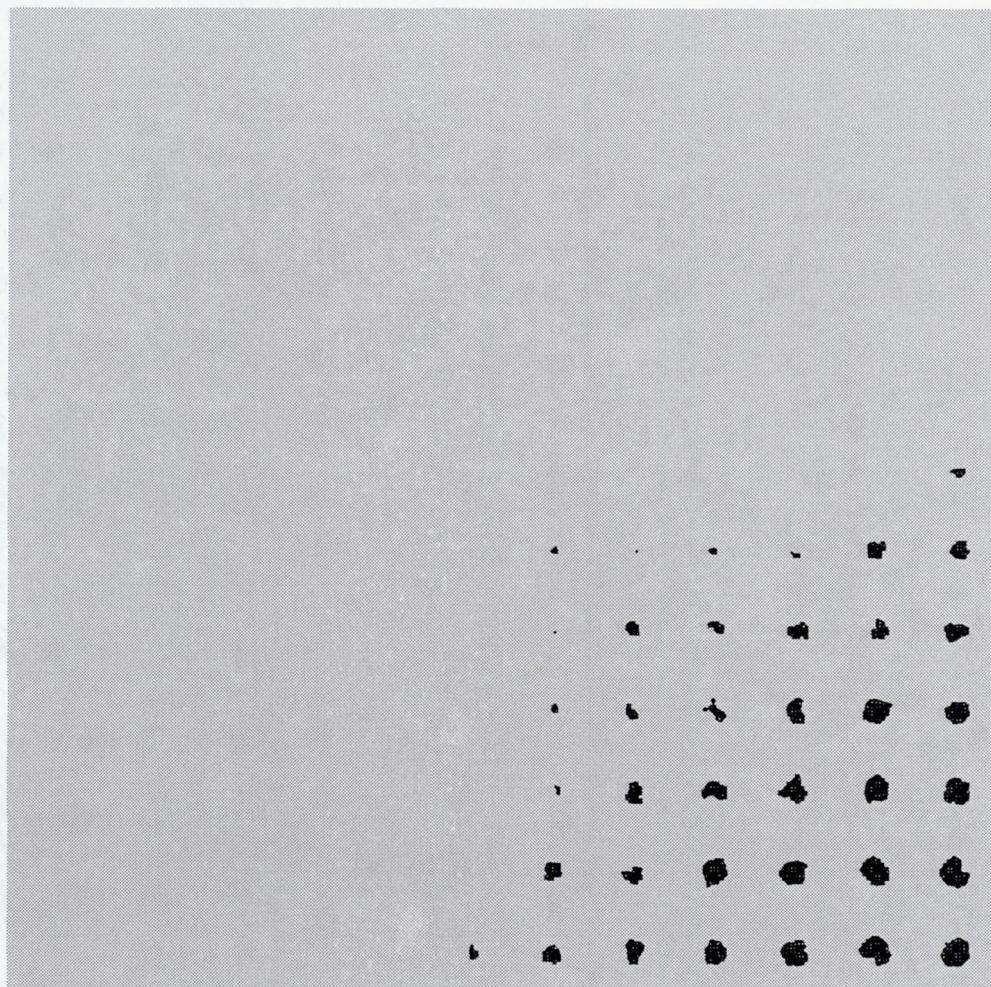


Figure A6. Example of a 95% carbon reacted cross-section for the reaction controlled regime. One-quarter plot of a 24x24 fiber tow array.

## 6. BIBLIOGRAPHY

Bird, R. B.; Stewart, W. E.; Lightfoot, E. N. *Transport Phenomena*, John Wiley & Sons, Inc., New York, 1963.

Camus, G.; Barbier, J. E. "Tensile Behavior of a 2D Woven C/SiC Composite at Ambient and Elevated Temperatures," Edited by A. G. Evans and R. Naslain, *High Temperature Ceramic Matrix Composites I*, Vol. Ceramic Transactions, 57. Westerville, OH: The American Ceramics Society, (1995) 407-412.

Carslaw, H. S.; Jaeger, J. C. *Conduction of Heat in Solids*, Oxford at the Clarendon Press, New York, 1950.

Crocker, P.; McEnaney, B. "Oxidation and Fracture of a Woven 2D Carbon-Carbon Composite," *Carbon*, **29** [8] (1991) 881-885.

Effinger, M. R.; Koenig, J. R.; Halbig, M. C. "C/SiC Mechanical and Thermal Design Data for a Turbopump Blisk," published in the proceedings of the 21<sup>st</sup> annual Conference on Composites, Materials, and Structures, Cocoa Beach, Florida, January 26-31, 1997.

Eckel, A. J.; Cawley, J. D.; Parthasarathy, T. A. "Oxidation Kinetics of a Continuous Carbon Phase in a Nonreactive Matrix," *J. Amer. Ceram. Soc.*, **78**, [4] (1995) 972-980.

Eckel, A. J. "Rate Laws for Material Recession Resulting From Gas-Solid Interactions in Multiphase Ceramics," Ph. D. Dissertation, Case Western Reserve University, May, 1998.

Eckel, A. J. Private Conversation, NASA Glenn Research Center, November, 1999.

Filipuzzi, L.; Camus, G.; Naslain, R. "Oxidation Mechanisms and Kinetics of 1D-SiC/C/SiC Composite Materials: 1, An Experimental Approach," *J. Am. Ceram. Soc.*, **77** [2] (1994) 459-466.

Gaskell, D. R. *An Introduction to Transport Phenomena in Materials Engineering*, Macmillan Publishing Company, New York, 1992.

Geankoplis, W. *Mass Transport Phenomena*, Ohio State U. Bookstore, Columbus, OH, 1978.

Glime, W. H.; Cawley, J. D. "Oxidation of Carbon Fibers and Films in Ceramic Matrix Composites: A Weak Link Process," *Carbon*, **33** [8] (1995) 1053-1060.

Goujard, S.; Vandenbuckle, L.; Tawil, H. "The Oxidation Behavior of Two- and Three-Dimensional C/SiC Thermostructural Materials Protected by Chemical Vapor Deposition Polylayers Coatings," *Journal of Materials Science*, **29** (1994) 6212-6220.

Herbell, T. P.; and Eckel, A. J. "Ceramic Matrix for Rocket Engine Turbine Applications," *Transactions of the ASME*, **115** (1993) 64-69.

Herbell, T. P.; Eckel, A. J. "Ceramic Composites Portend Long Turbopump Lives," published in the proceedings of the 1993 SAE Aerospace Atlantic Conference and Exposition, Dayton, Ohio, April 20-23, 1993.

Holmes, J. W.; Morris, J. "Elevated Temperature Creep of a 3-D Composite," published in the proceedings of the 15<sup>th</sup> Annual Conference on Ceramics and Advanced Composites, Cocoa Beach, FL, January, 1991, Paper 89-C-91F.

Incropera, F. P; DeWitt, D. P. *Fundamentals of Heat and Mass Transfer*, John Wiley & Sons, New York, 1985.

Ismail, I. M. K. "On the Reactivity, Structure, and Porosity of Carbon Fibers and Fabrics," *Carbon*, **29** [6] (1991) 777-792.

Lamouroux, F.; Camus, G.; Thebault, J. "Kinetics and Mechanisms of Oxidation of 2D Woven C/SiC Composites: I, Experimental Approach," *J. Am. Ceram. Soc.*, **77** [8] (1994) 2049-57.

Lamouroux, F.; Bourrat, X.; Naslain, R.; Sevely, J. "Structure/Oxidation Behavior Relationship in the Carbonaceous Constituents of 2-D/PyC/SiC Composites," *Carbon*, **31** [8] (1993) 1273-1288.

Lowden, R. A. ORNL/TM-11039, March 1989. Available from NTIS, U.S. Dept. of Commerce, Springfield, VA, (1989) 26-32.

McKee, D. W. "Oxidation Behavior of Matrix-Inhibited Carbon/Carbon Composites," *Carbon*, **26** [5] (1998) 659-665.

Mensessier, E.; Dumont, J. P.; Guette, A.; Pailler, R.; Raberdel, L.; Naslain, R. *Ceram. Eng. Sci. Proc.*, **10** (1989) 1496.

Ogbuji, L. U. J. T.; Opila, E. J. "A Comparison of the Oxidation Kinetics of SiC and Si<sub>3</sub>N<sub>4</sub>," *Journal of the electrochemical Society*, **142** [3] (1995) 925-930.

Pickup, I. M.; McEnaney B.; Cooke, R. G. "Fracture Processes and the Effects of Oxidation," *Carbon*, **24** [5] (1986) 535-543.

Rodrigues, P. A.; Rosa, L. G.; Sten, M. "Fatigue Behavior of a Ceramic Matrix Composite (CMC), 2D C fiber/SiC matrix," Edited by A. G. Evans and R. Naslain, *High Temperature Ceramic Matrix Composites I*, Vol. Ceramic Transactions, 57. Westerville, OH: The American Ceramics Society, (1995) 401-406.

Shemet, V. Zh.; Pomytkin, A. P.; Neshpor, V. S. "High Temperature Oxidation Behavior of Carbon Materials in Air," *Carbon*, **31** [1] (1993) 1-6.

Sines, G.; Yang, Z.; Vickers, B. D. "Creep of Carbon Yarn and a Carbon Composite at High Temperatures and High Stresses," *Carbon*, **27** [3] (1989) 403-415.

Villeneuve, J. F.; Naslain, R.; Fourmeaux, R.; Sevely, J. *Composite Sci. Technology*, **48**, [89], 1993.

Vix-Guterl, C.; Lahaye J.; Ehrburger, P. "Reactivity of Silicon Carbide and Carbon with Oxygen in Thermostructural Composites," *Carbon*, **31** [4] (1993) 629-635.

Windisch C. F. Jr.; Henager C. H. Jr; Springer, G. D.; Jones, R. H. "Oxidation of the Carbon Interface in Nicalon-Fiber-Reinforced Silicon Carbide Composite," *J. Amer. Ceram. Soc.*, **80**, [3] (1997) 569-574.

Wilshire B.; Jiang, H. "Deformation and Failure Processes During Tensile Creep of Sintered Silicon Carbide," *British Ceramic Transactions*, **93** [6] (1994) 213-218.

Wood, J. L.; Bradt, R. C.; Walker, P. L. Jr. "Oxidation Effects on Toughness and Slow Crack Growth in Polycrystalline Graphites," *Carbon*, **18** (1980) 179-189.

Yasuda, E.; Tanabe, T.; Machino, H.; Takaku, A. *Extended Abstract of the 18<sup>th</sup> Biennan Conf. Carbon*, (Edited by Amer. Carbon Soc.), University Park, PA, (1990) 30-31.

# REPORT DOCUMENTATION PAGE

Form Approved  
OMB No. 0704-0188

Public reporting burden for this collection of information is estimated to average 1 hour per response, including the time for reviewing instructions, searching existing data sources, gathering and maintaining the data needed, and completing and reviewing the collection of information. Send comments regarding this burden estimate or any other aspect of this collection of information, including suggestions for reducing this burden, to Washington Headquarters Services, Directorate for Information Operations and Reports, 1215 Jefferson Davis Highway, Suite 1204, Arlington, VA 22202-4302, and to the Office of Management and Budget, Paperwork Reduction Project (0704-0188), Washington, DC 20503.

<b>1. AGENCY USE ONLY (Leave blank)</b>	<b>2. REPORT DATE</b> <p style="text-align: center;">June 2001</p>	<b>3. REPORT TYPE AND DATES COVERED</b> <p style="text-align: center;">Technical Memorandum</p>	
<b>4. TITLE AND SUBTITLE</b> <p style="text-align: center;">The Oxidation Kinetics of Continuous Carbon Fibers in a Cracked Ceramic Matrix Composite</p>		<b>5. FUNDING NUMBERS</b> <p style="text-align: center;">WU-242-82-77-00 1L161102AH45</p>	
<b>6. AUTHOR(S)</b> <p style="text-align: center;">Michael C. Halbig</p>		<b>8. PERFORMING ORGANIZATION REPORT NUMBER</b> <p style="text-align: center;">E-12487</p>	
<b>7. PERFORMING ORGANIZATION NAME(S) AND ADDRESS(ES)</b> National Aeronautics and Space Administration John H. Glenn Research Center Cleveland, Ohio 44135-3191 and U.S. Army Research Laboratory Cleveland, Ohio 44135-3191		<b>10. SPONSORING/MONITORING AGENCY REPORT NUMBER</b> <p style="text-align: center;">NASA TM-2000-210520 ARL-TR-2296</p>	
<b>9. SPONSORING/MONITORING AGENCY NAME(S) AND ADDRESS(ES)</b> National Aeronautics and Space Administration Washington, DC 20546-0001 and U.S. Army Research Laboratory Adelphi, Maryland 20783-1145		<b>11. SUPPLEMENTARY NOTES</b> <p>This report was submitted as a dissertation in partial fulfillment of the requirements for the degree of Master of Science to the Case Western Reserve University, Cleveland, Ohio, May 2000. Responsible person, Michael C. Halbig, organization code 5130, 216-433-2651.</p>	
<b>12a. DISTRIBUTION/AVAILABILITY STATEMENT</b> Unclassified - Unlimited Subject Category: 24 Available electronically at <a href="http://gltrs.grc.nasa.gov/GLTRS">http://gltrs.grc.nasa.gov/GLTRS</a> This publication is available from the NASA Center for AeroSpace Information, 301-621-0390.		<b>12b. DISTRIBUTION CODE</b> <p style="text-align: center;">Distribution: Nonstandard</p>	
<b>13. ABSTRACT (Maximum 200 words)</b> <p>Experimental observations and results suggest two primary regimes as a function of temperature, i.e., diffusion and reaction controlled kinetics. Thermogravimetric analysis of carbon fiber in flowing oxygen gave an activation energy of 64.1 kJ/mol in the temperature range of 500 to 600 °C and an apparent activation energy of 7.6 kJ/mol for temperatures from 600 to 1400 °C. When C/SiC composite material was unstressed, matrix effects at temperatures from 900 to 1400 °C protected the internal fibers. When under stress, self-protection was not observed. Increasing the stress from 10 to 25 ksi caused a 67 to 82 percent reduction in times to failure at temperatures from 750 to 1500 °C. Based on experimental results, observation, and theory, a finite difference model was developed, which simulates the diffusion of oxygen into a matrix crack that is bridged by carbon fibers. The model allows the influence of important variables on oxidation kinetics to be studied systematically, i.e., temperature, reaction rate constant, diffusion coefficient, environment, and sample geometry.</p>			
<b>14. SUBJECT TERMS</b> <p style="text-align: center;">Ceramic matrix composite; Oxidation kinetics; Carbon fiber</p>			<b>15. NUMBER OF PAGES</b> <p style="text-align: center;">147</p>
<b>17. SECURITY CLASSIFICATION OF REPORT</b> <p style="text-align: center;">Unclassified</p>			<b>16. PRICE CODE</b>
<b>18. SECURITY CLASSIFICATION OF THIS PAGE</b> <p style="text-align: center;">Unclassified</p>	<b>19. SECURITY CLASSIFICATION OF ABSTRACT</b> <p style="text-align: center;">Unclassified</p>	<b>20. LIMITATION OF ABSTRACT</b>	